UNIVERSITY OF GENOVA

POLYTECHNIC SCHOOL

DIME

Department of Mechanical, Energy, Management and Transportation Engineering

MASTERS THESIS

IN

ENERGY ENGINEERING

Hydrogen-driven system for smart buildings: modelling and energy management

Supervisors:

Chiar.mo Prof. Ing. Mario Luigi Ferrari

Prof. Mohsen Assadi

Co-supervisor:

Reyhaneh Banihabib

Candidates:

Sobhan Mashatzadegan

Hamidreza Golesorkhi

March 2024

UNIVERSITÀ DEGLI STUDI DI GENOVA

SCUOLA POLITECNICA

DIME

Dipartimento di Ingegneria Meccanica, Energetica, Gestionale e dei Trasporti

TESI DI LAUREA MAGISTRALE

IN

INGEGNERIA ENERGETICA

Sistema ad idrogeno per edifici intelligenti: modellazione e gestione dell'energia

Relatori:

Chiar.mo Prof. Ing. Mario Luigi Ferrari

Prof. Mohsen Assadi

Correlatore:

Reyhaneh Banihabib

Allievi:

Sobhan Mashatzadegan

Hamidreza Golesorkhi

Marzo 2024

Hydrogen-driven system for smart buildings: modelling and energy management

Abstract

This research delves into the integration of hydrogen-driven energy systems within smart buildings, focusing on the development of a physics-based model that combines electrolyzer, fuel cell, and hydrogen storage. The core strategy leverages off-peak hours to store energy, optimizing its use during periods of high demand through a daily operation algorithm. Utilizing MATLAB Simscape, the study presents a case involving the My-Box building at the University of Stavanger, demonstrating how hydrogen technology can be effectively employed to enhance sustainability and efficiency. The research underscores the capability of the system to leverage hydrogen for energy storage and electricity generation, particularly emphasizing the model feasibility in reducing operational costs and carbon emissions. Additionally, the thesis highlights the benefits of dynamic energy management in response to electricity price fluctuations in a daily timeframe, showcasing the viability of the strategy in regions with significant daily electricity price variations. This approach offers a promising pathway for smart buildings aiming to achieve greener energy solutions and economic efficiency against the backdrop of fluctuating energy market conditions.

Acknowledgements

We extend our sincere gratitude to our esteemed supervisors, Professor Mohsen Assadi from the University of Stavanger, Professor Mario Luigi Ferrari, and all other Professors at the University of Genova/DIME, for their exceptional guidance, unwavering support, and invaluable insights throughout the course of this thesis. Their expertise, encouragement, and dedication have been pivotal in shaping our research and guiding us through the complexities of our academic endeavor.

We are also deeply thankful to our co-supervisor at the University of Stavanger, Reyhaneh Banihabib, whose invaluable contributions, insightful feedback, and continuous encouragement have greatly enriched the depth and quality of our work. Her expertise and guidance have been indispensable in navigating the challenges of our research journey.

Furthermore, we express our heartfelt appreciation to our families for their unconditional love, unwavering support, and understanding during this endeavor. Their encouragement and belief in our capabilities have served as a constant source of motivation and strength.

Additionally, we extend our gratitude to our friends and colleagues for their encouragement, assistance, and camaraderie throughout this journey. Your support and camaraderie have been deeply appreciated and have made this academic pursuit more rewarding.

To all those mentioned above, as well as to anyone whose support has contributed to this thesis in ways seen and unseen, we offer our heartfelt thanks. Your contributions have been invaluable, and we are profoundly grateful for your guidance, support, and encouragement.

With sincere appreciation

یک چند به کودکی به استاد شدیم

یک چند به استادی خود شاد شدیم

پایان سخن شنو که ما را چه رسید

از خاک در آمدیم و بر باد شدیم

حکیم عمر خیام

Table of Contents

List of figures & tables

1. Introduction

1.1 Smart buildings in the evolving environment

To mitigate the most detrimental effects of climate change, it is essential to reduce carbon dioxide emissions. In 2021, the Intergovernmental Panel on Climate Change (IPCC) released important data regarding climate objectives. They reported that to keep global warming below 1.5°C, the world needs to limit its carbon dioxide emissions to no more than 400 billion tonnes. At the current rate of emissions, an average nation is expected to use up its portion of this limit within the next eight years (IPCC, 2021). The primary cause of the increase in atmospheric CO_2 levels is the combustion of fossil fuels, which also brings geopolitical hazards, as seen by the recent energy crisis stemming from the conflict in Ukraine. Consequently, the cessation of fossil fuel utilization has become a key goal in global energy and climate policies. The European Climate Law mandates that EU nations collectively achieve net-zero greenhouse emissions by the year 2050 (European Union, 2021) [1]. On January 8, 2021, Norway endorsed a detailed climate initiative to align with the Paris Agreement and foster sustainable economic development. The Norwegian government has outlined a strategy to cut emissions across all industries, with the objective of achieving carbon neutrality by 2030. Starting from January 1, 2030, Norway will counterbalance its greenhouse gas emissions by supporting emission reductions abroad, utilizing mechanisms like the EU Emission Trading Scheme, global emission reduction collaborations, carbon trading, and project-based partnerships [2].

The shift to a decarbonized society entails the transition to clean energy sources and the adoption of low-carbon alternatives across various sectors. Scenarios derived from numerous studies point to a future energy system that is economically and technically optimized by primarily harnessing renewable energy [3]. Given the intermittent nature of primary renewable sources like wind and solar power, ensuring a constant equilibrium between energy supply and consumption poses a significant challenge. The fluctuating nature of energy supply and demand naturally leads to variable energy pricing, which encourages consumers to invest in systems that maximize energy utilization during cost-effective periods.

The International Energy Agency (IEA) reports that in 2021, heating was responsible for roughly half of the world's energy consumption, as depicted in Figure 1(a). Of this, space heating and domestic hot water (DHW) combined account for approximately 46% of total heat consumption, translating to about a quarter of the global energy consumption dedicated to space heating and DHW. The proportion of energy used for heating is notably higher in colder climates, such as in Norway, as indicated in Figure 1.1 [4]. From research focusing on Norway's energy use for heating and cooling in 2020, it was determined that the total consumption amounted to about 72.5 TWh. This figure represents 33% of the nation's overall energy consumption, which stands at 216 TWh. The breakdown of heating energy within Norway shows that the residential sector accounts for 37.5 TWh (52%), the industrial sector for 37.5 TWh (26%), and the combined service and agricultural sectors for 16 TWh (22%) of the total heating energy usage. Given that household energy consumption totals 48 TWh,

with 37.5 TWh used for heating and cooling, it can be concluded that nearly 78% of a Norwegian household's energy usage is for heating, cooling, and DHW [4,5].

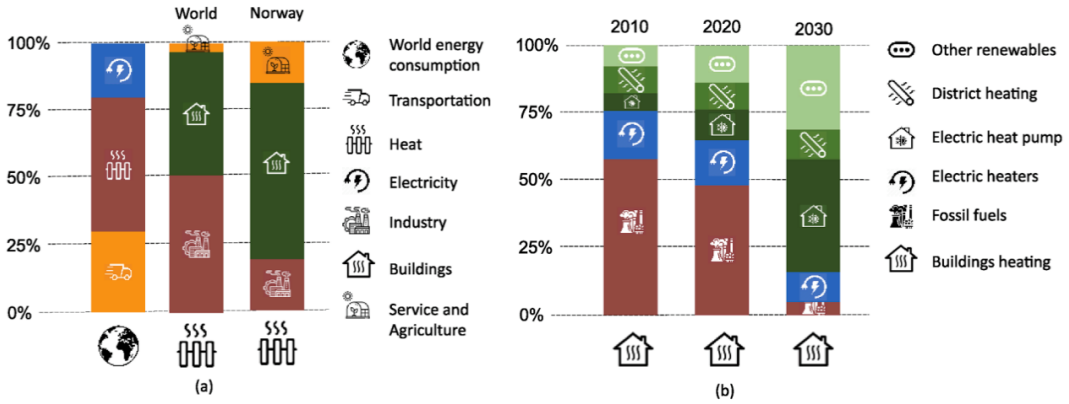

Figure 1.1 (a) World heat consumption and share of buildings from it in the world and Norway, (b) Heating sources for buildings in net zero scenarios, 2020–2030, [5]

Actions directing to enhance the structural energy efficiency of buildings, such as improving thermal insulation, are usually executed in connection with comprehensive renovations, which is a decades-long cycle. However, the energy efficiency of buildings can also be enhanced through the implementation of advanced control algorithms in building technical systems, managing energy use. Such technology can be integrated not only during construction, but also throughout the lifecycle of a building. Advancements in building intelligence have the potential to significantly diminish their ecological footprint.

What, then, is a smart building? A smart building is designed to balance the requirements of the occupants' comfort and energy consumption. It involves the installation and use of advanced and integrated building technology systems, including building management systems (BMSs), life safety, information and communications technology (ICT), user systems, and facility management systems. The sophistication of BMS elements such as control of heating, ventilation, and air conditioning (HVAC), lighting, power, and metering is crucial for a building operational energy efficiency. Smart buildings embody and adapt to the rapid evolution and integration of various building systems. They can adapt energy use to varying occupancy levels, reduce excess lighting, adaptively respond to environmental changes like sunlight or temperature with active shading, adjust operations based on external conditions such as occupant schedules, weather forecasts, or electricity tariffs, and offer feedback and advice to users. Smart buildings are also key components within the smart grid framework, where the collective energy management of buildings can become a dynamic resource that might engage with energy or balance markets under specific scenarios. The smart building concept transcends a single product or service and requires interoperable technical systems, which are often designed, supplied, installed, and commissioned by different entities. By integrating these systems, the smart building concept seeks to have the building technology operate as a unified, intelligent system, thus streamlining the efficiency from the design phase through to daily operation [1].

1.2 The essential role of storage

What could be the contribution of smart buildings to the green energy transition? The major building blocks of a renewable energy system are the sources of energy, particularly solar and wind, together with the equipment converting electricity to heat, fuels, and chemicals, electrified transportation, and energy storages [6]. In this context, buildings are often referred to as prosumers, implying that they do not only consume but also generate energy. The construction sector is recognized as a critical component of the green transition, with an estimated one-fourth of the global investment required for a renewable energy infrastructure directed towards energy generation within buildings [7]. As the electric grid shifts from a linear, fossil fuel-dependent framework to a more intricate, bi-directional network that integrates a variety of distributed energy sources, including renewables, the importance of energy storage becomes more pronounced. Energy storage provides building managers with the flexibility to adjust demand, a key feature for buildings integrated with the grid. This control over energy storage allows for the optimization of energy usage and the ability to feed energy back into the grid, aligning with supply and demand dynamics. This allows for:

- participation in demand response programs run by utilities or transmission organizations such as RTOs or ISOs;
- more refined building energy management, including taking advantage of time of use rates or limiting demand charges;
- better utilization of on-site energy generation resources, such as solar photovoltaics (PVs);
- a backup power source that can be accessed during power outages, potentially enhancing resilience [8].

In conclusion, the incorporation of energy storage systems within buildings emerges as a crucial strategy for navigating the complexities of contemporary energy dynamics. As outlined earlier, these systems contribute significantly to the optimization of renewable energy integration, ensuring a steady and reliable power supply. Their role in load balancing, enhancing grid stability, and providing resilience against disruptions further underscores their transformative impact on the energy landscape within buildings. Considering a future characterized by increased reliance on renewable sources, the imperative of energy storage in buildings becomes increasingly evident, shaping a path toward a more sustainable and resilient energy paradigm.

1.3 Potential of thermal, electricity and hydrogen storage systems for achieving sustainable buildings

Recognizing the significant energy consumption by the building sector within the overall energy landscape, numerous governments and international bodies have initiated policies and objectives to reduce the energy demand and greenhouse gas (GHG) emissions of buildings. A key strategy in this endeavour is the concept of net-zero energy buildings (NZEBs). NZEBs are designed to produce as much energy as they use over the course of a year, requiring a careful integration of energy-efficient measures and renewable energy systems, a task that presents numerous challenges. To reach NZEB goals, it is also essential to incorporate energy storage systems (ESSs). Buildings can utilize three primary storage methods: electrical, thermal, and hydrogen. These storage systems are crucial for matching energy supply with demand for thermal energy, electricity, and hydrogen in buildings. They

allow for the accumulation of excess energy generated during periods of surplus production. This energy can be released when demand peaks, easing the burden on the power grid and enabling cost reductions for consumers by lowering energy bills. Furthermore, energy storage systems are integral in reducing carbon emissions since they decrease the reliance on fossil fuel-based power generation during times of high energy demand.

The electrical ESS category predominantly comprises batteries capable of efficiently storing electricity obtained either from the grid or renewable sources like solar, wind, and geothermal energy. By harnessing these renewable energy resources, batteries serve as indispensable reservoirs, ensuring a reliable and consistent power supply to meet the building energy demands while reducing reliance on conventional grid-based electricity. Nevertheless, the application of batteries continues to encounter certain obstacles, especially concerning their high capital cost, short lifespan, and susceptibility to some weather conditions.

Hydrogen storage systems (HSSs) are distinct from batteries in several key aspects, including their operational principles, energy storage density, refuelling or charging processes, efficiency, and potential uses. HSSs, for example, possess a greater energy storage capacity and exhibit a reduced rate of energy leakage compared to batteries. Moreover, hydrogen has the capability to be burned or used in fuel cells to generate electricity, effectively catering to a range of functions within residential buildings, such as operating HVAC systems, electricity generation, and providing domestic hot water [5]. Conversely, batteries are generally more efficient, with efficiency rates ranging from 80–95%, as opposed to the 40–60% typical of HSSs. The efficiency of HSSs is influenced by a variety of factors, such as the methods of hydrogen production, its storage, and the conversion technologies employed, including fuel cells. Direct electricity usage tends to be more energy-efficient and cost-effective compared to hydrogen-based systems. This is attributed to the significant energy requirements, energy losses, and the substantial investment costs associated with components like fuel cells, electrolyzers, and hydrogen storage tanks.

Thermal energy storage systems (TESSs) can integrate a variety of passive features and renewable technologies. Passive systems like phase change materials (PCMs), trombe walls, thermal mass, and solar chimneys can be implemented to lessen reliance on active heating and cooling systems. The effectiveness of these passive TESSs is contingent upon several variables, including geographic location, local climate, and the architectural attributes of the building. On the other hand, renewable-based TESSs, such as geothermal systems and solar thermal collectors, allow for the accumulation and utilization of energy from sustainable sources. The challenge, however, lies in the initial costs of these thermal storage technologies, which can represent more than half of the total capital investment required for renewable energy facilities [9].

1.4 Advancing hydrogen storage: a synthesis of contemporary research and technological feasibility

Hydrogen storage, a beacon among energy storage technologies, stands prominently for its exceptional specific energy. Its potential as a sustainable energy carrier is pivotal in the battle against global warming. The utility of hydrogen is extensive; it not only powers vehicles

through fuel cells and hydrogen-fueled internal combustion engines, but also serves industrial and residential purposes. Uniquely, hydrogen can store and produce electricity over long periods, a clear advantage over batteries, which falter in extended storage capabilities. The transformation of hydrogen into electricity and heat is notably straightforward and environmentally benign. This is made possible through a suite of technologies for splitting water into hydrogen and oxygen, such as electrolysis, photochemical water decomposition, and thermochemical water decomposition, each offering a pathway to tap into hydrogen clean energy potential [10].

Aiche-Hamane et al.'s [11] exploration into the wind-powered hydrogen production in Algeria's Ghardaia region stands as a testament to the adaptability of hydrogen production methods to local environmental conditions. The research emphasized the crucial role of wind turbine hub height, discovering a significant variance in hydrogen production: a 10 kW wind turbine coupled with a 5 kW electrolyzer yielded 1600 Nm^3 at a hub height of 10 meters and an enhanced 3200 Nm^3 at 30 meters annually. This finding was crucial as it revealed the direct impact of hub height on maximizing hydrogen production while considering the installation costs. The study also shed light on the seasonal variability in production, with spring witnessing the highest output due to favorable wind speeds, and autumn showing a decline, reflecting the system responsiveness to the fluctuating availability of wind energy.

Further south, in Italy, Fragiacomo et al. [12] offered an in-depth technical-economic assessment of a proton exchange membrane (PEM) hydrogen production system energized by both the grid and renewable energy sources, including wind and solar. This comprehensive study spanned three distinct Italian regions, exhibiting a nuanced picture of hydrogen production potential across diverse landscapes. They reported daily hydrogen production rates with significant differences: Capo Suvero led the way with 287 kg/day, followed by Cosenza at 180 kg/day, and Civita trailing at 22 kg/day. The study illuminated the integral role of renewable energy, with the share of renewables in hydrogen production ranging impressively from 45–77% in Cosenza, a remarkable 87–90% in Civita, and a consistent 75–77% in Capo Suvero. The study simulated PEM electrolyzer showcased specific power consumption metrics, with values of 58.2 kWh/kg for Capo Suvero, slightly higher at 58.5 kWh/kg for Cosenza, and peaking at 62.3 kWh/kg for Civita, reflecting the varied efficiencies of 57.5%, 57.4%, and 53.53% respectively, attributed to each location's distinct energy profile.

On the international stage, Nguyen et al. [13] carried out a detailed techno-economic analysis of large-scale electrolytic hydrogen production facilities operating within the competitive wholesale electricity markets of Canada, California, and Germany. Their study was pivotal in contextualizing the levelized cost of hydrogen, particularly in Ontario, where it was found to be only 6%-27% higher than the cost of steam methane reforming. This marginal difference was indicative of the potential for electrolytic hydrogen to become economically competitive, especially considering advancements in capital cost reductions and operational optimizations. The research highlighted the significant role of smart electricity pricing strategies, such as avoiding peak times, which could further enhance the feasibility of hydrogen production in these markets. Mansir et al. [14] investigated the behavior of renewable energy systems with hydrogen and battery storage for residential applications. Utilizing the TRNSYS software for simulation, their work unveiled that hydrogen storage systems commanded more than twice the capital cost of battery systems. This was largely

due to the high cost of fuel cell components, which are central to the functionality of hydrogen systems. Despite this, hydrogen storage systems were observed to outperform battery systems in terms of efficiency, particularly under higher load conditions, suggesting a more favorable performance in larger applications such as HVAC systems.

Xiang et al. [15] delves into examination and comparison of two energy storage systems, namely Compressed Air Energy Storage (CAES) and Hydrogen Energy Storage (HES), as applied to address the energy demands of 500 buildings in Beijing. The two systems were both designed to harness solar energy, but they differed in their performance metrics. CAES was shown to draw an annual 842 MWh from the grid, significantly less than the 1612 MWh required by the HES system. Yet, when it came to energy and exergy efficiencies, CAES demonstrated a high energy efficiency of 93% compared to HES's 64%, and exergy efficiencies stood at 56% for CAES versus 34% for HES. The study pinpointed areas for improvement, such as the substantial exergy destruction experienced by CAES in its combustion chambers and the considerable losses faced by HES in its electrolyzers. These findings point to the challenges in managing surplus solar energy, especially during the warmer months, which affects overall system efficiency. Completing the narrative, Mosayebi et al. [16] explored the optimal energy scheduling in Smart Energy Hubs (SEHs) faced with electricity price uncertainties. Employing a robust two-layer interval optimization approach, the study integrates Demand Side Management (DSM) and hydrogen storage systems to address uncertainties in energy generation. The analysis reveals economic benefits associated with the incorporation of DSM and hydrogen storage technologies. Case 1, which excludes DSM and hydrogen storage, identifies higher energy generation costs during peak hours. Introducing hydrogen storage in Case 2 results in a commendable 1.48% cost reduction, while Case 3, encompassing both DSM and hydrogen storage, achieves a substantial 5.05% cost reduction. These findings underscore the economic advantages of adopting DSM and hydrogen storage technologies. The study identifies the best trade-off solution in Case 3, emphasizing the optimal balance between average and deviation values. A sensitivity analysis further highlights the effectiveness of DSM and hydrogen storage, emphasizing not only cost savings but also enhanced dispatch reliability.

In summary, the collective knowledge harvested from these studies [11-16] tells a comprehensive story of hydrogen storage technology, underscoring its potential as a versatile and sustainable energy carrier. The narrative weaves through regional and international perspectives, offering a tableau of technical and economic insights that together advocate for the integration of hydrogen in our energy systems. It reflects on the adaptive nature of hydrogen production processes to local environmental conditions, the importance of integrating renewable energy sources, and the significance of strategic energy scheduling and demand management.

1.5 Research question and objectives

Based on the above consideration, the research question of this dissertation is conceptualized as follows: "How might the strategic utilization of off-peak electricity for hydrogen production and storage in building power consumption patterns result in cost reduction and increased sustainability?" In addressing the question, this study explores the feasibility and advantages of implementing a hydrogen (H_2) solution within building structures. Hydrogen, produced during low-cost electricity hours and stored for utilization during periods of high

electricity demand, presents a promising strategy for cost reduction and heightened sustainability. It is essential to note that the conceptual approach of this thesis revolves around leveraging the significant variations in electricity prices throughout the day or distinct periods. This variability creates a favorable environment for storing hydrogen efficiently during times of economic electricity availability and subsequently deploying it when electricity prices surge, thereby optimizing cost-effectiveness and sustainability within the built environment.

To contextualize this study, the case investigation is situated at the University of Stavanger in Norway and the study considers the load and consumption data of the building, coupled with a consideration of the electricity price in the region. Notably, in Norway, an impressive 98% of electricity production is derived from renewable sources: hydropower is the source of most of the production with the share of 88.2% and the wind power with 10.1% of the whole electricity production as can be seen in Figure 1.2 [17]. Thus, in this setting, harnessing the power grid to produce hydrogen during periods of renewable energy abundance aligns seamlessly with the nation's commitment to sustainable practices. Consequently, the produced hydrogen can be classified as green hydrogen, offering a clean and environmentally friendly solution.

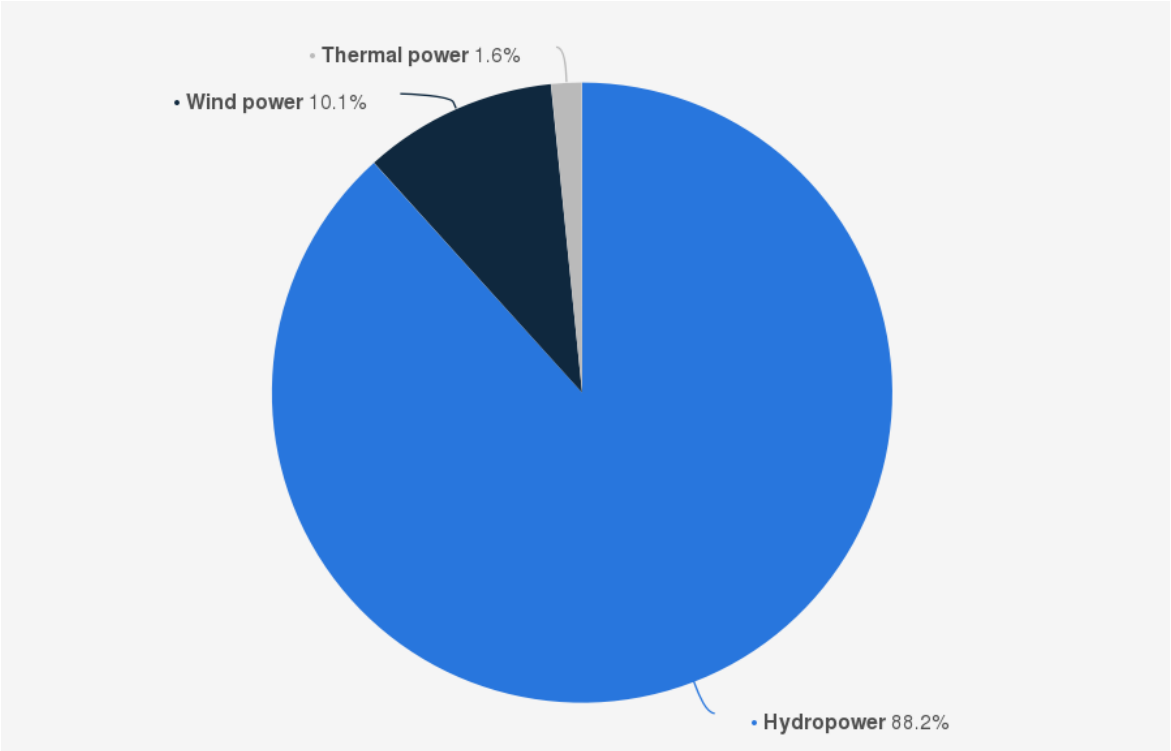

Figure 1.2 Distribution of electricity production in Norway in 2022 [17]

1.6 Outline of the work

The remainder of this thesis is organized as follows. Chapter 2 explores the technologies behind hydrogen production, such as electrolyzers and fuel cells, along with their governing

equations. It provides an in-depth look at how these systems operate and the principles that underpin their functionality. Following this, Chapter 3 details the research methodology, outlining the critical phase that involves the careful development of a comprehensive model using MATLAB Simulink and Simscape. This model is specifically designed for an integrated system that includes an electrolyzer and a fuel cell. The design of this model emphasizes versatility, ensuring that it is suitable for a variety of scenarios and adaptable to different system types. The integrated system is capable of drawing electricity from both conventional grids and renewable sources, including wind and solar power.

The detailed description of this model in chapter 3 unfolds within the methodology section, where each element is systematically elaborated. This detailed explanation not only clarifies the model complexities, but also emphasizes its ability to be adapted for various systems, highlighting its versatility. Following the model development, attention turns to the assessment of an operational system, a critical phase aimed at controlling the integrated system on/off conditions and determining optimal working hours throughout the day. This meticulous evaluation ensures not only the operational efficiency of the integrated system but also its responsiveness to varying demands.

As the research progresses into the results chapter, the focus shifts to a detailed exploration of the integrated system operation. Performance metrics, hydrogen production and consumption, power and efficiency measures are scrutinized, providing a nuanced understanding of the system functionality. Simultaneously, a comprehensive analysis of cost-saving data is presented, shedding light on the economic viability and sustainability of the proposed approach. In essence, this outlined path through the project signifies a systematic and methodical journey, emphasizing the development, assessment, and analytical scrutiny of an innovative integrated system poised to make a substantial impact.

2 Hydrogen production technologies and governing equations

Hydrogen technology, a fundamental element of sustainable energy solutions, holds immense promise for shaping the future of the energy landscape. At the core of this transformative technology lie key components such as the electrolyzer and fuel cell. The electrolyzer, a critical player in the hydrogen production process, facilitates the separation of water into hydrogen and oxygen through an electrochemical process. On the flip side, the fuel cell engages in the reverse process, converting hydrogen back into electricity. While this thesis primarily examines the role of electrolyzers and fuel cells in hydrogen technology, it's important to acknowledge that hydrogen can also be produced through methods like steam methane reforming and partial oxidation. Steam methane reforming is a widely used commercial process that reacts methane with steam to produce hydrogen and carbon dioxide. Partial oxidation, on the other hand, partially burns hydrocarbons in the presence of oxygen to form hydrogen. These methods are more traditional and are known for their scalability but also come with environmental considerations due to carbon emissions. As we look ahead, hydrogen technology is poised to play a pivotal role in the global transition towards cleaner, more efficient energy systems, offering a promising avenue for sustainable energy solutions and addressing the challenges of climate change. Now, looking closely at the governing equations for the proton exchange membrane (PEM) electrolyzer and the fuel cell helps us understand how they work in detail.

2.1 Electrochemical model of polymer electrolyte membrane electrolyzer

The electrolysis process is naturally not spontaneous. Thus, the conversion from electrical energy to chemical energy through the electrochemical reaction is possible only if the electromotive force provided by the supply, and, consequently, the voltage gradient generated are sufficiently high to cover at least the ideal voltage at open circuit conditions, directly related to the Gibbs free energy of the process. In real operation, the voltage required is higher because of the non-faradaic losses involved in it. These losses determine an activation overvoltage, $V_{act,EL}$, an ohmic overvoltage, $V_{ohmic,EL}$, and concentration overvoltage, $V_{conc,EL}$. The mass transport, the resistance to the flow of protons in the electrolyte membrane and the electric current in the cell components are the main cause of the listed overvoltages [18]. The voltage gradient between anode and cathode is, thus, given by (Eq.2.1):

$$V_{EL} = V_{OC,EL} + V_{act,EL} + V_{ohmic,EL} + V_{conc,EL} \tag{2.1}$$

2.2 Electrolyzer open circuit voltage ($V_{OC,EL}$)

The open circuit voltage, OCV, it is defined the voltage corresponding to null current operating conditions, resulting in absence of losses. According to [19,20], $V_{OC,EL}$ depends on

the reaction electrochemistry with a correction on the pressure. It can be described by the Nernst Equation, reported as follows (Eq.2.2):

$$V_{OC,EL} = E_{Nernst} = E^0 + \frac{RT}{nF} \ln\left(\frac{a_{H_2} a_{O_2}{}^{\frac{1}{2}}}{a_{H_2O}}\right) \tag{2.2}$$

Here, a_{H_2} , a_{O_2} and a_{H_2O} indicate the chemical activities at the catalyst layers respectively of hydrogen, oxygen and water between electrode and membrane (1 for liquid water) with their respective stoichiometric factors. R is the gas constant, T is the cell temperature, n is the stoichiometric coefficient corresponding to the number of electrons moles per hydrogen moles involved in the reaction, here 2. F is the Faraday's constant (96485 C/mol) and E^0 is the standard potential or reversible voltage calculated from the Gibbs free energy (Eq.2.3):

$$E^0 = \frac{\Delta \hat{g}^0(T, p_{\text{ref}})}{nF} \tag{2.3}$$

$\Delta \hat{g}^0$ is the Gibbs free energy of the reaction of hydrolysis in standard conditions (1 atm pressure).

2.3 Overpotentials (electrolyzer)

Before the actual production of hydrogen and oxygen can occur, some irreversibilities present in the system require a higher potential to be overcome. These overpotentials are mainly the activation and the ohmic, and, in minor share, because of the low operating current density, the concentration overpotential [21].

- **Activation overvoltage $V_{act,EL}$**

The first loss to be analyzed is the one responsible for the activation overpotential. This voltage increment hinges on the kinetics of the reactions occurring in the catalyst layer in the anodic and cathodic interface with the electrolyte. On the interface, the formation of an electrical double layer (EDL) takes place by means of the protons produced at the electrode, migrated in the solution and accumulated on the interface. Because of the presence of the electrical double layer, a capacitive behavior occurs at the electrode, opposing the electric field, a resistance to the charge and mass transfer. This phenomenon results in a higher voltage to apply [22].

Following the common approach used in [19], the activation overpotential can be described, both for the anode and the cathode by the Butler-Volmer (B-V) expression, reported as follows (Eq.2.4):

$$V_{act,EL} = \frac{RT}{\alpha_{an} F} \sinh^{-1}\left(\frac{i}{2i_{0,an}}\right) + \frac{RT}{\alpha_{cat} F} \sinh^{-1}\left(\frac{i}{2i_{0,cat}}\right) \tag{2.4}$$

Where α is the dimensionless charge transfer coefficient respectively at the anode and at the cathode, F is the Faraday constant, R is the gas constant, T is the temperature, i is the current density, whereas i_0 represents the exchange current density at the electrodes.

The Butler-Volmer equation is obtained with the assumption of symmetry of the reactions at the electrodes of oxidation and reduction. As a consequence, they consider the same value for the two transfer coefficients. This single value can vary from 0.18 to 0.42, even if often assumed equal to 0.5 [19,23].

- **Ohmic overpotential $V_{ohmic,EL}$**

The second loss with a considerable effect is the ohmic overpotential. The phenomenon behind this irreversibility consists in the electrical resistances encountered by the electron movement in the different parts of the cell (electrodes, GDL, bipolar plates, channels) and, mainly, by the protons moving in the membrane. As explained in [24], the mechanism can be described by the Ohm's law (Eq.2.5):

$$V_{ohmic,EL} = R_{ohmic,tot} * I \tag{2.5}$$

In the equation above the I is the cell current, while $Rohmic,tot$ is the total resistance computed as the sum of the resistances in the electrode and the membrane, as follows (Eq.2.6):

$$R_{ohmic,tot} = R_{el} + R_{mem} \tag{2.6}$$

If the activation losses prevail at low current densities, the voltage increase related to ohmic overpotential is dominant for higher currents densities where the higher production is experienced. For this reason the operational point has to be a trade-off between production and losses [22].

- **Concentration overpotential $V_{conc,EL}$**

The concentration or mass transport overpotential are the result of the concentration variation of the reactants occurring at the interface with the electrodes during the electrolysis. A high current is able, indeed, to alter the rate of the reaction at the catalyst layer. In particular, gas bubbles are generated in these conditions, causing a limitation in mass transport and, thus, a reduction in the reaction kinetics. Due to the larger volume of the oxygen bubbles produced, the main contribution is given by the anodic side, which is, therefore, the only share considered in the modelling [23].The general equation of the overpotential is presented as follows (Eq.2.7):

$$V_{\text{conc},EL} = \frac{RT}{\alpha_{an} nF} \ln\left(\frac{i_L}{i_L - i_{an}}\right) \tag{2.7}$$

The term diffusion overpotential is often used to define this class of irreversibility, focusing the analysis of the causes on the concentration gradient of charge-carriers between the

electrolyte and the electrode. The mechanism is described in better details in [25]. It has been experimentally displayed that the share of this overpotential is significantly smaller than the activation and the ohmic terms, especially at low current densities. Commercial PEM electrolyzers, nowadays, operate at current densities insufficiently high to be affected by mass-transport limitation. Therefore, the concentration contribution is often neglected in these operating conditions [25].In any case, from the equation above, it is possible to see that at larger current densities, its contribution is increasingly significant.

2.4 Material balance (electrolyzer)

The following section explains the mass balance of each species involved in the reactions, to understand the production rate of the hydrogen in relation to the water consumption and oxygen production. The production and consumption rate of the two gases can be described by the Faraday's law (Eq.2.8):

$$\dot{N}_{\text{species}} = \frac{I}{nF} \tag{2.8}$$

Where n is the number of moles generated or consumed for each electron. In the anodic side, the oxidation reaction of the oxygen involves four moles of oxygen per electron and, in parallel, two moles of water. The molar flows, respectively generated and consumed, are then defined as (Eqs.2.9 and 2.10):

$$\dot{N}_{O_2}^{gen} = \frac{I}{4F} \tag{2.9}$$

$$\dot{N}_{\text{H}_2\text{O}}^{\text{cons}} = \frac{I}{2F} \tag{2.10}$$

The generation of the hydrogen in cathode chamber is then computed with the Faraday's law (Eq.2.11):

$$\dot{N}_{H_2}^{gen} = \frac{I}{2F} \tag{2.11}$$

2.5 Energy balance (electrolyzer)

In the equations analyzed in the previous sections, temperature is often present. Therefore, for better understanding the system a thermal balance is added to the study, being aware of the energy required by the nonspontaneous endothermic reaction, provided in the form of electric energy. Following the study presented by [24], the global equation can be written considering the temperature variation as a function of the enthalpy net balance, electric power contribution and heat transfer (Eq.2.12):

$$C_{tot}\frac{dT}{dt} = \dot{H}_{\text{in}} - \dot{H}_{\text{out}} - \dot{Q}_{\text{loss}} + P_{el} \tag{2.12}$$

The term C_{tot} [kJ K] indicates the overall thermal capacity of the whole system taken into consideration. Through the variation of the enthalpy between the incoming and outgoing flows, $\dot{H}_{\text{in}} - \dot{H}_{\text{out}}$, the cooling contribution is taken into account being a function of temperature and pressure. The term $\dot{Q}_{\text{loss}}$ is used in the equation to define the heat losses toward the ambient air through the external wall of the control volume, i.e. the stack. In the literature, the thermal power contribution is imposed (assumed equal to zero, constant or function of the enthalpy difference) or computed by means of the heat transfer equation (Eq.2.13):

$$\dot{Q}_{\text{loss}} = UA(T_{\text{wall}} - T_{\text{amb}}) \tag{2.13}$$

In the last case, the global heat transfer coefficient U [W/m^{2}K] must be known through manufacturer datasheet and correlations. Lastly, P_{el} is the electric power provided by the external generator allowing the process of the electrolysis to occur [22].

2.6 Efficiency (electrolyzer)

In the analysis carried by [26] several ways of computing the efficiencies of the electrolyzer are listed. The following general equation is proposed for the computation of the efficiency for PEM water electrolyzer (Eq.2.14):

$$\eta = \frac{N_{H_2}^{\text{out}} HHV}{E + Q_{\text{cell}} \left(1 - \frac{T_0}{T_S}\right) + Q_{H_2O} \left(1 - \frac{T_0}{T_S}\right)} \tag{2.14}$$

Here, the HHV is the higher heating value of H_2, E is the electric energy input, and Q_{H_2O} refers to the further heating provided to the water by the heat exchanger. The term Q_{cell} refers to the heat generated within the electrolyzer cell itself during operation. This may include both the sensible heat raising the temperature of the cell components and any excess heat resulting from the inefficiency of the electrolysis process.. By means of the temperatures of the environment T_0 and of the external heat source T_S , the distinction in the type of energy between the electric source and thermal source is considered, allowing the addition.

2.7 Electrochemical model of polymer electrolyte membrane fuel cell

PEM fuel cells function through electrochemical reactions to produce electrical energy. In this process, hydrogen gas is supplied to the anode, where it undergoes a catalytic reaction, leading to the release of protons and electrons. The protons traverse through a proton-conducting polymer electrolyte membrane to the cathode, while the electrons flow through an external circuit, generating an electric current. Concurrently, at the cathode, oxygen is introduced, and the protons, electrons, and oxygen combine to form water as the primary byproduct. Within the fuel cell subject, this current is often normalized by the cell active area, A_{cell} , which is the surface area of the electrode/electrolyte interface where the fuel cell reactions take place [27]. This yields the current density (Eq.2.15):

$$i = \frac{I}{A_{\text{cell}}} \tag{2.15}$$

The voltage generated by a PEM fuel cell is a key outcome of this electrochemical process, representing a significant advancement in clean and efficient energy conversion from hydrogen fuel. The actual voltage of fuel cell at the steady state condition can be calculated using the following equation (Eq.2.16):

$$V_{FC} = E_{\text{Nernst}} - V_{\text{act},FC} - V_{\text{ohmic},FC} - V_{\text{conc},FC} \tag{2.16}$$

Equation below is known as the Nernst's equation for a PEM fuel cell and gives the ideal voltage that a fuel cell can deliver at the given conditions. E is often referred to as the Nernst voltage (E_{Nernst}) and is the voltage in the fuel cell if there are no losses present (Eq.2.17).

$$E_{Nernst} = E^0 + \frac{RT}{nF}\ln\left(\frac{a_{H_2}a_{O_2}{}^{\frac{1}{2}}}{a_{H_2O}}\right) \tag{2.17}$$

2.8 Overpotentials (fuel cell)

Overpotentials represent the additional energy required beyond the thermodynamic potential to drive electrochemical reactions efficiently. Three primary overpotentials contribute to the voltage losses in PEM fuel cells: activation overvoltage, ohmic overvoltage, and concentration overvoltage.

- **Activation overvoltage $V_{act,FC}$**

Activation losses are a critical aspect influenced by the Tafel equation, a key component of electrochemical kinetics. The Tafel equation describes the relationship between the activation overpotential and the reaction rate at the electrode-electrolyte interface. In the context of PEM fuel cells, activation losses occur when the electrochemical reactions at the anode and cathode interfaces face barriers that require overcoming for efficient ion and electron transfer. The Tafel equation quantifies the activation overpotential as a function of the exchange current density and the Tafel slope. The activation losses are estimated using the Tafel equation (Eq.2.18):

$$V_{act,FC} = \frac{RT}{\alpha nF}\ln\left(\frac{i}{i_0}\right) \tag{2.18}$$

- **Ohmic overvoltage $V_{ohmic,FC}$**

The principle of ohmic losses is outlined in [27] and it is summarized in the following. one of the general principles of hydrogen fuel cells is that the electrons (e −) and protons (H+) are transported between two spatially separated locations in two different ways. However,

in all real conductors there will be an intrinsic resistance to charge flow. In the transportation of the electrons and protons, the particles will therefore be affected by this resistance. This will occur as a voltage loss over the length of the conductors. The total voltage losses accounted for by the transportation of both electrons and protons are often referred to as the ohmic losses, and are given by (Eq.2.19):

$$V_{ohmic,FC} = R_{ohmic} * I \tag{2.19}$$

where R_{ohmic} [Ohm/cm^2] is called the area specific ohmic resistance and is constant for a given fuel cell. R_{ohmic} is often independent of the current density. The ohmic resistance is however very dependent on the water content in the fuel cell, as water is very central in the mechanism of proton transportation in the Nafion membrane [28].

- **Concentration/mass transport overvoltage $V_{\mathbf{conc},FC}$**

It can be shown that changes in concentrations of the chemical species at the surface of the catalyst layers will affect both the reversible fuel cell voltage (E_{Nernst}) and the activation losses ($V_{act,FC}$). The joint losses which are caused due to these concentration changes are referred to as the concentration losses, V_{conc} . As the concentrations at the electrodes in a fuel cell are related to mass transport mechanisms, these losses are also commonly named mass transport losses.

To determine the concentration losses, it is crucial to understand the parameter named the limiting current density, i_L. This is defined as the current density that will make the reactants concentrations tend toward zero and is therefore the maximum current density which can appear in a fuel cell. Theoretically, there would be two ways of calculating the limiting current density, as there are two different reactant concentrations that can tend to zero. However, since O_2 diffuses more slowly than H_2, the limiting current density will be determined based on the O_2 present in the fuel cell. If both the changes in reversible fuel cell voltage and activation losses are accounted for, the theoretical total concentration losses can be calculated by (Eq.2.20):

$$V_{\text{conc},FC} = \frac{RT}{nF}\left(1 + \frac{1}{\alpha}\right) \ln\left(\frac{i_L}{i_L - i}\right) \tag{2.20}$$

However, it is stated in [27] that the real concentration losses are often larger than the theoretical losses calculated by the equation above. Adjustments to the equation may therefore be done to obtain the correct concentration losses, e.g., by reducing the value of α from the conventional value of 0.5. Eventually could other semi-empirical equations be used. It can be observed from the equation above that the concentration losses become increasingly significant for larger current densities. In detail, the concentration losses tend towards infinity when i tends towards the maximum obtainable current density, i_L.

2.9 Material Balance (fuel cell)

For the flow model of anode and cathode, the model uses mass balance to calculate the inlet and outlet properties of streams. The partial pressures of different species are determined from the properties of the gas streams entering and leaving the system, gas and water crossovers, products formed and depletion of reactants during chemical reactions within the fuel cell stack model. Faraday's law is used to predict the molar flow rate required off the reactants for a specific current (Eq.2.21):

$$\dot{N}_{H_2}^{cons} = \frac{I}{\mathrm{n}F} S_{H_2} \tag{2.21}$$

where, S_{H_2} is the hydrogen stoichiometric ratio for the model [29].

2.10 Energy Balance (fuel cell)

The total energy into the fuel cell is consumed by the electrical power output, heat removed by the coolant, heat loss at the stack surface and energy stored within the stack itself. The stack is regarded as a single thermal mass with a heat capacity. With the assumption of stack temperature being equal to the coolant temperature at the outlet, heat exchanged with the coolant and hence stack operating temperature could be determined. The energy balance modes can be given by (Eq.2.22):

$$C_{tot} \frac{dT}{dt} = \dot{H}_{\text{in}} - \dot{H}_{\text{out}} - \dot{Q}_{\text{loss}} - P_{el} \tag{2.22}$$

where, C_{tot} is the thermal capacitance of the stack, $\dot{H}_{\text{in}}$ is the total power delivered by the fuel to the stack (kW), P_{el} is the power consumed by the electrical load (kW), $\dot{H}_{\text{out}}$ is the heat transferred to the cooling water circulating in the stack (kW), and $\dot{Q}_{\text{loss}}$ is the heat dissipated to the ambient (kW).

2.11 Efficiency (fuel cell)

The net power produced by the fuel cell is the product of current drawn and the voltage generated. Since, average cell voltages are calibrated to define the IV curve here, the net power produced by the stack is obtained by multiplying the cell power to the number of cells in the stack (Eq.2.23):

$$P_{\text{stack}} = (V_{\text{cell}} \cdot I) \cdot N_{\text{cells}} \tag{2.23}$$

For specific power output simulations at steady state, the current (I) is assumed to be constant, which calculates the flow rates of reactants based on the stoichiometry. The voltage is determined by the electrochemical equations summarized above. However, in case of transient analysis, the current and voltage models are independent and are determined by the system controls [29]. Usually stack efficiency is calculated by the following equation (Eq.2.24):

$$\eta_{\text{stack}} = \frac{P_{\text{stack}}}{\dot{n}_{\text{fuel}} \cdot LHV} \tag{2.24}$$

In this equation, $\dot{n}_{\text{fuel}}$ refers to the mass flow rate of the fuel, considering that the LHV is given in joules per kilogram (J/kg). This relationship allows for the calculation of the stack's efficiency based on the mass of fuel consumed.

The exploration of hydrogen technology in this chapter has illuminated the governing equations essential for understanding the intricate workings of the electrolyzer and proton exchange membrane fuel cell. These equations, serving as the theoretical backbone, encapsulate the electrochemical processes crucial for hydrogen production and consumption. The subsequent chapter will delve into the developed model on Simscape, intricately designed to align with these governing equations. This model, which forms the heart of the upcoming discussions, promises a practical and dynamic approach to simulate and analyze the behavior of electrolyzer and fuel cell systems and later is used to take the results conduct the calculations. The seamless integration of theoretical foundations with practical modeling will provide a robust platform for unraveling the complexities and optimizing the performance of hydrogen-based energy systems in the following discussions.

3 Case study and modelling approach

Chapter 3 is dedicated to an exhaustive evaluation of the case study, a living lab located at the University of Stavanger. Initially, the lab's existing infrastructure, prior to the integration of a hydrogen-based energy system, is described to provide foundational insights. Following this, the modelling tool that is used to model the integrated system, which includes an electrolyzer, fuel cell, and hydrogen storage, is detailed. Through this modelling process, a dynamic system is equipped to the case study, laying the groundwork for further analysis. The core of the chapter is the detailed presentation of the model created using MATLAB Simulink with Simscape parts. The role and cooperation of the electrolyzer, fuel cell, and hydrogen storage within the model are explained thoroughly. The chapter ends by looking at the control strategy that manages the daily workings of the system. This strategy is outlined in detail, showing how it decides the daily operation of the fuel cell and electrolyzer, based on things like electricity prices and expected energy use.

3.1 Case study: My-Box building

The considered case study is a building which is located at the Ullandhaug campus of the University of Stavanger, and it is chosen as the case study. The selection of this building is justified by the availability of operational data from diverse local energy conversion technologies and the potential for advancing an integrated energy system that can function as a microgrid. The technical and economic potential of integrating an electrolyzer, hydrogen storage, and a fuel cell has been explored using the Simscape modelling environment. This investigation aims at implementing and managing load shifting and leveraging electricity price differences during different hours of the day to diminish the overall electricity cost of the building.

In 2018, the Energy Lab at the University of Stavanger was established as a platform for students and researchers to investigate local energy production using renewable sources. The building shown in Figure 3.1 comprises five student residences designed for cold climates. The pilot buildings at the university are also unique in the country for incorporating vacuum insulation, a technology long used in freezers and refrigerators. This feature enables compliance with the rigorous Norwegian building regulations outlined in TEK 104 [30]. The container-based dormitories are constructed as smart houses, enabling the control of all electronic devices through smartphones. Two local decentralized ventilation fans equipped with heat exchangers, along with the recycling of heat from grey water (wastewater), contribute to low energy consumption. Additionally, these dormitories offer another advantage as they are designed to be movable and reusable. All of the five apartments in the My-Box building, are located near the Sudeten House on the Ullandhaug campus. The building features several solar panels on the roof and the eastern and western walls of the building, and a wind turbine as its nearest neighbour shown in Figure 3.1.

The University of Stavanger is actively engaged in an ongoing project known as "Future Hub." This initiative involves a close collaboration between the university and local industries to develop energy solutions for the future, with the aim of creating greener and more sustainable houses. The integration of existing renewable energy systems, such as wind

turbine and PV panels, with other energy sources that will be installed later, such as an electrolyzer-fuel cell system, is explored by the project. The objective of the future hub project is to meet the energy demands of structures like the My-Box building, enabling it to function independently ("islanded") and even export excess electricity to the grid during periods of surplus. The “Future Energy Hub” research project at the University of Stavanger invites master’s students to live for free for 6 months in the My-Box building, while they write their master’s thesis. In return, students are expected to contribute to the project making the My-Box even more environmentally friendly.

Figure 3.1: My-box building

What makes the My-Box extra interesting is that there is an interaction between wind and sun and other renewable systems such as an electrolyzer-fuel cell system. In Norway, solar energy production is relatively low during the months of peak electricity consumption. the integration of both solar cells and a wind turbine was intended to contribute to a more balanced and consistent energy production throughout the year; however, due to a lack of modeling and improper placement of the wind turbine, it does not meet the requirement of the load properly. The goal for the solar cells and the wind turbine was to satisfy a portion

of the electricity consumption of the apartments, where the students currently live. Equally crucial to energy production is data collection. This data will serve as the basis for numerous engaging student assignments, research projects, and collaborations with industry and the public sector. Therefore, it is essential to measure energy consumption in the apartments to facilitate optimization [31].

3.1.1 Wind turbine:

A vertical-axis wind turbine (Figure 3.1) has been installed close to the building. The choice of the vertical-axis wind turbine was made because it makes less noise and thereby is more appropriate for urban environment than the horizontal ones. Additionally, it is designed to harness the fluctuating and unstable wind conditions existing in Stavanger. The wind turbine on the campus along with advanced wind measuring equipment allows for model calibration, ensuring that the models accurately reflect real-world conditions.

3.1.2 Solar cells:

Solar cells are located on the facade, 4 panels on the east facing wall illustrated in Figure 3.2: (a)- Roof PV facing south (b)-West-wall PV panels, 4 panels on the west facing wall, and 12 tilted panels on the roof facing toward the south. This configuration ensures optimal energy production during the morning and evening hours, aligning with the periods of peak electricity consumption. A company called “Lyse AS” is also an important supporter and has contributed solar cells to the lab [32].

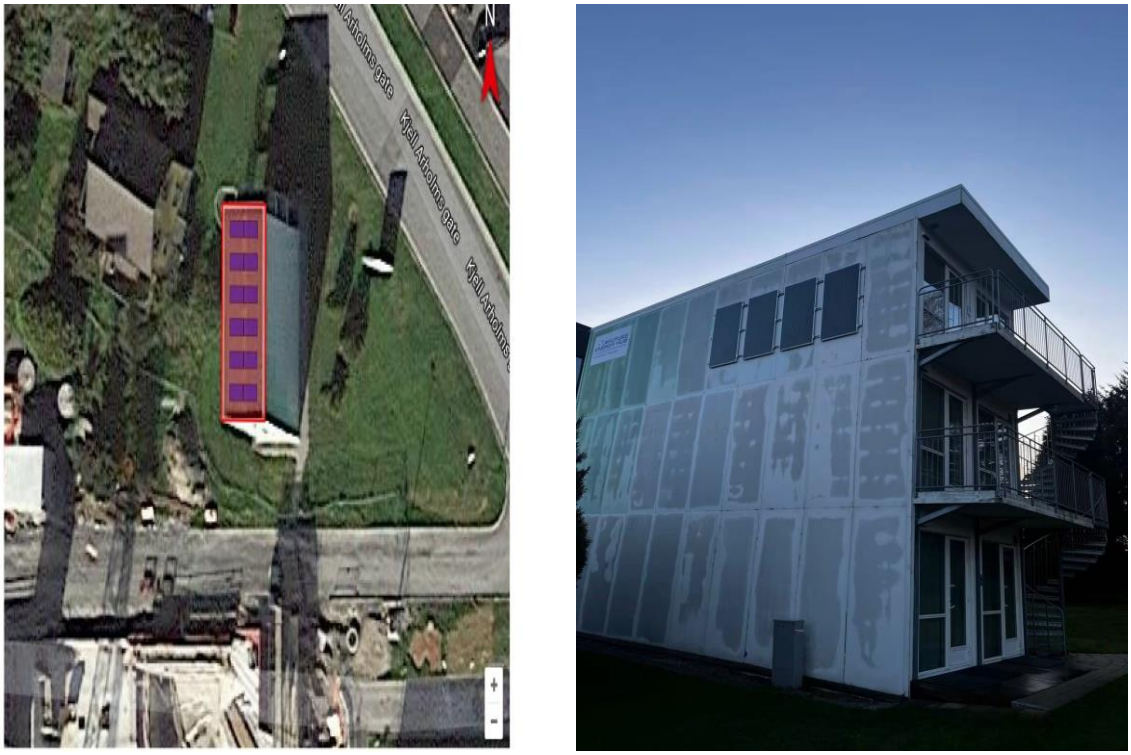

(a) (b)

Figure 3.2: (a)- Roof PV facing south (b)-West-wall PV panels

3.1.3 Environmental and value creation achievements:

The My-Box Energy + Living Lab project at the University of Stavanger holds significant potential for both financial and environmental value creation. Financially, the enhancements will elevate the lab's capacity for more efficient research and innovation, potentially leading to the development of novel technologies and solutions in the realm of renewable energy. These innovations may be commercialized, creating new revenue streams for the university and its industrial partners.

Moreover, the insights derived from the lab can contribute to lowering energy costs and improving energy efficiency, resulting in direct financial benefits for both the university and society at large. For companies collaborating with the university in this project, the lab serves as an opportunity to test and validate their technologies in a realistic environment. This not only expedites the product development process and mitigates risks, but also has the potential to unlock new markets and customers.

The project addresses several key sustainability challenges. First and foremost, it contributes to the transition to renewable energy, which is crucial for combating climate change. Through a focus on local energy production and efficient energy utilization, the project has the potential to diminish reliance on fossil fuels and mitigate CO_2 emissions. Furthermore, by integrating social aspects into the research, the project also addresses the need to create sustainable societies where citizens are actively engaged in energy decisions and have access to clean and affordable energy. For instance, the project ensures that any newly introduced technologies are environmentally friendly and do not lead to unintended negative consequences for the environment or society.

3.2 Modelling tool: MATLAB Simscape

Modelling the electrolyzer and fuel cell system presents a formidable challenge due to the complexity arising from the involvement of diverse domains. The integration of mechanics, thermodynamics, chemical reactions, and control systems adds layers of intricacy to the modeling process. Each domain operates with its own set of principles and interactions, necessitating a comprehensive understanding and effective representation in the model. Furthermore, the dynamic nature of these systems introduces another layer of complexity. The electrolyzer and fuel cell system is subject to continuous changes and fluctuations, requiring the model to account for dynamic responses and adaptability. Achieving accuracy in predicting system behavior under varying conditions is crucial for the model reliability. In addition to domain-specific challenges, considerations such as material properties, environmental factors, and external influences contribute to the complexity. The accurate representation of these elements and different sections of the model is vital for a realistic and reliable model, especially when the aim is to develop a model from a combination of these two systems.

This thesis employs a physics-based approach, opting for a model that describes the system behavior. This choice is intentional, aligning with the aim of tailoring the system design to a specific case study. By using a physical model, the approach ensures a targeted and context-specific solution, capturing the intricacies of the observed phenomena and

addressing the unique challenges presented by the case study. This contributes to the advancement of systems design within the specific context under investigation.

Building a dynamic model of an integrated system of electrolyzer and fuel cell that encompasses the mechanics, thermodynamics, chemical reactions, and control devices of the system can be best carried out in software that provides infrastructure for all those domains and the relations between them. MATLAB Simscape is a powerful tool developed for modelling physical systems that provides the foundation for all physical domains while preserving the freedom to define arbitrary components based on those domains. Figure *3.3* presents the overarching logo of the software, symbolizing a synthesis of diverse domains for modeling purposes.

Figure 3.3: Simscape as a powerful tool for modelling

Simscape, which originated within the renowned Simulink framework, possesses capabilities that simplify the creation of physical system models. Unlike Simulink, where component connections are equation-based, Simscape connections reflect real physical links, creating a model that accurately represents the structure of the actual system. This significantly eases the development of intricate physical networks [33].

Every Simscape model is constructed based on two elements: domains and components. Domains are the definitions of the physical fields of the system, e.g., electrical, gas, magnetic, etc., and are based on declaring “through” and “across” variables. A through-variable is referred to as a type of domain variable that imitates a flow in a domain, whereas a cross-variable is associated with a point in the domain. In the field of electricity, current is an example of a through-variable because it flows through a component. On the other hand, voltage is an across-variable because it is measured across a component. To put it in terms of measurement, a through-variable like current requires a series connection with a measuring instrument such as an ammeter. On the other hand, to measure an across-variable like voltage, you would use an instrument such as a voltmeter, connected in parallel to the circuit, with one lead of the instrument connected to the point of interest and the other to a common reference point, often the ground. [34].

Components represent the actual physical elements that are working in the defined domains. A resistor or capacitor is an example of a physical component. A physical system with a multi-domain background with components that are defined based on more than one domain can be constructed in Simscape. For instance, a DC motor can be defined in the mechanical, electrical, and thermal domains. Figure 3.4 illustrates the presence of libraries containing physical domains and components within the software. Notably, the flexibility of this tool extends to the ability to define custom domains and components through textual files. This feature distinguishes the software from many others, where components and domains are typically pre-defined, allowing only parameter adjustments.

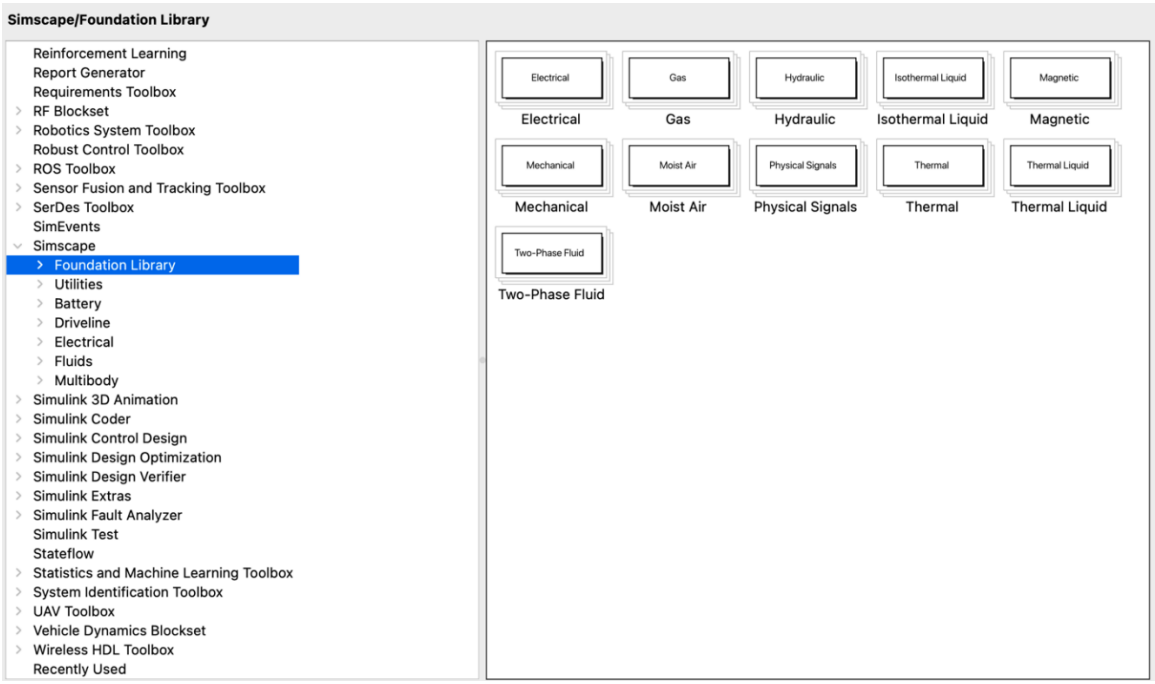

Figure 3.4: Simscape foundation library

Since Simscape has been developed based on Simulink, it is worth describing the advantages of Simscape that make it suitable for modelling physical systems. A model that is constructed with Simscape easily reproduces the actual physical system layout, while in Simulink equations play the main role in constructing the system, which make them more difficult to interpret by people other than the model developer. Moreover, each connection line in Simulink transports a single variable that can be transferred in one direction, while connections in Simscape can simulate bidirectional flow and transferring multiple through-variables in either direction. In addition, the equations and mathematical functions within the components allow acausal modelling and the ability to solve the equations implicitly. Simscape converts the entire network to equations and solves them simultaneously with no order expected. This clearly provides an undemanding method of component definition that is more flexible than Simulink explicit calculation approach. A Simscape model can also connect to Simulink components by converting a physical signal to a Simulink signal and vice versa, which enables the modelling of control systems in a physical system within the Simulink environment [35].

Simscape block diagrams use physical signals instead of regular Simulink signals. Therefore, a converter block is needed to connect Simscape diagrams to Simulink sources and scopes

which is possible with using the Simulink-PS Converter block. It is also possible to use data logging, instead of sensors and scopes, to view and analyze simulation results. Another way to access variables during simulation is to use a Probe block. Adding this block to the model lets us select variables from another block in the model and output them as Simulink signals [36].

In the following section, the developed model will be presented, emphasizing the approach used to construct the various subsystems and components of the integrated system. The model, developed in MATLAB Simscape, can be universally applied to any scenario involving an integrated system of electrolyzer and fuel cell. This versatile model is constructed using Simscape example libraries, showcasing its adaptability and applicability across diverse applications. The system is engineered to operate within predefined parameters across various time periods, with the added flexibility to adjust these parameters to adapt to specific needs in a given case.

3.3 Developed model on MATLAB Simscape

Before delving into the details of the model, it is crucial to note that it is essentially composed of two main sections: the electrolyzer and the fuel cell. Both sections are intricately designed, encompassing different physical aspects. To manage this complexity, a stepwise approach is taken. Initially, each part is individually designed using MATLAB libraries to accurately capture their unique dynamics. Once these two parts are well-crafted, they are seamlessly integrated. The connection between them is facilitated by the hydrogen storage component, acting as a bridge. This component is filled by the electrolyzer and depleted by the fuel cell, illustrating their dynamic interaction. The model, as a whole, remains both consistent and dynamic, offering a representation of how the system behaves.

The modelling approach for the integrated system of an electrolyzer and a fuel cell in MATLAB Simscape varies between 0D and 1D depending on the component. 0D models, or lumped parameter models, assume that all properties are uniform across a component and do not change with position, leading to ordinary differential equations based on time. An example of this is the moisture source (MA) block, which adds or removes moisture at a uniform rate without accounting for spatial variations within the moist air volume. Conversely, 1D models allow for property variations along a single spatial dimension and are described by partial differential equations that track changes over both time and space. This is seen in the pipe (TL) block, where fluid dynamics such as pressure drops and heat transfer are dependent on the length of the pipe, thereby introducing spatial variation in one dimension.

The choice of modelling dimensionality is based on the physical phenomena being simulated and the level of detail required. For instance, fluid flow through pipes where pressure waves or thermal gradients are significant is best captured by 1D modelling. On the other hand, when simulating the overall behaviour of a system where such detailed spatial resolution is not required, 0D models are sufficient and computationally more efficient. The upcoming sections will dissect each part of the model, providing a detailed breakdown of its intricacies.

3.3.1 Electrolyzer

Two distinct moist air networks are established for the electrolyzer. The anode network comprises nitrogen (N_2), water vapor (H_2O), and oxygen (O_2), symbolizing the oxygen flow. Conversely, the cathode network consists of nitrogen (N_2), water vapor (H_2O), and hydrogen (H_2), symbolizing the hydrogen flow. Additionally, a thermal liquid network is employed to represent the water supply, while the thermal network is utilized to simulate the heat generation and cooling processes within the system. Figure 3.5 displays the overall schematic of the system. Subsequent sections will delve into comprehensive explanations of each subsystem.

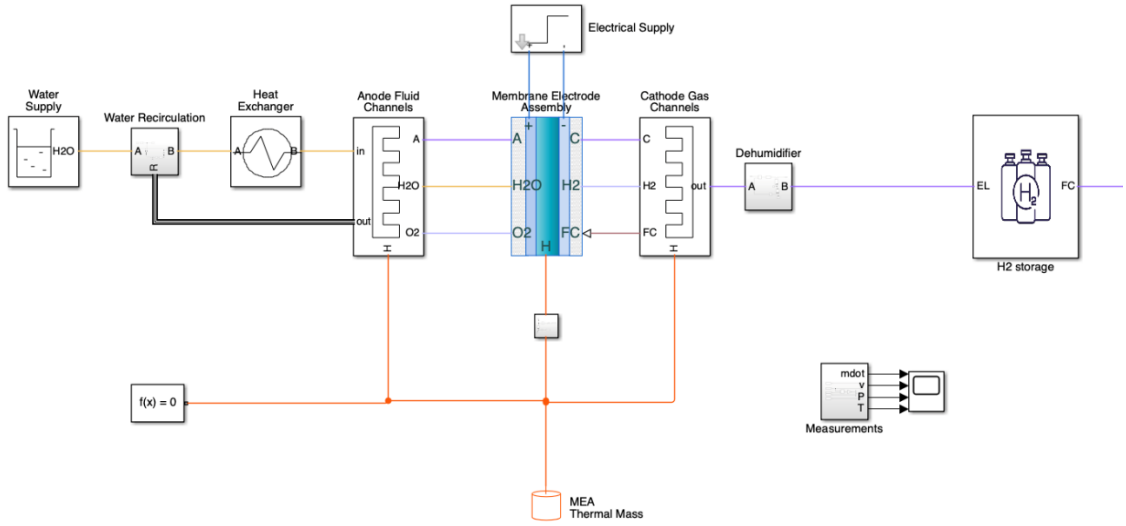

Figure 3.5: The general schematic of PEM electrolyzer model

3.3.1.1 Water supply

In this section, the necessary water for the electrolysis reaction is sourced from a water reservoir situated within a thermal liquid Simscape domain. As it is shown in Figure 3.6, the properties of the water are defined within this domain, allowing for a representation of its characteristics within the system.

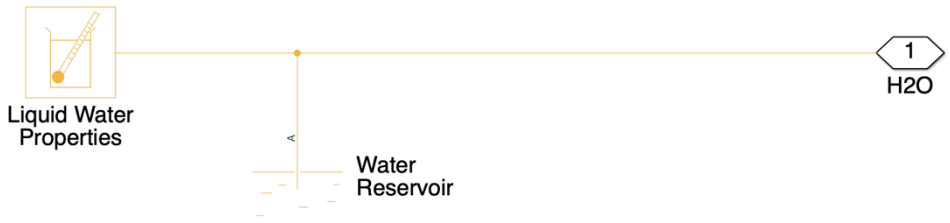

Figure 3.6: Water supply

3.3.1.2 Water recirculation

The produced oxygen and excess water both return from the anode through port R. The water is redirected to the thermal domain for recirculation, while the oxygen is released directly into the environment. Furthermore, the properties of oxygen are specified in this context as it is shown in Figure 3.7. Following this recirculation, a proportional-integral (PI) control system is developed to manage the mass flow rate of water based on the stack temperature. The control system adjusts the mass flow rate by differentiating between the setpoint temperature of 80 °C and the actual temperature of the stack. Ultimately, the control system issues commands to the circulation pump which provides a continuous flow of water to the anode side of the electrolyzer.

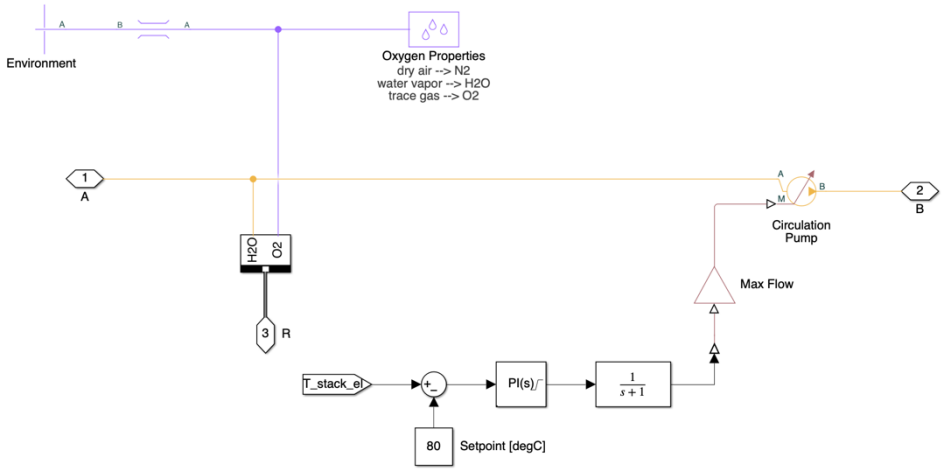

Figure 3.7: Water recirculation

The circulation pump is a flow rate source in thermal liquid domain which is used in many sections of the model, it represents an ideal mechanical energy source in a thermal liquid network. The source can maintain the specified mass flow rate or volumetric flow rate regardless of the pressure differential. There is no flow resistance and no heat exchange with the environment. The volumetric flow rate and mass flow rate are related through the following expression (Eq.3.1):

$$\dot{m} = \begin{cases} \rho_B \dot{V} & \text{for } \dot{V} \geq 0 \\ \rho_A \dot{V} & \text{for } \dot{V} < 0 \end{cases} \tag{3.1}$$

As we can see the mas flow rate is shown with $\dot{m}$, ρ_A and ρ_B are the densities at port A and B respectively. $\dot{V}$ is the volumetric flow rate. The energy balance at the source is a function of the energy flow rates through ports A and B and the work done on the fluid (Eq.3.2):

$$\Phi_A + \Phi_B + \Phi_{\text{work}} = 0 \tag{3.2}$$

ϕ_{A} is the energy flow rate into the source through port A, ϕ_{B} is the energy flow rate into the source through port B and ϕ_{work} is the isentropic work done on the fluid which is shown as (Eq.3.3):

$$\Phi_{\text{work}} = \dot{m}\left(\frac{p_B - p_A}{\rho_{\text{avg}}}\right) \tag{3.3}$$

ϕ_{work} is the isentropic work done on the thermal liquid, p_{A} is the pressure at port A, p_{B} is the pressure at port B, ρ_{avg} is the average liquid density which can be shown as the following (Eq.3.4) [37]:

$$\rho_{\text{avg}} = \frac{\rho_A + \rho_B}{2} \tag{3.4}$$

3.3.1.3 Heat exchanger

In this section, a thermal liquid pipe serves as a heat exchanger as shown in Figure 3.8. This pipe is linked to the convective heat transfer block, which is characterized by the defined area of the pipe and its heat transfer coefficient. Subsequently, it connects to a temperature source block, simulating the environmental conditions. The energy conversion equation of the pipe is as the following (Eq.3.5):

$$V\frac{d(\rho u)}{dt} = \Phi_A + \Phi_B + Q_H \tag{3.5}$$

Φ_{A} and Φ_{B} are the total energy flow rates into the pipe through ports A and B, Q_{H} is the heat flow rate into the pipe through the pipe wall and V is the pipe fluid volume. The heat flow rate between the thermal liquid and the pipe wall is (Eq.3.6):

$$Q_H = Q_{\text{conv}} + \frac{kS_H}{D}(T_H - T) \tag{3.6}$$

Q_H is the net heat flow rate, Q_{conv} is the portion of the heat flow rate attributed to convection at nonzero flow rates. k is the thermal conductivity of the thermal liquid in the pipe. S_H is the surface area of the pipe wall, the product of the pipe perimeter and length. T_H is the temperature at the pipe wall. Assuming an exponential temperature distribution along the pipe, the convective heat transfer is (Eq.3.7):

$$Q_{\text{conv}} = |\dot{m}_{\text{avg}}| c_{p,\text{avg}} (T_H - T_{\text{in}}) \left(1 - \exp\left(-\frac{h_{\text{coeff}} S_H}{|\dot{m}_{\text{avg}}| c_{p,\text{avg}}}\right)\right) \tag{3.7}$$

$\dot{m}_{\text{avg}}$ is the average mass flow rate from port A to port B, $c_{p,\text{avg}}$ is the specific heat evaluated at the average temperature, T_{in} is the inlet temperature depending on flow direction. The heat transfer coefficient, h_{coeff}, depends on the Nusselt number which is the following (Eq.3.8)[38]:

$$h_{\text{coeff}} = \frac{Nu \cdot k_{\text{avg}}}{D} \tag{3.8}$$

where k_{avg}, is the thermal conductivity evaluated at the average temperature. The Nusselt number depends on the flow regime. The Nusselt number in the laminar flow regime is constant and equal to the Nusselt number for laminar flow heat transfer parameter value and for the turbulent flow other correlations are used.

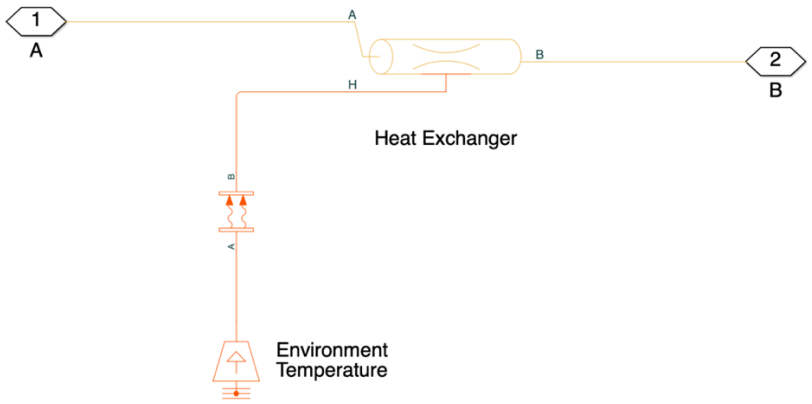

Figure 3.8: Heat exchanger

3.3.1.4 Electrolyzer anode fluid channels

In this segment as depicted in Figure 3.9, water is supplied to the membrane electrode assembly through two thermal liquid domain pipes. One pipe transports water from the water supply in preceding subsystems, while the other returns excess water to the water

recirculation section, effectively removing consumed water from the thermal liquid network and recirculating the excess.

The oxygen generated at the anode is carried away by the excess water flow. It is separately modelled in the anode moist air network, which comprises nitrogen (N_2), water vapor (H_2O), and oxygen (O_2). The oxygen is extracted from the S port of a third pipe within this moist air network. This connection facilitates the addition or removal of moisture and trace gas. In this instance, the trace gas, oxygen, is extracted from the MEA and introduced to the pipe via the S port. The properties of the network are shared with the MEA through the top connection.

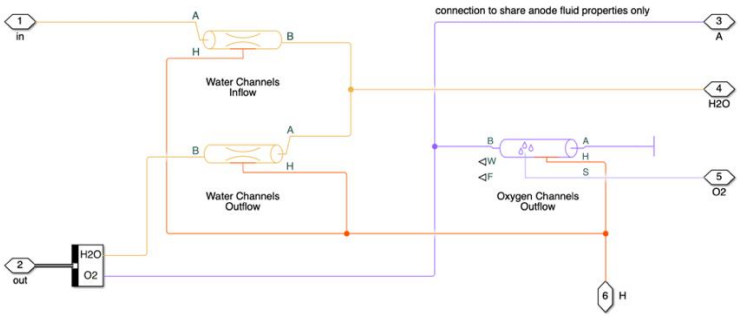

Figure 3.9: Electrolyzer anode fluid channels

Furthermore, all three pipes feature thermal port connections, allowing for the modelling of heat generation within the system and they follow the same equations mentioned for the thermal liquid pipe. Subsequently, they are connected to the thermal mass block which can be seen in Figure 3.5. The application and equation of this block will be explained in the next sections.

3.3.1.5 Electrolyzer membrane electrode assembly

This customized component within the system is connected to both the cathode and anode gas channels, as well as the electrical supply section. It encapsulates all the necessary reactions and equations for the electrolyzer to efficiently split the water atoms into its constituent atoms for hydrogen production. Through this block as indicated by Figure 3.10, users have the flexibility to modify crucial parameters of the electrolyzer, including the number of cells in the stack, cell area, membrane thickness, and more.

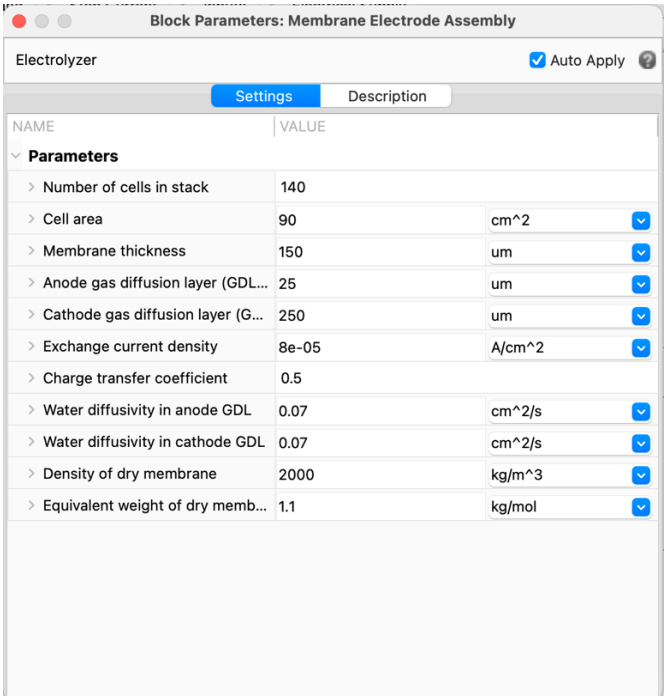

Figure 3.10: *Electrolyzer membrane electrode assembly*

Additionally, the heat generated by these chemical reactions is reported through the thermal port H, ultimately reaching the connected Thermal Mass block.

3.3.1.6 Electrical supply

The electrolyzer system receives commands for the required electrical supply via a Controlled Current Source block. The current is specified as a function of time and is directed to the controlled current source block observable in Figure *3.11*. Additionally, a voltage sensor is incorporated to monitor and report the voltage value within the system.

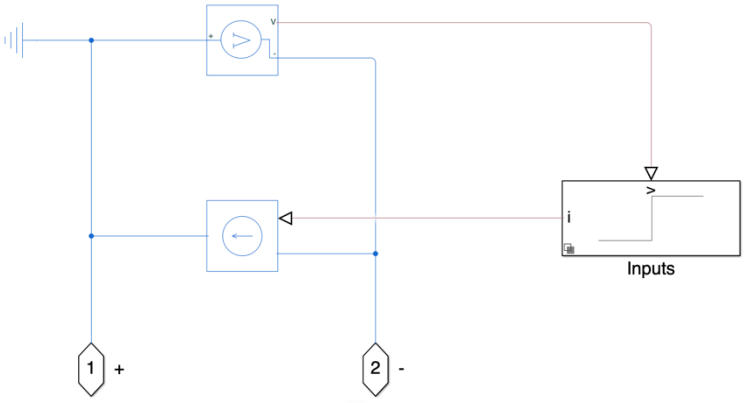

Figure 3.11: Electrical supply

3.3.1.7 Electrolyzer cathode gas channels

Hydrogen generated at the cathode side, along with any water transported across the membrane electrode assembly (MEA), is represented in the cathode moist air network. This network comprises nitrogen (N_2), water vapor (H_2O), and hydrogen (H_2) [39]. In this context, a single pipe is employed, linked to the MEA through the F port to record moist air volume measurements evident from Figure *3.12*. These measurements are crucial for determining gas mole fractions essential for modelling the electrolysis reaction. Furthermore, the pipe features a thermal port connection designed to simulate heat generation within the system, and it is subsequently connected to the Thermal Mass block.

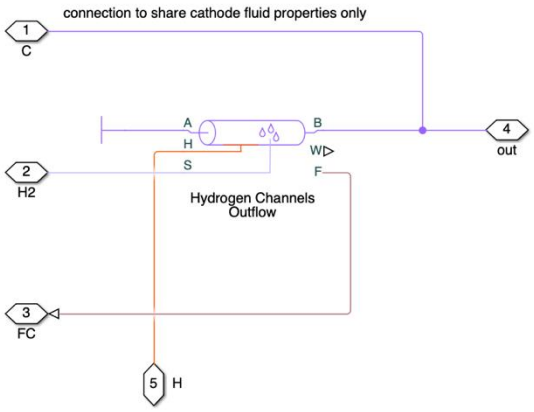

Figure 3.12: Electrolyzer cathode gas channels

This pipe is attached to the MEA through the S port, serving the purpose of introducing or removing moisture and trace gas. In this scenario, the trace gas, hydrogen, is extracted from the MEA block and introduced to the pipe via the S port. The properties of the network are shared with the MEA through the top connection.

3.3.1.8 Dehumidifier

The dehumidifier plays a crucial role in eliminating moisture or water vapor from gases generated during the electrolysis process. Within this setup, a flow rate sensor is employed to measure the water vapor mass flow rate through the Mw port. Subsequently, this signal is directed to the moisture source block, commanding the removal of vapor from the insulated constant volume chamber in the moist air network as illustrated in Figure *3.13*. Additionally, the moist air source is linked to a thermal port to maintain the temperature at the desired level. The moisture source block represents a constant or time-varying source or sink of moisture for the connected moist air volume. A positive or negative moisture mass flow rate results in moisture being added or removed, respectively. For a time-varying source, two physical signal input ports, M and T, supply the mass flow rate and temperature values, respectively. For water vapor, the energy associated with the added or removed moisture is (Eq.3.9) [40]:

$$\Phi_s = \begin{cases} \dot{m}_{\text{specified}} \cdot h_w(T_{\text{specified}}), & \text{if } \dot{m}_{\text{specified}} \geq 0 \\ \dot{m}_{\text{specified}} \cdot h_w(T_s), & \text{if } \dot{m}_{\text{specified}} < 0 \end{cases} \quad (3.9)$$

$\dot{m}_{\text{specified}}$ is the water vapor mass flow rate specified by the input physical signal at port M or by the moisture mass flow rate parameter. h_w is the water vapor specific enthalpy and $T_{\text{specified}}$ is the temperature of added moisture, as specified by the input physical signal at port T or by the block parameters. The block uses this value to evaluate the specific enthalpy of the added moisture only. The specific enthalpy of removed moisture is based on the temperature of the connected moist air volume. T_s is the temperature at port S, which is the same as the temperature of the connected moist air volume.

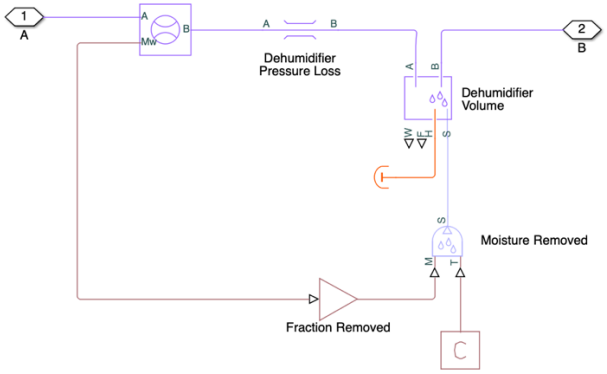

Figure 3.13: Dehumidifier

3.3.1.9 Hydrogen output

In this section, the objective is to store hydrogen. Initially, a pressure sensor provides the pressure value to the PI control system, which regulates and maintains it at 3 MPa. This control system adjusts the pressure by varying the entry area of the local restriction block. Subsequently, the hydrogen properties are defined, and a flow rate sensor is positioned before the entrance of hydrogen into the hydrogen storage with reference to the details in Figure *3.14*.

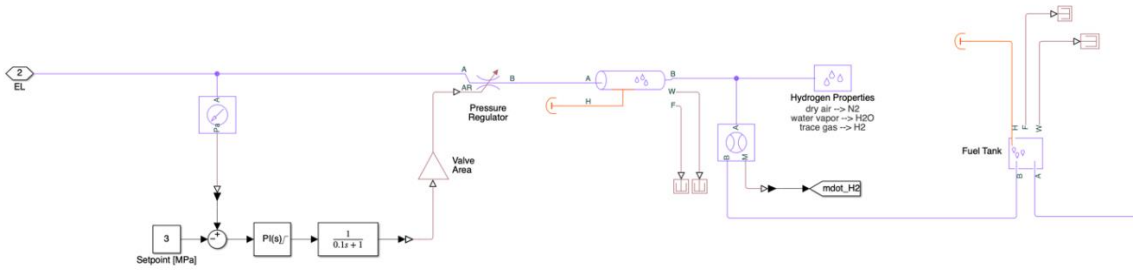

Figure 3.14: Hydrogen output

The hydrogen storage itself is represented as a constant volume chamber, simulating mass and energy storage within a moist air network. This chamber houses a constant volume of moist air, and the pressure and temperature evolve based on the compressibility and thermal capacity of the moist air volume. Furthermore, the chamber is connected to a perfect insulator through its thermal port, effectively preventing heat transfer with the environment. The net flow rates into the moist air volume inside the chamber are (Eq.3.10) to (Eq.3.13):

$$\dot{m}_{net} = \dot{m}_A + \dot{m}_B - \dot{m}_{condense} + \dot{m}_{ws} + \dot{m}_{gs} \tag{3.10}$$

$$\dot{\Phi}_{net} = \dot{\Phi}_A + \dot{\Phi}_B + \dot{Q}_H - \dot{\Phi}_{condense} + \dot{\Phi}_s \tag{3.11}$$

$$\dot{m}_{w.net} = \dot{m}_{wA} + \dot{m}_{wB} - \dot{m}_{condense} + \dot{m}_{ws} \tag{3.12}$$

$$\dot{m}_{g.net} = \dot{m}_{gA} + \dot{m}_{gB} + \dot{m}_{gs} \tag{3.13}$$

Subscripts a, w, and g indicate the properties of dry air, water vapor, and trace gas, respectively that their characteristics can be defined in the hydrogen properties block. Subscript ws indicates water vapor at saturation. Subscripts A, B, H, and S indicate the appropriate port. Subscript I indicates the properties of the internal moist air volume. $\dot{m}_{condense}$ is the rate of condensation, $\dot{\Phi}_{condense}$ is the rate of energy loss from the condensed water. $\dot{\Phi}_s$ is the rate of energy added by the sources of moisture and trace gas. $\dot{m}_{ws}$ and $\dot{m}_{gs}$ are mass flow rates of water and gas, respectively, through port S. The values of $\dot{m}_{ws}$, $\dot{m}_{gs}$, and $\dot{\Phi}_s$ are determined by the moisture and trace gas sources connected to port S of the chamber. Water vapor mass conservation relates the water vapor mass flow rate to the dynamics of the moisture level in the internal moist air volume (Eq.3.14):

$$\frac{d(x_{wI})}{dt}\rho_I V + x_{wI}\dot{m}_{\text{net}} = \dot{m}_{w,\text{net}} \tag{3.14}$$

Similarly, trace gas mass conservation relates the trace gas mass flow rate to the dynamics of the trace gas level in the internal moist air volume (Eq.3.15):

$$\frac{d(x_{gI})}{dt}\rho_I V + x_{gI}\dot{m}_{\text{net}} = \dot{m}_{g,\text{net}} \tag{3.15}$$

Mixture mass conservation relates the mixture mass flow rate to the dynamics of the pressure, temperature, and mass fractions of the internal moist air volume (Eq.3.16):

$$\begin{aligned}\left(\frac{1}{p_I}\frac{dp_I}{dt} - \frac{1}{T_I}\frac{dT_I}{dt}\right)\rho_I V + \frac{R_a - R_w}{R_I}\left(\dot{m}_{w,\text{net}} - x_w\dot{m}_{\text{net}}\right) \\ + \frac{R_a - R_g}{R_I}\left(\dot{m}_{g,\text{net}} - x_g\dot{m}_{\text{net}}\right) = \dot{m}_{\text{net}}\end{aligned} \tag{3.16}$$

Finally, energy conservation relates the energy flow rate to the dynamics of the pressure, temperature, and mass fractions of the internal moist air volume (Eq.3.17):

$$\begin{aligned}\rho_I c_{vI} V\frac{dT_I}{dt} + (u_{wI} - u_{aI})\left(\dot{m}_{w,\text{net}} - x_w\dot{m}_{\text{net}}\right) + (u_{gI} - u_{aI})\left(\dot{m}_{g,\text{net}} - x_g\dot{m}_{\text{net}}\right) \\ + u_I\dot{m}_{\text{net}} = \Phi_{\text{net}}\end{aligned} \tag{3.17}$$

The equation of state relates the mixture density to the pressure and temperature (Eq.3.18):

$$p_I = \rho_I R_I T_I \tag{3.18}$$

The mixture specific gas constant is (Eq.3.19):

$$R_I = x_{aI}R_a + x_{wI}R_w + x_{gI}R_g \tag{3.19}$$

Flow resistance and thermal resistance are not modeled in the chamber (Eq.3.20):

$$p_A = p_B = p_C = p_D = p_I \tag{3.20}$$

When the moist air volume reaches saturation, condensation may occur. The specific humidity at saturation is (Eq.3.21):

$$x_{wsI} = \frac{\varphi_{ws}R_I}{R_w}\frac{p_{wsI}}{p_I} \tag{3.21}$$

φ_{ws} is the relative humidity at saturation (typically 1), p_{wsI} is the water vapor saturation pressure evaluated at T_{I}. The rate of condensation is (Eq.3.22):

$$\dot{m}_{\text{condense}} = \begin{cases}0, & \text{if } x_{wI} \le x_{wsI} \\ \dfrac{x_{wI} - x_{wsI}}{\tau_{\text{condense}}}\rho_I V, & \text{if } x_{wI} > x_{wsI}\end{cases} \tag{3.22}$$

where τ_{condense} is the value of the condensation time constant parameter. The condensed water is subtracted from the moist air volume, as shown in the conservation equations. The energy associated with the condensed water is (Eq.3.23):

$$\Phi_{\text{condense}} = \dot{m}_{\text{condense}}(h_{wI} - \Delta h_{\text{vap}I}) \tag{3.23}$$

where Δh_{vapI} is the specific enthalpy of vaporization evaluated at T_{I} [41].

3.3.1.10 Electrolyzer MEA thermal mass

The thermal mass block serves to depict the thermal capacitance of a system. Thermal mass is indicative of a material's capacity to absorb and retain thermal energy. Analogous to an electrical capacitor storing electrical charge, a thermal mass stores thermal energy. The thermal mass block facilitates the modelling of how heat is stored within a material and subsequently released over time. It captures the internal energy storage in a thermal network by incorporating both the mass of the system and the specific heat of the material. The rate of temperature increase is directly proportional to the heat flow rate into the material and inversely proportional to the mass and specific heat of the material [42]. The mass of the material and its specific heat characterize this property. The thermal mass is described by (Eq.3.24):

$$Q = c\,.\,m\frac{dT}{dt} \tag{3.24}$$

In the abovementioned equation Q is the heat flow, c is the specific heat of the mass material, m is the mass, T is the temperature and t is time. This component is used in the fuel cell section with the same approach as well.

3.3.2 Fuel cell

Two distinct moist air networks are established for the fuel cell. The anode network is comprised of nitrogen (N_2), water vapor (H_2O), and hydrogen (H_2), symbolizing the fuel. On the other hand, the cathode network includes nitrogen (N_2), water vapor (H_2O), and oxygen (O_2), representing air sourced from the environment. The system utilizes a thermal network to model heat generation and cooling processes. Additionally, a thermal liquid network is defined for the cooling system section, serving as the coolant liquid within the radiator. The general schematic of the model is depicted in Figure *3.15*. Subsequent sections will offer detailed elucidations on each subsystem for a more thorough understanding.

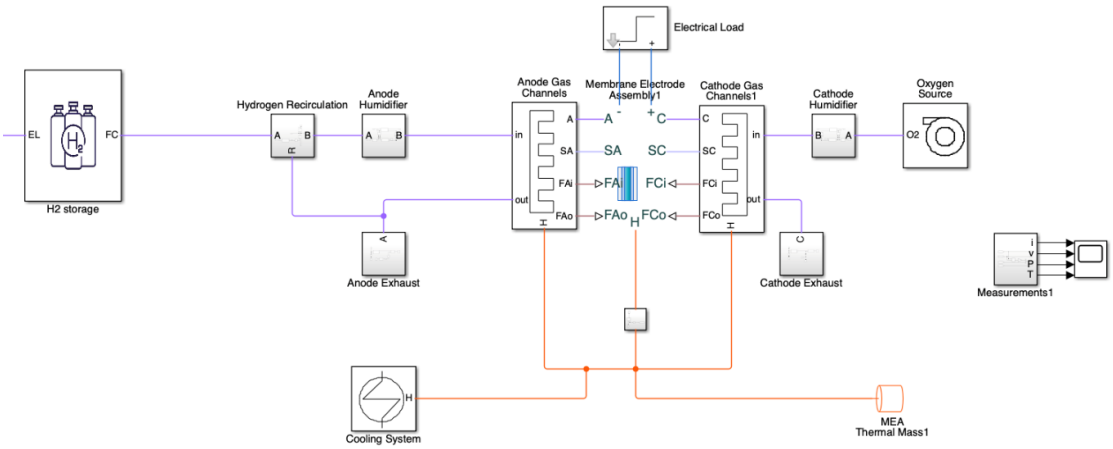

Figure 3.15: The general schematic of PEM fuel cell model

3.3.2.1 Hydrogen source

In this section, a pressure reducing valve system is incorporated following the hydrogen storage as can be seen in Figure *3.16*. The pressure reducing valve is constructed using a local restriction component, allowing the restriction area to be optionally set through the physical signal port AR [m^2]. The specific value for the restriction area is determined by a control algorithm, ensuring that the pressure at port B is maintained around 0.16 MPa. The default state of the valve is open, but it fully closes when the pressure surpasses the set threshold.

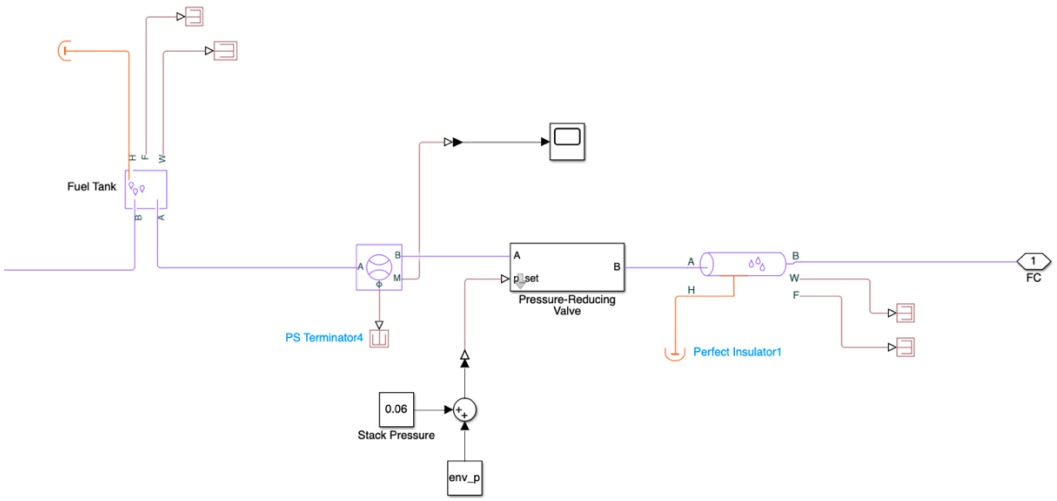

Figure 3.16: Hydrogen source

Subsequent to the pressure-reducing valve, there is an insulated pipe for transferring the fuel and the properties are introduced afterwards. This section plays a critical role in pressure regulation and introduces essential components for managing fuel within the fuel cell system.

3.3.2.2 Hydrogen recirculation

The hydrogen surplus from the anode section undergoes recirculation and returns to this particular section. Here, it is introduced into a constant volume chamber, functioning as a balancing point for the incoming hydrogen flow from the fuel tank, the recirculated hydrogen from the anode, and the continuous flow of hydrogen directed towards the anode side clearly visible in Figure *3.17*.

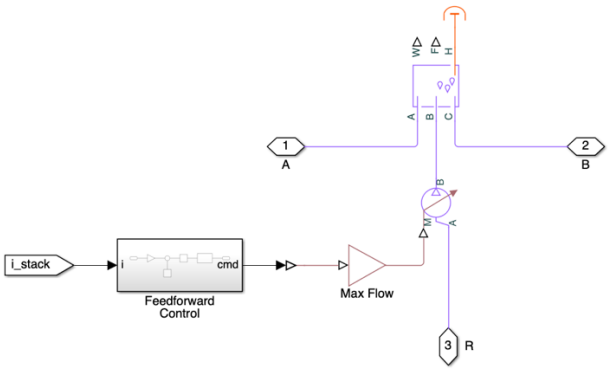

Figure 3.17: Hydrogen recirculation

The recirculated hydrogen is regulated using a feedforward control mechanism, and this regulated value is then sent as a command to a flow rate sensor, which essentially functions as a pump in this context. This arrangement allows for precise control and management of the recirculated hydrogen within the fuel cell system. It is important to note that the flow rate source used in this section has similar equations as the one in water recirculation for section the electrolyzer but in a different domain.

3.3.2.3 Anode humidifier

The anode humidifier in a fuel cell system plays an important role in maintaining the proper moisture level at the anode. Its functions include preventing drying out, optimizing electrochemical reactions, and enhancing the overall efficiency and lifespan of the fuel cell.

Humidifiers are employed to saturate the gas with water vapor, ensuring that the anode membrane stays hydrated. This process helps minimize electrical resistance within the fuel cell, contributing to efficient ion exchange and supporting the electrochemical reactions responsible for generating electricity. PEM fuel cells commonly employ hydrated Nafion

films or other hydrated perfluorinated ionomeric materials as the electrolyte membrane. These membranes need to be properly hydrated in order to achieve maximum performance and extended life. Partial dehydration of the membrane decreases the protonic conductivity and lead to increased resistive loss, decreased net power, and local hot spots that may dramatically reduce the life of the membrane. On the other hand, if excessive water is present in the membrane and/or the gas diffusion layer, a situation that is generally referred as flooding, the fuel cell performance will also be adversely affected due to the water blockage of the flow channels, porous electrodes and backing layers [43]. Therefore, water management was recognized as a critical issue for PEM fuel cell performance.

Observing Figure *3.18* reveals that in this section, there is an insulated pipe that communicates moist air volume measurements through the F port to the measurement selector block. The measurement selector block, in turn, relays moisture levels via port W to the PI control system, responsible for managing the humidity for anode entry. This control system then issues commands to the M port of the moisture source block.

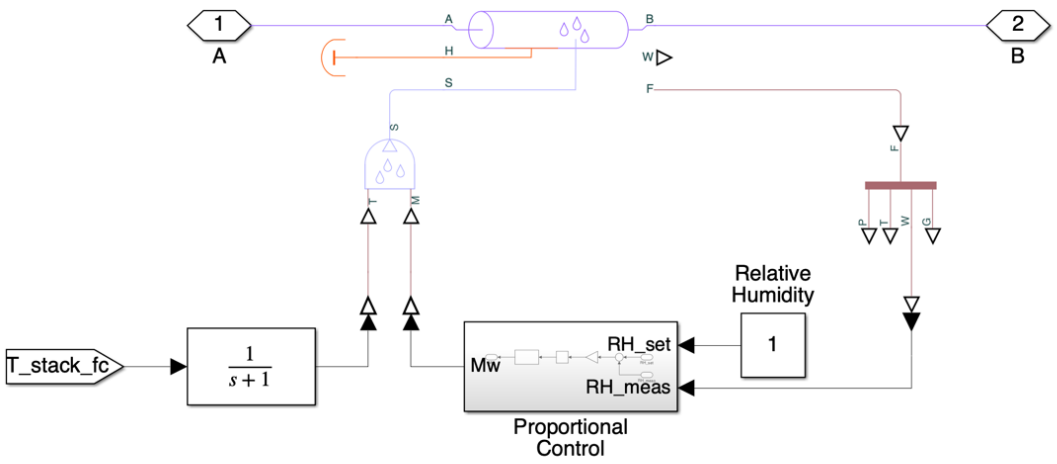

Figure 3.18: Anode humidifier

The moisture source block is connected to the pipe through the S port, which serves as an optional moist air source conserving port for adding moisture. The same equations as the humidifier section for the electrolyzer are valid for this component. Additionally, the temperature of the stack is directed to the pipe through the moisture source block. This integrated control system ensures effective management of both moisture levels and temperature within the fuel cell system.

3.3.2.4 Fuel cell anode gas channels

The anode moist air network consists of nitrogen (N_2), water vapour (H_2O), and hydrogen (H_2), representing the fuel in the moist air domain. In the anode section, hydrogen is consumed, and any excess hydrogen is recirculated back to the stack through the lower pipe, it is important to note that nitrogen does not enter the fuel cell anode and only hydrogen enters from the S port of the pipe. Both pipes are linked to the membrane electrode assembly

through the F port to report moist air volume measurements, essential for determining gas mole fractions necessary for modelling the fuel cell reaction in accordance with the visualization in Figure *3.19*. Additionally, both pipes have thermal port connections designed for modelling heat generation within the system. Following this, they are connected to the thermal mass block.

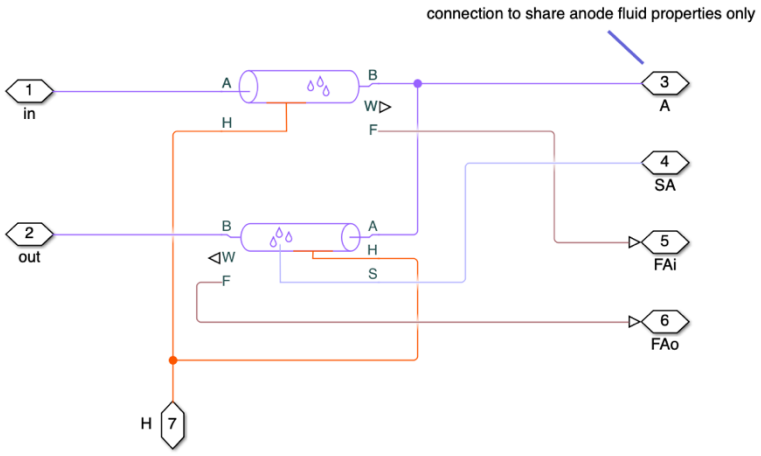

Figure 3.19: Fuel cell anode gas channels

Importantly, only the lower pipe is connected to the MEA through the S port. This connection serves the purpose of adding or removing moisture and trace gas. In this specific case, the trace gas, which is hydrogen, is extracted from the lower pipe and added to the MEA block via the S port. The properties of the domain are shared with the MEA through the connection on the topside.

3.3.2.5 Anode exhaust

In PEM fuel cells, managing the anode exhaust is a critical aspect of ensuring efficient and reliable operation. This exhaust, which primarily consists of unreacted hydrogen alongside water vapor and trace impurities, plays a significant role in the cell's water and thermal management, as well as in maintaining the fuel cell's overall efficiency. By recirculating unreacted hydrogen back into the fuel cell, removing excess water to prevent membrane flooding, and controlling the temperature within the cell, the anode exhaust management system helps in optimizing the performance and extending the lifespan of the PEM fuel cell. Regarding the water management In a PEM fuel cell, water is produced at the cathode as a by-product of the electrochemical reaction between hydrogen (from the anode side) and oxygen (from the cathode side) to produce electricity. A portion of this water will travel through the membrane to the anode side due to electro-osmotic drag and diffusion. Proper management of water content in the anode exhaust is crucial. It helps in maintaining the hydration of the membrane, which is essential for its ionic conductivity and, thus, the overall efficiency of the fuel cell. Excess water must be removed to prevent flooding of the anode, which can impede the access of hydrogen to the reaction sites [44].

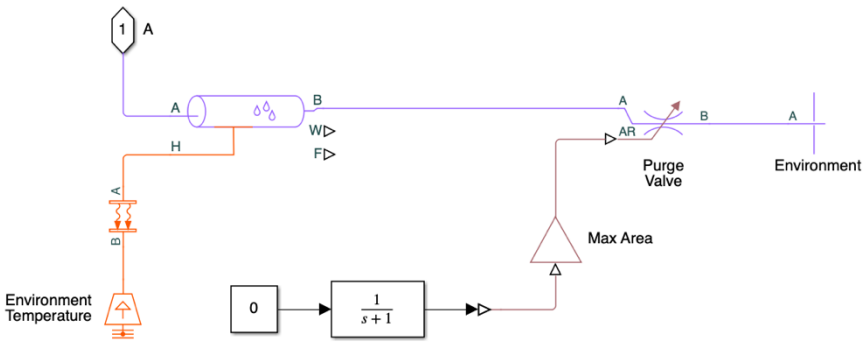

Figure 3.20: Anode exhaust

Based on the representation in Figure *3.20*, there is a pipe that undergoes heat transfer with the environment. Subsequently, the pipe leads to a purge valve, which functions as a local restriction block. The purge valve is responsible for regulating the area of the pipe, and any surplus gas is directed to the environment.

3.3.2.6 Fuel cell membrane electrode assembly

The membrane electrode assembly is a critical component of a fuel cell, especially in proton exchange membrane fuel cells. The MEA is essentially a sandwich-like structure that consists of three main components: a proton exchange membrane, an anode electrode, and a cathode electrode.

This customized component within the fuel cell system is connected to both the cathode and anode gas channels, as well as the electrical load section. It encapsulates all the necessary reactions and equations for the fuel cell to efficiently convert the chemical energy of hydrogen into electrical energy. Through this block with reference to the details in Figure *3.21*, users have the flexibility to modify crucial parameters of the fuel cell, including the number of cells in the stack, cell area, membrane thickness, and more.

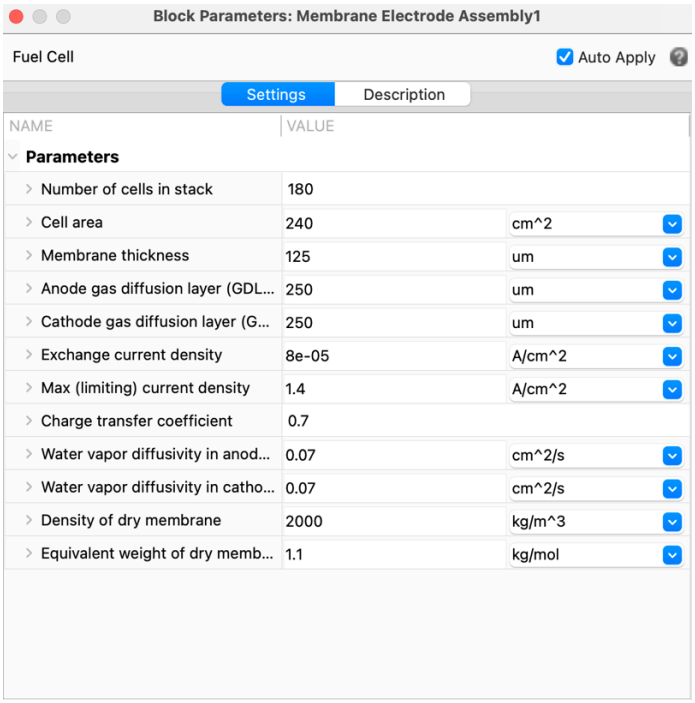

Figure 3.21: Fuel cell membrane electrode assembly

Additionally, the heat generated by these chemical reactions is reported through the thermal port H, ultimately reaching the connected thermal mass block and finally this heat will be cooled by the cooling system developed for the model.

3.3.2.7 Electrical load

The fuel cell system receives commands for the required electrical load through a controlled current source block, as can be seen in Figure *3.22*. The input data for this process is the energy consumption pattern of the building over time. On the other end, the voltage is sensed and reported through a voltage sensor. The output is the required current, which is then communicated as a physical signal to the controlled current source block. This mechanism allows the fuel cell system to adapt and meet the specific current needs dictated by the building energy consumption.

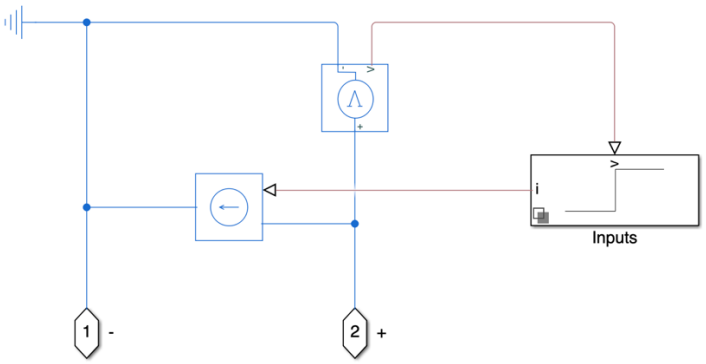

Figure 3.22: Electrical load

3.3.2.8 Fuel cell cathode gas channels

The cathode moist air network consists of nitrogen (N_2), water vapour (H_2O), and oxygen (O_2), representing air from the environment in the moist air domain. In the cathode section, oxygen is consumed, and any excess oxygen is directed to the exhaust through the lower pipe. Both pipes are linked to the membrane electrode assembly via the F port to report moist air volume measurements as illustrated in Figure *3.23*. These measurements are crucial for determining gas mole fractions necessary to model the fuel cell reaction. Additionally, both pipes have thermal port connections, allowing for the modelling of heat generation within the system. Subsequently, they are connected to thermal mass block.

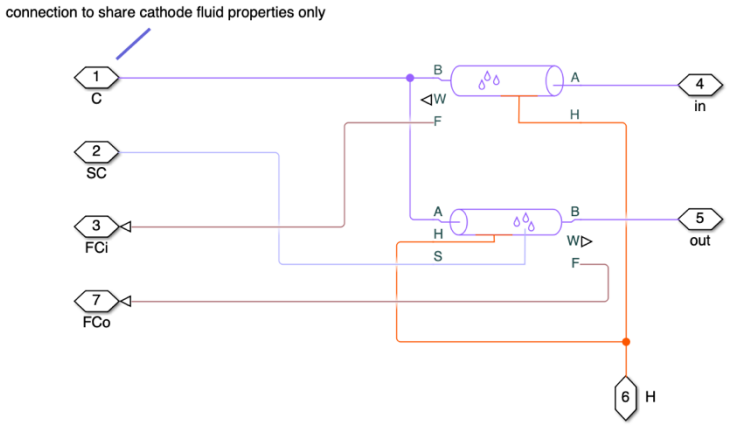

Figure 3.23: Fuel cell cathode gas channels

However, only the lower pipe is connected to the MEA through the S port. This connection serves the purpose of adding or removing moisture and trace gas. In this case, the trace gas,

which is oxygen, is extracted from the pipe and introduced to the MEA block via the S port. The properties of the domain are shared with the MEA through the top connection.

3.3.2.9 Cathode humidifier

The cathode humidifier in a PEM fuel cell serves to manage water content at the cathode, preventing drying out, optimizing electrochemical reactions, and contributing to the overall efficiency and reliability of the fuel cell. Proper water management is crucial for ensuring the longevity and optimal performance of the fuel cell system.

Humidifiers are employed to saturate the gas with water vapor, ensuring that the membrane stays hydrated. This process helps to minimize electrical resistance within the fuel cell, contributing to efficient ion exchange and supporting the electrochemical reactions that generate electricity.

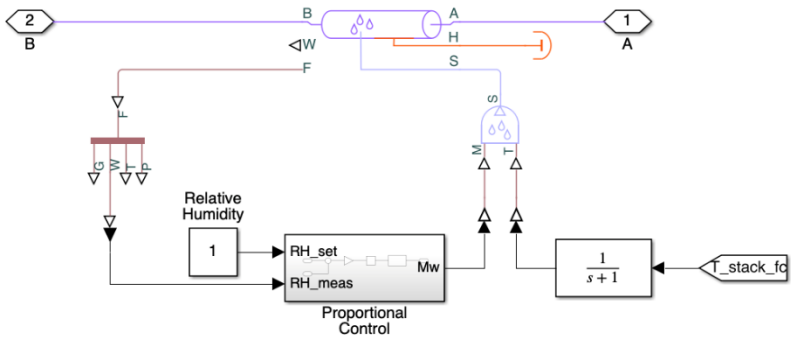

Figure 3.24: Cathode humidifier

In this section observable is Figure *3.24*, there is an insulated pipe that relays moist air volume measurements through the F port to the measurement selector block. The measurement selector block then conveys the moisture level via port W to the PI control system, which regulates humidity for anode entry. This control system issues commands to the M port of the moisture source block. The moisture source block is connected to the pipe via the S port, serving as an optional moist air source conserving port for adding moisture. Additionally, the moisture source block commands the stack temperature to the pipe.

3.3.2.10 Oxygen source

In Figure *3.25* it is evident that in this section a compressor brings air to the fuel cell stack at a controlled rate to ensure that the fuel cell is not starved of oxygen. Following the air intake, represented by a reservoir block, a flow rate sensor functions as a compressor, compressing the air for the subsequent section. It's important to note that the model assumes an isentropic compressor. A flow rate sensor is in place to report the mass flow rate to the compressor control subsystem as feedback. The compressor rotational velocity is then

regulated by the compressor map subsystem. Ultimately, the necessary mass flow rate is directed to the compressor. The air properties are defined within this section.

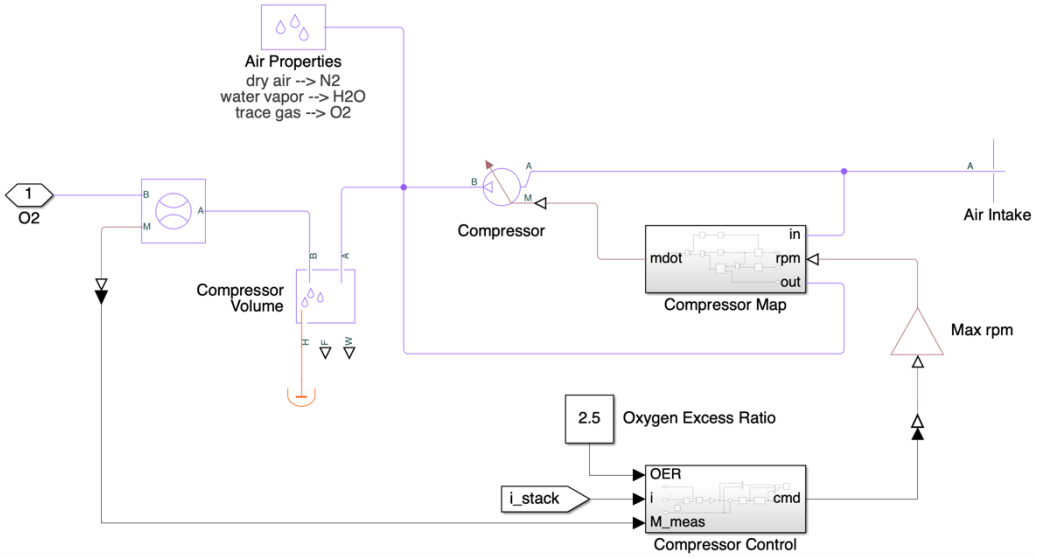

Figure 3.25: Oxygen source

3.3.2.11 Cathode exhaust

The cathode exhaust in a Proton Exchange Membrane (PEM) fuel cell primarily consists of excess oxygen, water vapor, and heat produced during the electrochemical reaction that generates electricity. Its management is crucial for several reasons: to remove the produced water vapor, which helps in maintaining optimal humidity levels within the cell; to expel excess heat, preventing overheating and ensuring the fuel cell operates within its ideal temperature range; and to efficiently use the remaining oxygen, which can be critical in closed or semi-closed systems to maximize resource utilization. Proper handling of the cathode exhaust is vital for the efficient and sustainable operation of PEM fuel cells.

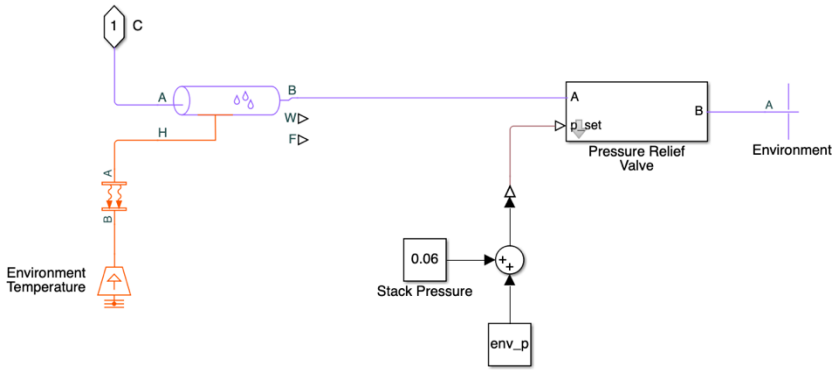

Figure 3.26: Cathode exhaust

In this section as indicated by Figure *3.26*, there is a pipe that exchanges heat with the environment. This pipe is connected to a pressure relief valve, responsible for keeping the pressure in the stack at approximately 0.16 MPa and releasing excess exhaust into the environment. The pressure relief valve subsystem is designed to uphold a predetermined pressure at port A. Normally, the valve remains closed. However, when the pressure surpasses the set threshold, the valve opens to release the excess pressure.

3.3.2.12 Fuel cell MEA thermal mass

The thermal mass block here represents the thermal capacitance of a system and has the same function as the electrolyzer section. Thermal mass is a measure of a material ability to absorb and store thermal energy. This block allows for the precise specification of both the material mass and specific heat, providing a comprehensive representation of the internal energy stored within the material.

3.3.2.13 Cooling system

The temperature in the fuel cell stack must be maintained at an optimal level to ensure efficient operation under various loading conditions. Higher temperatures increase thermal efficiency but reduce relative humidity, which causes higher membrane resistance. Therefore, in this model, the fuel cell stack temperature is kept at 80°C [45]. The cooling system circulates coolant between the cells to absorb heat and rejects it to the environment via the radiator as can be observed in Figure *3.27*.

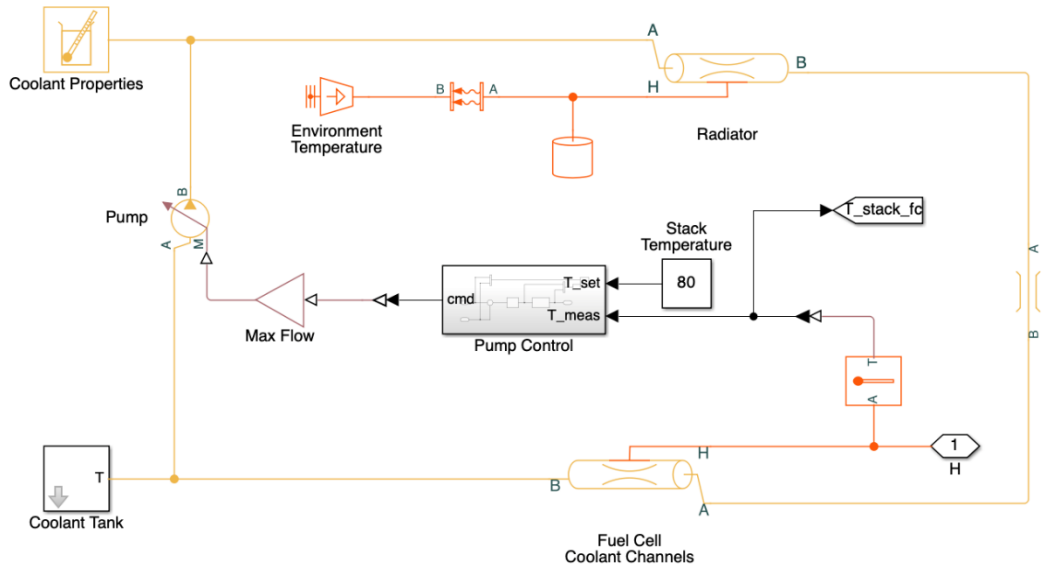

Figure 3.27: Cooling system

The cooling system is designed by integrating the thermal liquid and thermal domains. On one side, port H is connected to a temperature sensor, which reports temperature information

to the pump control system. On the other side, port H is linked to the coolant channels, where the coolant liquid circulates, absorbing heat generated by the fuel cell stack. The coolant is directed to the coolant tank before being pumped into the radiator channels, which are in direct contact with the environment, facilitating convection heat transfer through the radiator fins. The convective heat transfer block is used for this part (that is connected to the environment temperature) which represents heat transfer by convection between two bodies by means of fluid motion [46]. The Newton law of cooling describes the transfer (Eq.3.25):

$$Q = k \cdot A \cdot (T_A - T_B) \tag{3.25}$$

Q is the heat flow, k is the convection heat transfer coefficient, A is the surface area. T_A and T_B are the temperatures of the two bodies. A and B are thermal conserving ports associated with the points between which the heat transfer by convection takes place. Because the block positive direction is from port A to port B, the heat flow is positive if it flows from A to B.

Subsequently, the coolant completes its cycle by returning to the coolant channels, thereby establishing the coolant system. It is noteworthy that in this configuration, water serves as the coolant, and its properties are specified within the thermal liquid domain.

The pump control system has been implemented in Simulink, and it regulates the necessary mass flow rate by transmitting a physical signal to the pump. This regulation is determined by comparing the desired temperature with the temperature detected by the sensor in the fuel cell stack.

3.3.3 Model validation:

Validating the model stands as the crucial stage within the process of model construction. Nonetheless, it is frequently neglected. If the model fails to adequately fit the data, it undermines the primary purpose behind constructing the model initially. The model was validated based on [47] for the electrolyzer and [48] for the fuel cell, through the following process assessment.

3.3.3.1 Electrolyzer

After comparing the experimental data with the predicted data derived from the model, the fitting results are provided in Table 3-1: Fitted model parameters. Regarding the diffusivity of hydrogen protons in water (D_{H^+}), the value obtained from the experimental data aligns with the one acquired from the model. Furthermore, it is noted that hydrogen diffusivity increases with temperature. As illustrated in the following table, D_{H^+} increases as the temperature escalates from 60°C to 80°C.

Table 3-1: Fitted model parameters

Parameter	value	Unit
$i_{0,an,ref}$	5×10-12	A/cm^2
$i_{0,ca,ref}$	1×10-3	A/cm^2
α_{an}	1.2	[-]
α_{ca}	0.5	[-]
D_{H+} (T_{cell}=60 °C)	2.4×10-9	m^2/s
D_{H+} (T_{cell}=80 °C)	3×10-9	m^2/s

Figure 3.28 and Figure 3.29and illustrate a comparison between the results derived from both modelling and experimental trials, utilizing the empirically adjusted parameters outlined in Table 3-1: Fitted model parameters. A slight variation in the polarization curve is noticeable, attributed to the model assumption regarding the insignificance of Ohmic overpotentials in electrodes and plates, which, in reality, do have a limited impact.

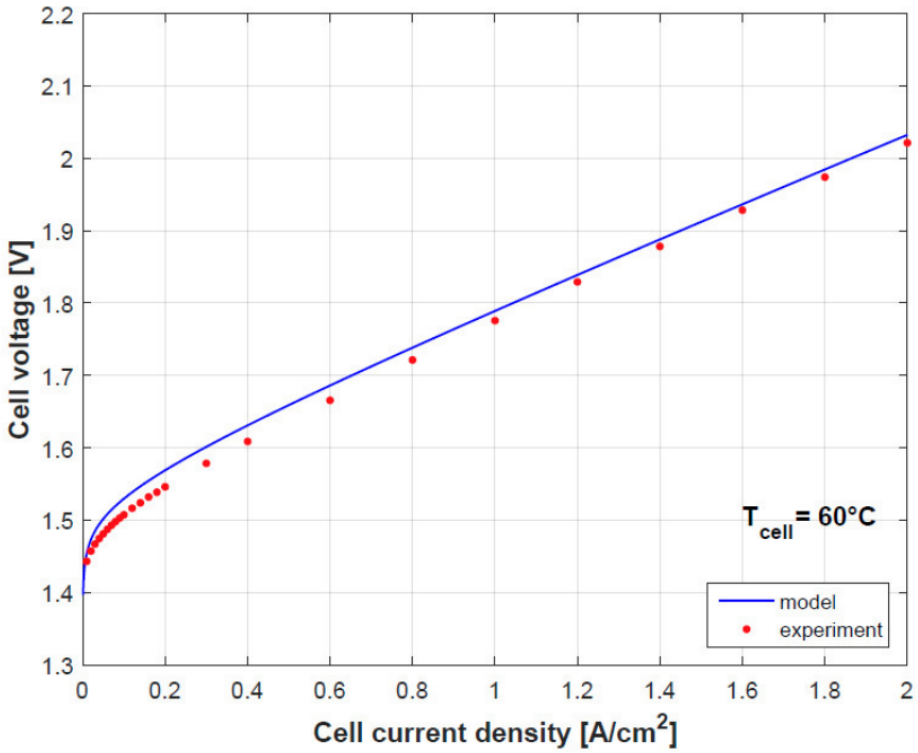

Figure 3.28: Model prediction and experimental data of the cell polarization at 60°C

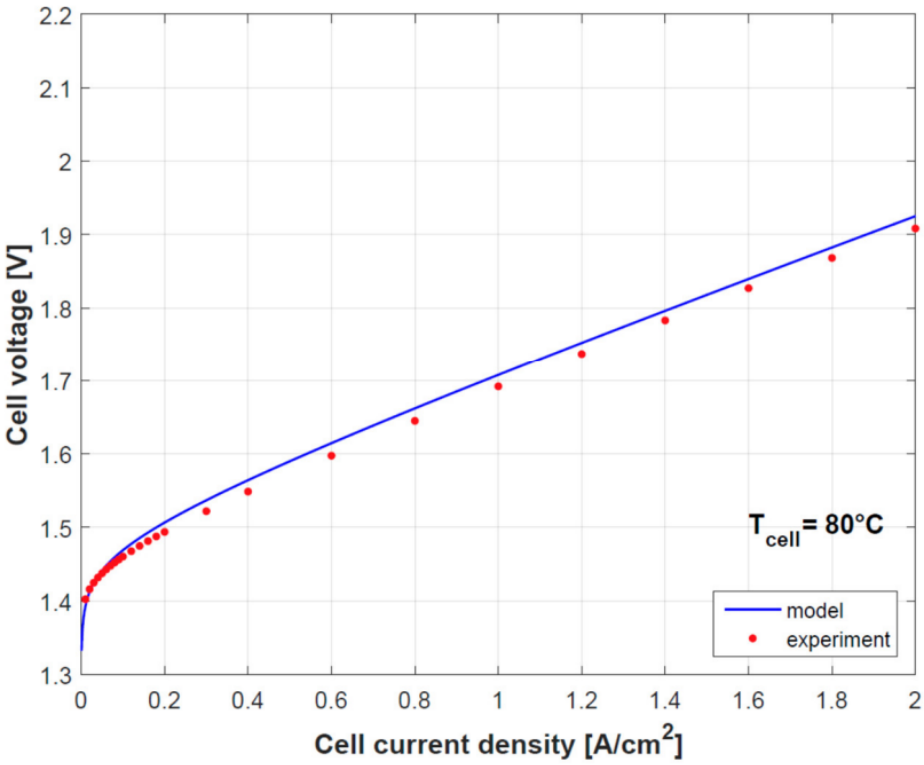

Figure 3.29: Model prediction and experimental data of the cell polarization at 80°C

Figure 3.30, displays the impact of temperature on cell performance. As the operating temperature rises, the Gibbs free energy of the electrochemical reaction decreases, leading to an enhancement in cell performance and energy conversion efficiency.

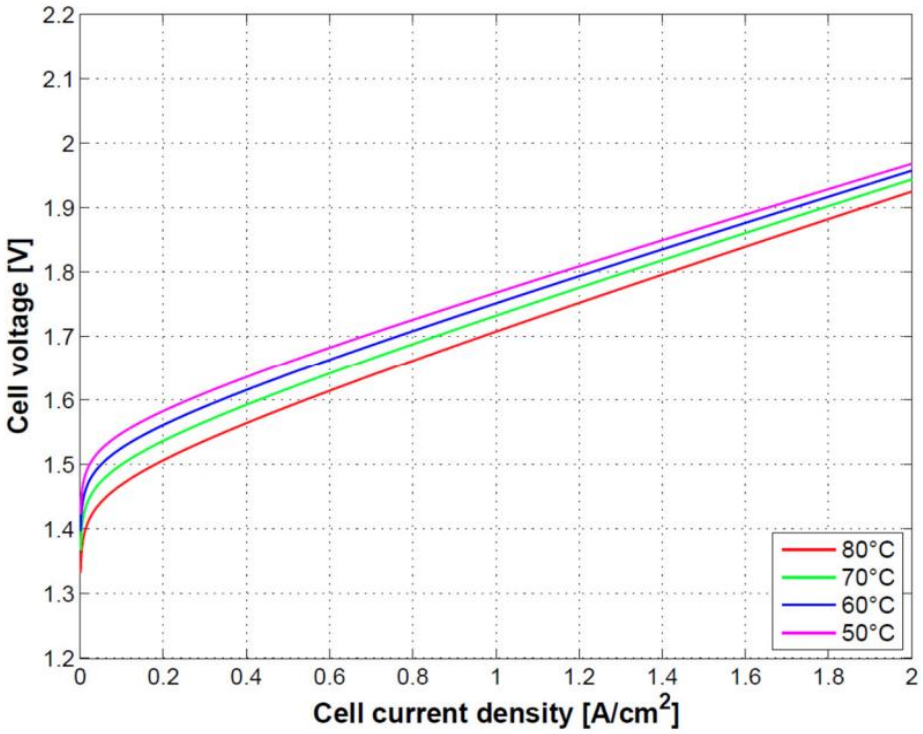

Figure 3.30: Modelling results of the polarization curve at different temperature of operation

Hence, as evident from the previous figures and table, it can be seen that the model was able to reasonably fit the experimental data at two different temperature values i.e., 60 °C and 80 °C.

3.3.3.2 Fuel cell

In the context of model validation, "residual" typically refers to the difference between the observed target values and the predicted values generated by the model. The residual, also known as the prediction error, is the disparity between the actual target values and the values predicted by the model for the same data points. Mathematically, it is often represented as:

$$\text{Residual} = \text{Observed value} - \text{Predicted value}$$

Examining the residuals can provide insights into how well the model fits the data. By analyzing the distribution and patterns of residuals, it can be assessed whether the model assumptions are met, identify areas where the model performs poorly, detect outliers, and decide whether the model needs further refinement or improvement. Determining if there are any specific patterns in the residual data is often done by studying scatterplots. These scatterplots are useful for checking if the errors have a consistent level of variation.

Drifts in the measurement process can be checked by creating a “run order” or “run sequence” plot of the residuals. These scatterplots display each residual plotted against an index that signifies the order (in time) in which the data points were gathered. This method is beneficial when data are gathered in a randomized run order, meaning there is no specific

trend in the arrangement of predictor variables. However, if the data show an increasing or decreasing pattern with the predictor variables, distinguishing process drift from the functional relationship between predictors and the response becomes challenging. Hence, randomization is advocated in experimental design to mitigate this issue.

A parametric model was formulated to predict the performance of a PEM fuel cell across various operating currents and temperatures. The parametric equation forecasts activation overvoltage through a linear regression analysis. Table 3-2shows the run order, experimental temperature, experimental current, calculated experimental activation overpotential, and predicted activation overpotential from the model.

Table 3-2: Experimental and predicted results from model

Run order	Temperature [K]	Current [A]	Experimental activation overvoltage [V]	Predicted activation overvoltage [V]
1	358	2.72	-0.2717	-0.2647
2	328	6.66	-0.4017	-0.4014
3	343	6.66	-0.3522	-0.35
4	358	6.66	-0.3038	-0.3025
5	343	6.66	-0.3341	-0.3283
6	343	6.66	-0.3756	-0.3775
7	328	6.66	-0.3727	-0.3747
8	343	2.72	-0.322	-0.3188
9	343	6.66	-0.3492	-0.35
10	343	6.66	-0.3472	-0.35
11	328	2.72	-0.3141	-0.3193
12	328	6.66	-0.352	-0.3541
13	343	6.66	-0.3482	-0.35
14	358	6.66	-0.3473	-0.3537
15	358	6.66	-0.325	-0.3252
16	358	6.66	-0.3218	-0.3252
17	343	16.33	-0.4075	-0.4083
18	343	16.33	-0.3902	-0.3868
19	343	6.66	-0.3492	-0.35
20	343	6.66	-0.3788	-0.3775
21	358	16.33	-0.3834	-0.386
22	343	2.72	-0.2969	-0.292
23	343	6.66	-0.3249	-0.3283
24	343	2.72	-0.2868	-0.292
25	343	16.33	-0.4453	-0.4379
26	343	6.66	-0.3502	-0.35
27	328	6.66	-0.3793	-0.3747
28	343	16.33	-0.4062	-0.4083

The scatter plot of temperature with respect to the residual is illustrated in Figure 3.31.

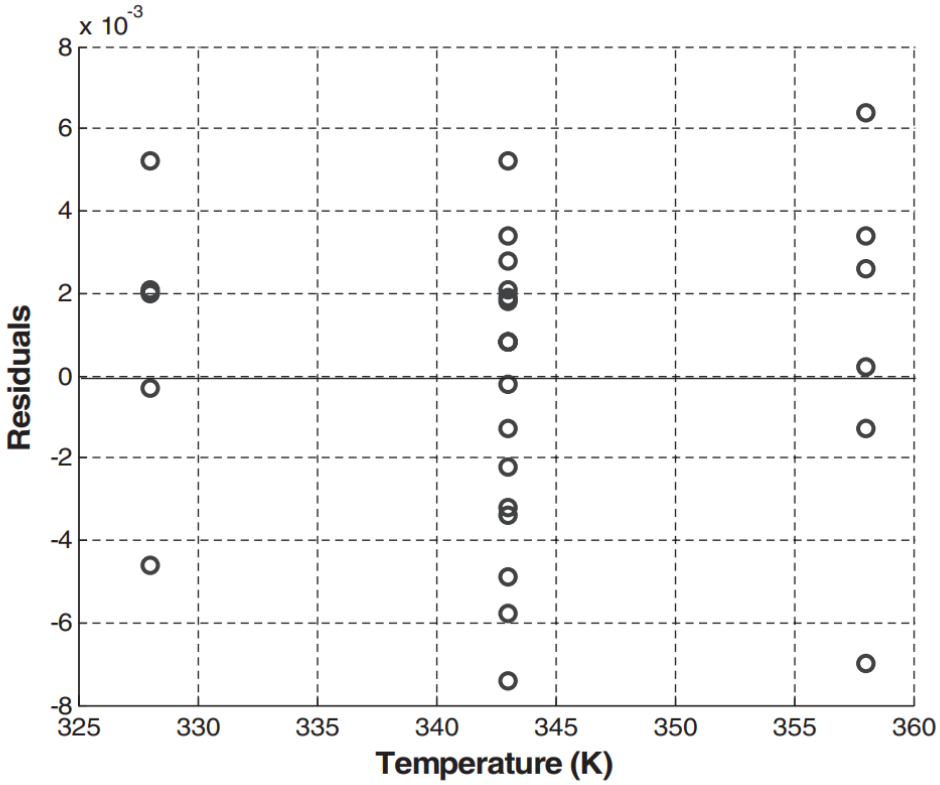

Figure 3.31: Scatter plot of temperature versus residuals

The residuals versus the experimental factor (current) and the run order plot, is displayed in Figure 3.32 and Figure 3.33 respectively.

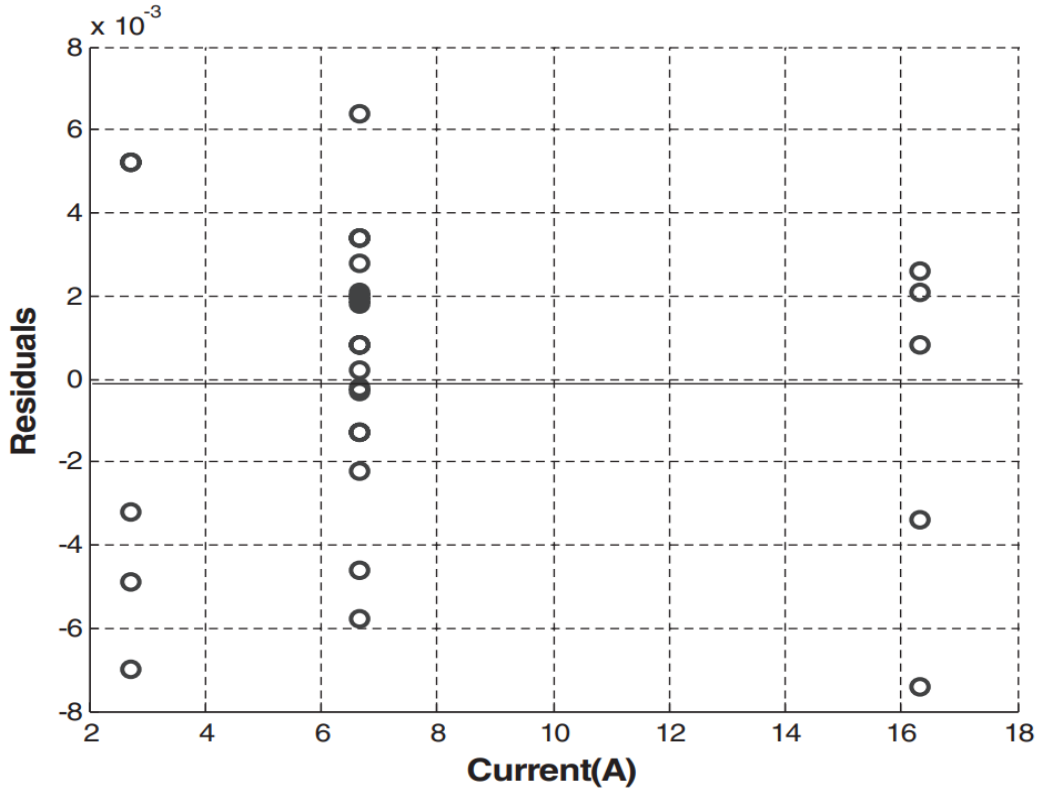

Figure 3.32: Scatter plot of current versus residuals

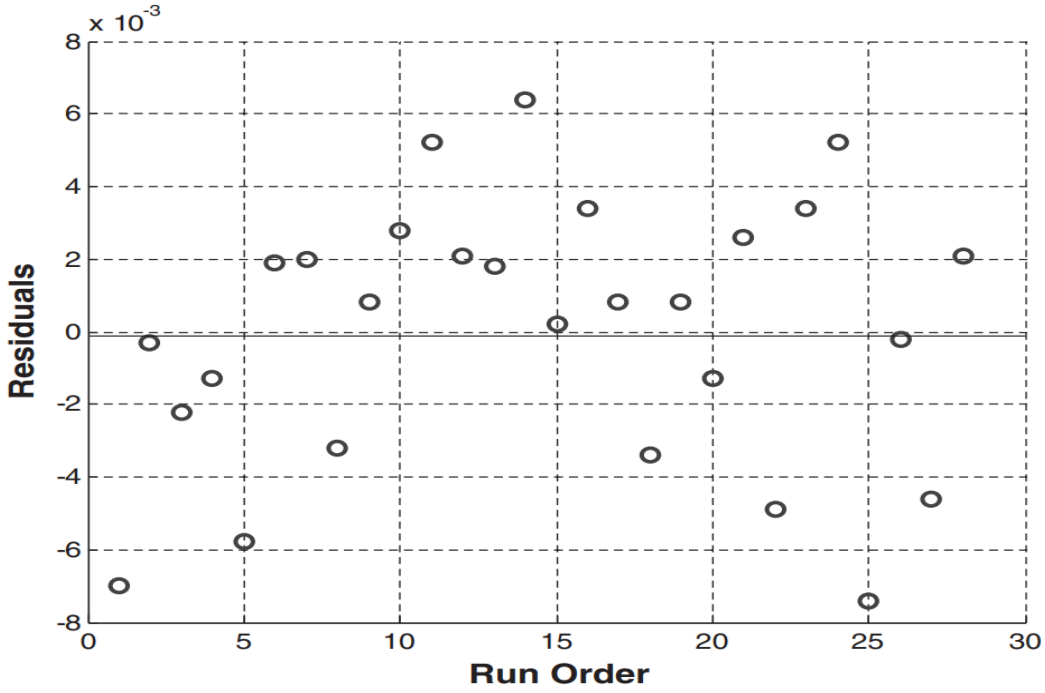

Figure 3.33: Scatterplot of run order versus residuals

In these figures, the spread of the residuals appears consistently uniform across the different levels of the predictor variables, which are temperature and current. Randomly scattered

points are observed both above and below the y = 0 line. This indicates that the standard deviation of the random error remains consistent for the responses observed at each temperature and current. The scatter plots strongly suggest that the parametric model is likely a good fit for the experimental data.

4 Control algorithm for operation of the system

Energy management system (EMS) refers to a comprehensive approach or framework designed to monitor, control, and optimize energy usage within a given system or organization. This includes various processes such as energy data collection, analysis, and decision-making to achieve energy efficiency, cost savings, and environmental sustainability goals (international organization for standardization) [49]. Following this definition, this section will focus on organizing an EMS system, whereby data monitoring and collection lead to day-ahead planning. Through this planning process, energy management, control, and distribution are implemented.

4.1 Decision making process: day-ahead plan

All the data containing day-ahead market prices have been provided by Nordpool group [50], which is published daily around 1 p.m., along with previously collected consumption data (P_{L_his}) of the building, undergo processing within the EMS system to make decisions for the next 24 hours. To predict the building load, a specific approach has been employed. Two coefficients are assigned: one to each hour of the current day and the other to each hour of the hourly average of the past week. By comparing these coefficients, ranging from zero to one for both parameters (the current day and its last week), the optimal values were determined to be thirty percent for the current day and seventy percent for the last week. This approach resulted in an approximate twenty percent error in the real load of the building. These findings are detailed in chapter "sensitivity analyses" since for the prediction of the consumption, the real load of the current day is needed, the day-ahead program is planned in the last hour of the day. Afterwards, this plan verifies whether the electrolyzer-fuel cell system can function together, ensuring that the benefits of the fuel cell are reasonable when compared to the cost of hydrogen production by the electrolyzer for that specific day ($C_{tot2} \geq 1.3*C_{tot1}$). Additionally, it assesses the conditions under which just hydrogen can be produced. This comparison involves analyzing the average unit prices of the five cheapest hours for the upcoming day ($C_{avg,5h}$) against the average unit prices of the past seven days during the five cheapest hours ($C_{avg,5h\_7day}$), while considering the fuel status (X). Furthermore, the system considers scenarios where the fuel cell operates solely for hydrogen consumption. In such cases, it determines whether the electrolyzer remains inactive for the day. Then, by comparing the average unit prices of the six highest hours for the upcoming day ($C_{avg,6h}$) with the average unit prices of the six expensive hours over the past seven days ($C_{avg,6h\_7day}$), also considering the fuel status to decide if the fuel cell should operate or remain inactive. The relations are mentioned from equations (4.1) to (4.7) as the following:

$$P_L+P_{ELZ} = P_{FC}+P_G \quad (4.1)$$

P_L: Hourly load power [kW]

P_{ELZ}: Power taken by electrolyzer [kW]

P_{FC}: Power from fuel cell [kW]

P_G: Power taken from the grid [kW]

$C_{tot1} = \sum_{t=0}^{T-1} P_{ELZ}(t) * C_{BP}(t) * \Delta t$ (4.2)

C_{tot1}: Total cost of hydrogen production by the electrolyzer [NOK]

C_{BP}: Unit buying price of electricity from grid [NOK/kWh]

$\Delta t: Duration\ [hr]$

t=0,…,T-1

$C_{tot2} = \sum_{t=0}^{T-1} P_{FC}(t) * C_{BP}(t) * \Delta t$ (4.3)

Ctot2: Total contribution of the fuel cell [NOK]

$C_{avg,6h} = \sum_{t=0}^{T-1} C_{BP}(t)/6$ (4.4)

$C_{avg,6h}$: Average of the 6-highest unit price [NOK/kWh]

$C_{avg,5h} = \sum_{t=0}^{T-1} C_{BP}(t)/5$ (4.5)

$C_{avg,5h}$: Average of the 5-cheapest unit price [NOK/kWh]

$C_{avg,6h\_7day} = \text{Avg}\ [\sum_{t=0}^{T-1} C_{BP}(t)/6](i)$ (4.6)

$C_{avg,6h\_7day}$: Average of 6-highest unit price of the past 7days [NOK/kWh]

$C_{avg,5h\_7day} = \text{Avg}\ [\sum_{t=0}^{T-1} C_{BP}(t)/5\ ](i)$ (4.7)

$C_{avg,5h\_7day}$: Average of 5-lowest unit price of the past 7days [NOK/kWh]

4.2 Sensitivity analyses

4.2.1 Sensitivity analysis for load prediction:

As discussed earlier in the previous section, load prediction relies on assigning two coefficients (α and β) to determine weights on historical load data (P_{L_his}). One coefficient corresponds to the average load for each hour over the past seven days, while the other relates to each hour on the previous day of a given for which the day-ahead plan is organized. After conducting several sensitivity analyses, the optimal values for the coefficients, α and β, are determined to be 0.7 and 0.3, respectively. As evident in Table 4-1, different combinations of the coefficients yield different results.

This analysis was conducted for a week in April from the 10_{th} to the 16_{th}. Two parameters were used to measure deviations from the actual load: $\varepsilon_{avg\text{-}day}$, which represents the average deviation of predicted load for all hours of the given day as a percentage of the real load, and $\varepsilon_{avg\text{-}week}$, which denotes the weekly average error compared to the actual consumption data

(P_L). By comparing different values for both coefficients, it is observed that increasing α and decreasing β leads to reduced average daily and weekly errors up to a certain point (α=0.7, β=0.3), after which the errors begin to increase again. Specifically, $\varepsilon_{avg\text{-}day}$ decreased for each day, and $\varepsilon_{avg\text{-}week}$ showed about 18% deviation. This trend was consistent for the other two weeks in January and April, except for August, where the error decreased linearly up to (α=0.9, β=0.1). However, the reduction in error in August was negligibly small (<0.5%).

Finally, after conducting the analysis using the coefficients values as depicted in Table 4-1, the average prediction errors over an entire week in January, August, and October are as follows: 16.6%, 30%, and 16%, respectively.

Table 4-1 Daily and weekly average error based on different combinations of coefficients

Coefficient [-]		$\varepsilon_{avg\text{-}day}$ [%]							$\varepsilon_{avg\text{-}week}$ [%]
α	β	10 Apr	11 Apr	12 Apr	13 Apr	14 Apr	15 Apr	16 Apr	
0	1	25.7	15.6	16.6	23.2	38.4	20	26.7	23.7
0.1	0.9	23.6	14.2	16.6	22.8	36.4	18.5	25.9	22.6
0.2	0.8	22.2	13.1	16.7	22.4	34.6	17	25.3	21.6
0.3	0.7	20.8	11.9	16.7	22.2	32.9	15.6	24.7	20.7
0.4	0.6	19.7	11	16.8	22.2	31.1	14.2	24.2	19.9
0.5	0.5	18.6	10.2	16.9	22.4	29.8	13	23.6	19.2
0.6	0.4	17.7	9	17	22.6	28.6	11.9	23.1	18.7
0.7	0.3	17.4	9	17.3	22.8	27.8	11.2	23	18.4
0.8	0.2	17.5	10	17.8	23.4	27.6	11.3	22.8	18.6
0.9	0.1	18.5	10.7	18.3	24.3	28	11.7	22.6	19.2
1	0	19.8	11.4	18.9	25.1	29	12.2	22.5	19.8

Table 4-2: Average error during a week in January, April, August, and October

α	β	$\varepsilon_{avg\text{-}week}$ [%] Jan	$\varepsilon_{avg\text{-}week}$ [%] Apr	$\varepsilon_{avg\text{-}week}$ [%] Aug	$\varepsilon_{avg\text{-}week}$ [%] Oct
0.7	0.3	16.6	18.4	30	16

4.2.2 Sensitivity analysis on the working duration:

One of the most critical factors determining the economic feasibility of the system is the operational duration of the electrolyzer and fuel cell. The installation of such a system is based on the favorable potential in electricity unit prices during specific periods. Given that these price differentials occur within narrow peak and off-peak periods, it becomes essential to define a specific timeframe for the operation of the electrolyzer and fuel cell. Moreover, as the power of the electrolyzer is fixed at 12 kW, but the power of the fuel cell is less than

that of the electrolyzer and can vary based on the building load, the run time duration for both devices is not equal. Various aspects and considerations led to setting a maximum of 5 hours for the electrolyzer and 6 hours for the fuel cell.

The economic feasibility of the system operation hinges on three primary parameters, which form the basis of sensitivity analyses. Firstly, there is HUB/NOR [-], representing the ratio between hydrogen utilization benefit and normal cost. This ratio illustrates the portion of normal cost covered by utilizing the Hydrogen-based energy system, regardless of the remaining hydrogen in the tank by the end of each week. The second factor is THUB/NOR [-], which mirrors the parameter. However, it accounts also for the value of the remaining hydrogen at the end of a week. Lastly, there is THUB itself, denoting the total hydrogen utilization benefit in [NOK].

In the following tables, three economic parameters and the relative equations from (4.8) to (4.11), can be defined as:

$NOR=C_{BP}(t)*P(t)$	(4.8)	NOR: Normal cost of electricity in absence of both electrolyzer and fuel cell [NOK]. (summation of all daily NOR over a week)
$HUB=FC_{contribution} - ELZ_{cost}$ $FC_{contribution}= P_{FC}*t*C_{BP}(t)$ $ELZ_{cost}= P_{ELZ}*t* C_{BP}(t)$	(4.9)	HUB: Subtraction of fuel cell contribution from the cost of H_2 production by electrolyzer [NOK]. (summation of all daily HUB over a week)
$THUB=HUB+HSB$	(4.10)	THUB: sum of all daily HUB over a week and HSB of the last day of the week [NOK]
$HSB=m_{H2}*LHV_{H2}* \eta_{FC}*C_{avg6h\text{-}next}$	(4.11)	HSB: Hydrogen saving benefit [NOK] (calculated based on the value of the remaining H_2 in the tank) LHV: Lower heating value of hydrogen (0.03333) [kWh/g] m_{H2}: Remaining gas in the tank at the end of the day $C_{avg6h\text{-}next:}$ Average of the 6-highest unit price of electricity for the next operational day [NOK/kWh]

First and foremost, for the case study, which involves several containers where students reside, it is crucial to cover the building load for at least several hours in case of emergency conditions, say 5-6 hours. Considering the efficiency of the fuel cell (η_{FC}=0.6) and the average power consumption rate in the building, which is about 4 [kW], the running time of the fuel cell is at most 6 hours. The other important reason is that, based on several assessments involving the analysis of more than 50 days unit prices, collecting and studying relevant data of electricity unit prices, a comprehensive sensitivity analysis was conducted for all four weeks of four months in the year 2023. Two of these assessments for a week in January and October, are displayed in Table 4-3 and Table 4-4 respectively.

Table 4-3: Sensitivity analysis on different working hours-Weekly overview in January

System running hours [hr]		Economic evaluation			
ELZ	FC	HUB/NOR [%]	THUB/NOR [%]	THUB [NOK]	January ($10_{th}-16_{th}$)
4	5	10.6	10.6	58.4	
5	6	12.8	12.9	71.3	
6	7	3.7	7.3	40.6	
7	8	2.1	4.5	24.9	

Table 4-4: Sensitivity analysis on different working hours-Weekly overview in October

System running hours [hr]		Economic evaluation			
ELZ	FC	HUB/NOR [%]	THUB/NOR [%]	THUB [NOK]	October ($10_{th}-16_{th}$)
4	5	21.2	21.2	43.6	
5	6	17.6	17.6	36.1	
6	7	10.8	12	24.7	
7	8	13.9	15.7	32.2	

4.2.3 Sensitivity analysis on C_{tot2}/C_{tot1} ratio:

Another crucial factor for which a sensitivity analysis was conducted is the ratio between the benefit gained by the fuel cell (C_{tot2}) and the cost of the electrolyzer (C_{tot1}). This ratio holds significant importance as it serves as a key determinant in the final assessment of the system feasibility, alongside the fuel tank status. If the ratio falls below one, it indicates that running the system is not economically viable. However, if the ratio surpasses a certain threshold, both the electrolyzer and fuel cell can operate, considering the tank capacity. A comprehensive analysis of different values across all four weeks was conducted, from which the optimal ratio value was determined to be 1.3. Two weeks are provided as examples, shown in Table 4-5 and Table 4-6. This ratio represents the best value, yielding the highest values for HUB/NOR and THUB/NOR.

The highest and lowest values for HUB/NOR and THUB/NOR are 27.2% and 43.5%, respectively, occurring in August, and 6.6% and 6.8%, respectively, occurring in April. In August, there are even negative unit prices of electricity on two days. However, in April, the system was only operational for two days and remained inactive for the remaining days.

Table 4-5: Sensitivity analysis on different ratio of C_{tot2}/C_{tot1}- Weekly overview in January

Ctot2/Ctot1 [-]	HUB/NOR [%]	THUB/NOR [%]	THUB [NOK]	
0.4	0.69	6.6	33.33	January ($10_{th} - 16_{th}$)
1.1	12.8	12.9	71.5	
1.3	12.8	12.9	71.5	
1.5	3.6	9.9	54.7	
1.7	2	7.4	40.9	
12	1.6	7.9	43.6	

Table 4-6: Sensitivity analysis on different ratio of C_{tot2}/C_{tot1}- Weekly overview in October

Ctot2/Ctot1 [-]	HUB/NOR [%]	THUB/NOR [%]	THUB [NOK]	
0.4	9.9	12.2	25.1	October ($10_{th} - 16_{th}$)
1.1	17.6	17.6	36.2	
1.3	17.6	17.6	36.2	
1.5	17.6	17.6	36.2	
1.7	17.6	17.6	36.2	
12	17.5	21.8	44.7	

4.2.4 Sensitivity analysis on fuel tank status (X):

Finally, the last crucial factor impacting the system's operation is the status of the fuel tank. This factor holds significant influence, as illustrated by examples: If the tank capacity reaches a certain threshold, for instance, 90% full, then, the electrolyzer must not work even in scenarios of negative electricity unit prices, Conversely, when the fuel tank is nearly empty, and the difference between unit prices at peak and off-peak hours is negligible, the fuel cell must remain off.

In the following tables, Table 4-7 and Table 4-8, the impact of different thresholds on the economic parameters for Ctot2/Ctot1=1.3 is illustrated. In October, the advantageous effect of increasing the margin dictating the electrolyzer ON/OFF status is evident. The optimal tank capacity occurs when X approaches 80%. Similarly, favorable outcomes are observed for limits on X determining the fuel cell operational status or inactivity. However, this positive effect occurs when X decreases to a certain threshold (X<0.2), signifying that below 20% of the tank capacity, the fuel cell must not work. Consequently, the highest economic benefit is attained when the tank limits are set at 0.8 and 0.2 for the electrolyzer and fuel cell, respectively. The comprehensive description of the control algorithm, which governs the operation of the system, is provided in the "control algorithm scenario" section within this chapter.

Table 4-7: Sensitivity analysis on fuel tank-weekly overview in October

Fuel tank limits X [-]		Economic evaluation [-] $C_{tot2}/C_{tot1}=1.3$			
ELZ	FC	HUB/NOR [%]	THUB/NOR [%]	THUB [NOK]	
0.1	0.9	2.4	11.7	24.1	October (10_{th} – 16_{th})
0.2	0.8	2.4	11.7	24.1	
0.3	0.7	2.4	11.7	24.1	
0.4	0.6	11.5	11.5	23.6	
0.5	0.5	11.5	11.5	23.6	
0.6	0.4	11.5	11.5	23.6	
0.7	0.3	14.6	17.5	35.9	
0.8	0.2	17.6	17.6	36.2	
0.9	0.1	17.6	17.6	36.2	

Through the sensitivity analysis on tank limits, it was determined that the optimal outcome is achieved when, for the electrolyzer, X increases from 50% of the tank capacity towards full position, while for the fuel cell, the best result is obtained when X decreases from 50% down to empty position. Consequently, only values above 0.5 for the electrolyzer and below 0.5 for the fuel cell were considered for the remaining two months. Additionally, various options for tank limits were examined, some of which are detailed in Table 4-9. As evident from the table below, the results in January are largely consistent across all combinations with minor variations. However, in October, there is a noticeable difference in results. The only margins that exhibit a negative impact on economic parameters are when the fuel tank margin for the electrolyzer is set to zero and for the fuel cell is considered at full capacity, resulting in a significant reduction in benefits. On the other hand, altering the ratio of Ctot2/Ctot1 yields disparate outcomes. Another crucial rationale behind selecting these limits is related to practical considerations. With 20% of the tank capacity amounting to approximately 400 [g], this equates to less than 2 hours of operation for the electrolyzer, and roughly the same duration for the fuel cell. Consequently, it is impractical for the system to operate for less than 2 hours, hence justifying the chosen limits.

Table 4-8: Sensitivity analysis on fuel tank-weekly overview in January

Fuel tank limits X [-]		Economic evaluation [-] $C_{tot2}/C_{tot1}=1.3$			
ELZ	FC	HUB/NOR [%]	THUB/NOR [%]	THUB [NOK]	
0.1	0.9	1.8	3.2	17.7	January (10_{th} – 16_{th})
0.2	0.8	3.3	6	32.8	
0.3	0.7	4.2	8.7	48.3	
0.4	0.6	4.2	8.7	48.3	
0.5	0.5	12.8	12.9	71.5	
0.6	0.4	12.8	12.9	71.5	
0.7	0.3	12.8	12.9	71.5	
0.8	0.2	12.8	12.9	71.5	
0.9	0.1	12.8	12.9	71.5	

Table 4-9: Sensitivity analysis on fuel tank with different combinations on X

Fuel tank limits X [-]		Economic evaluation C_{tot2}/C_{tot1}=1.3					
		January			October		
ELZ	FC	HUB/NOR [%]	THUB/NOR [%]	THUB [NOK]	HUB/NOR [%]	THUB/NOR [%]	THUB [NOK]
0.6	0.3	12.8	12.9	71.5	11.5	11.5	23.6
0.6	0.1	12.8	12.9	71.5	11.5	11.5	23.6
0.7	0.4	12.8	12.9	71.5	14.6	17.5	35.9
0.7	0.1	12.8	12.9	71.5	14.6	17.5	35.9
0.8	0.4	12.8	12.9	71.5	14.6	17.5	35.9
0.8	0.3	12.8	12.9	71.5	14.6	17.5	35.9
0.9	0	12.8	12.9	71.5	17.6	17.6	36.2
1	0	12.8	12.9	71.5	17.6	17.6	36.2
0	1	-2.9	4.1	22.5	5.5	6.1	12.6

4.3 Constraints

Within the energy management system, several constraints must be considered. Firstly, the overall load of the building must be satisfied, whether by the grid alone or in conjunction with the electrolyzer-fuel cell system ($P_L+P_{ELZ}=P_{FC}+P_G$). Secondly, there are constraints related to overall costs and profit considerations. Specifically, the contribution of the fuel cell must always be equal to or greater than 1.3 times the cost of hydrogen production to ensure whether the system can work together on that specific day ($C_{tot2} \geq 1.3*C_{tot1}$). Furthermore, to assess the feasibility of operating either the electrolyzer or fuel cell, additional conditions must be met. Specifically, the average unit prices of the six most expensive hours must exceed their respective averages over the past seven days ($C_{avg,6h} > C_{avg,6h\_7day}$). Conversely, from the electrolyzer perspective, the average unit prices of the five cheapest hours must be lower than their respective averages over the past seven days ($C_{avg,5h} < C_{avg,5h\_7day}$). These comparisons help determine the economic viability of operating either of component, of the system based on prevailing market conditions. Another constraint involves the fuel tank status. The fuel tank has a capacity of 2 kg and can be discharged until it is empty. However, from a filling or charging perspective, it must not be filled beyond 98% of its capacity, due to the safety (X<=0.98). These constraints play a crucial role in optimizing the operation of the energy management system and ensuring efficient utilization of resources.

1- $P_L+P_{ELZ}=P_{FC}+P_G$

2- $0=< X<=0.98$

3- $C_{tot1}*1.3 <= C_{tot2}$

4- $C_{avg,6h} > C_{avg,6h-7day}$

5- $C_{avg,5h} < C_{avg,5h-7day}$

X: Hydrogen tank status [-], X= 2 kg

4.4 Objective function

A key part of an Energy Management System (EMS) is its objective function. This function sets out the main goals and standards for optimizing the system. The EMS is made to oversee and control how energy is used in a building. The objective function is important in making decisions for the EMS because it guides how to make the most effective use of the energy resources available.
The main objective functions are listed below:

- Maximizing overall cost savings (ΔC_{save}): It is the main goal, which is achieved by subtracting the contribution of the fuel cell (C_{tot2}) during peak electricity hours (when the load is satisfied and unit prices are high, ($C_{avg,6h}$), Additionally, it involves minimizing the total cost of hydrogen production by the electrolyzer system (C_{tot1}) during off-peak hours (when unit prices are lowest, $C_{avg,5h}$), hence, reducing the final electricity cost. This objective is achieved through the following equation (Eq.4.12):

$$\text{Max } \{\Delta C_{save} = C_{tot2} - C_{tot1}\} \quad (4.12)$$

- Reliability: In certain situations, an EMS may prioritize maximizing the reliability of the energy supply. This means ensuring that the system can meet the energy demand for extended periods during emergencies or power outages. Another objective is to store hydrogen for emergency situations.

- Load shifting: Load shifting refers to the practice of re-scheduling electricity consumption to alternative time intervals while keeping the overall consumption unchanged. This strategy aims to optimize energy usage by capitalizing on variations in electricity costs or grid demand, effectively managing energy resources without altering the total amount consume, which can contribute to grid power balance by helping to match electricity supply with demand more efficiently.

Decision variables:

- Electrolyzer: Binary variable indicating whether the electrolyzer operates during off-peak hours.
  ELZ = {0,1}; where:
  0: Electrolyzer does not operate during off-peak hours.
  1: Electrolyzer operates during off-peak hours.

- Fuel Cell: Binary variable indicating whether the fuel cell operates during peak hours.
  FC= {0,1}; where:
  0: Fuel cell does not operate during peak hours
  1: Fuel cell operates during peak hours

- Fuel tank capacity (X)

- C_{tot2}, C_{tot1}, $C_{avg,6h}$, $C_{avg,5h}$, $C_{avg,6h\text{-}7day}$, $C_{avg,5h\text{-}7day}$

4.5 Control algorithm scenario

The control algorithm scenario begins with the initial transmission of all the data containing day-ahead market prices shown in Figure 4.1 and Figure 4.2, and the historical load consumption data to the " day-ahead plan " section. This data undergoes processing to inform decision-making for the subsequent day, wherein predictive values for load consumption (P_L) are ascertained. The primary constraint in the subsequent phase revolves around ensuring the satisfaction of load requirements, a condition that necessitates the contribution of the available sources such as an integrated H_2 system (electrolyzer-fuel cell) and the grid. At first, two key parameters are considered: the total cost of electricity drawn from the grid, utilized for hydrogen production during off-peak hours (C_{tot1}) and the total contribution of the fuel cell during peak hours (C_{tot2}) over which the load is covered by the fuel cell totally not the grid.

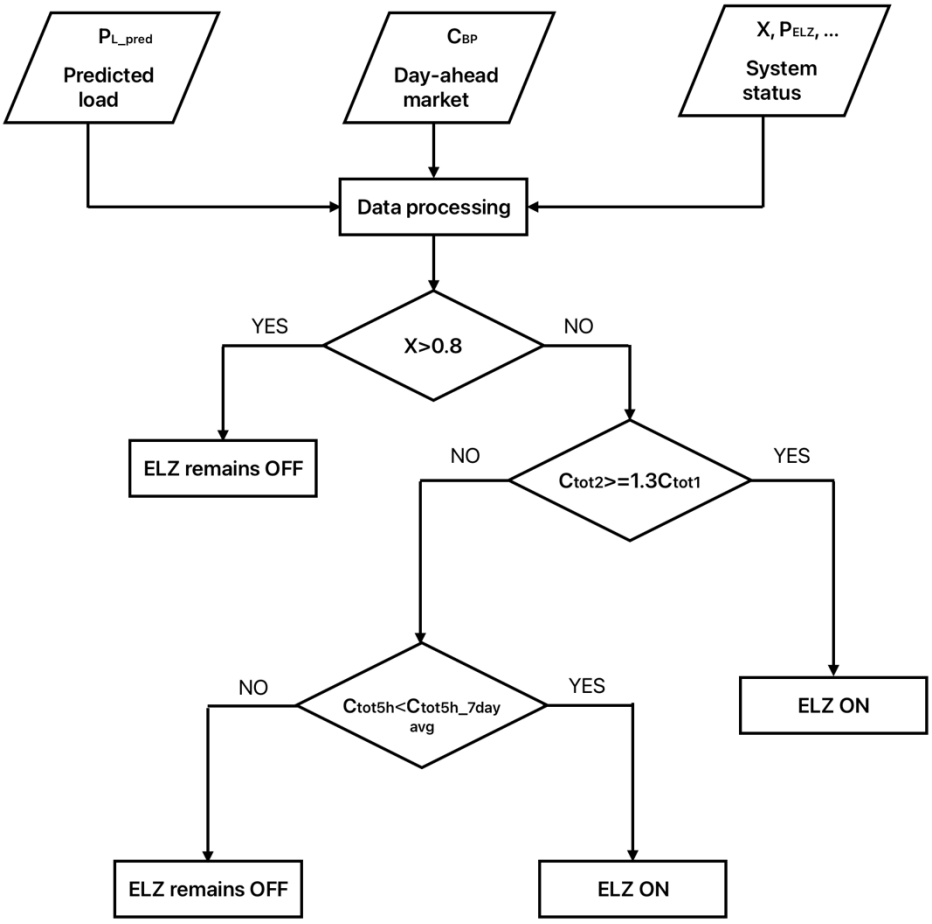

Figure 4.1: Decision making algorithm for the electrolyzer

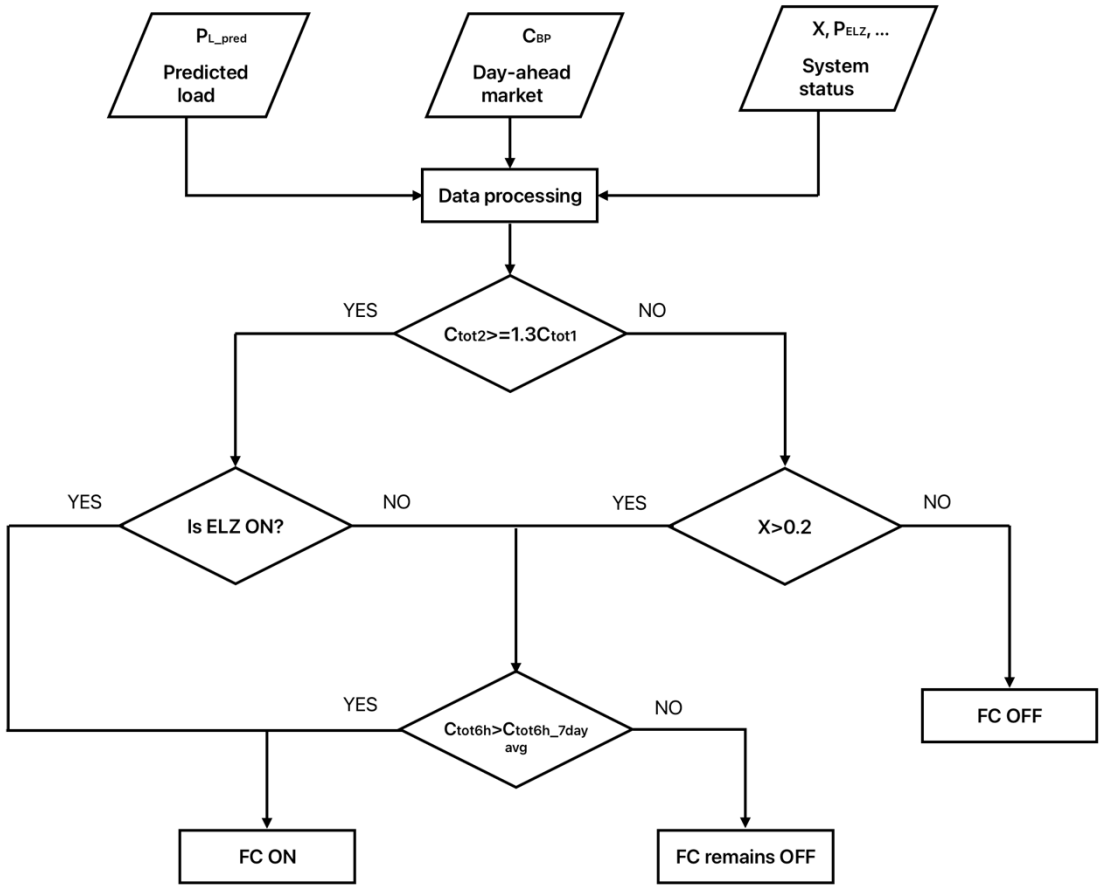

Figure 4.2: Decision making algorithm for the fuel cell

4.6 Different conditions of the system:

Based on the decision making of the system for electrolyzer and fuel cell, different conditions can happen for the system, these conditions are divided into four general groups that are explained in detail as the following:

4.6.1 Electrolyzer - Fuel cell both ON:

Following the evaluation of the total cost and contribution of the entire system, if the condition ($C_{tot2} \geq 1.3*C_{tot1}$) is satisfied, the fuel tank status is examined to ascertain if there is sufficient space available for hydrogen production (if X<0.8). If this condition holds true, the electrolyzer and fuel cell systems are activated, respectively. In this scenario, if the tank is empty (X=0), the electrolyzer operates for 5 hours. At its nominal power ($P_{nom,ELZ}$=12 kW), it can produce approximately 1260 grams of hydrogen. Alternatively, if there is existing hydrogen in the tank from previous production, the tank status is considered. If the sum of the previously produced hydrogen and the 5-hour production exceeds 98% of the tank capacity (X <= 0.98, which is 1960 g), then it operates until the fuel tank reaches its

defined limit. Otherwise, it operates again for 5 hours. In essence, the electrolyzer operates for a maximum of 5 hours.

4.6.2 Electrolyzer - Fuel cell both OFF:

Conversely, if a space constraint exists (if X>0.8), the electrolyzer remains off regardless of the total cost difference. From the fuel cell perspective, a final consideration is made by comparing the day-ahead average of the 6-highest unit prices ($C_{avg,6h}$) with the average of 6-highest unit prices of the past 7 days ($C_{avg,6h\_7day}$). If the condition ($C_{avg,6h} > C_{avg,6h\_7day}$) is met, then the fuel cell will be run; otherwise, it remains off. This indicates that the unit prices are not reasonable enough for producing or consuming hydrogen compared to their past 7 days' average prices.

4.6.3 Electrolyzer ON - Fuel cell OFF:

On the contrary, if ($C_{tot2} \geq 1.3*C_{tot1}$) is not satisfied, indicating that the price difference for that day is not substantial enough, one of the electrolyzer or fuel cell must remain inactive. From the electrolyzer perspective, after evaluating the fuel tank status, the condition compares the day-ahead average of the 5-cheapest unit prices ($C_{avg,5h}$) with the average of 5-lowest unit prices of the past 7 days ($C_{avg,5h\_7day}$). If ($C_{avg,5h} < C_{avg,5h\_7day}$) is met, then the electrolyzer operates within its defined working hours based on the fuel tank status. In this scenario, the fuel cell remains inactive, regardless of $C_{avg,6h}$, as one of the priorities is to store energy (hydrogen production) for emergency conditions.

4.6.4 Electrolyzer OFF - Fuel cell ON:

Another condition to consider is that the electrolyzer must remain inactive while the fuel cell operates according to its designated working hours plan. In this scenario, since the conditions ($C_{tot2} \geq 1.3*C_{tot1}$) and ($C_{avg,5h} < C_{avg,5h\_7day}$) are not met, the electrolyzer must stay off. However, the fuel cell might still operate under specific circumstances. If there is enough hydrogen in the tank (if X>0.2), there is a chance for it to work, subject to a specific condition. This condition is assessed through the comparison between ($C_{avg,6h}$) and ($C_{avg,6h\_7day}$). If ($C_{avg,6h} > C_{avg,6h\_7day}$) holds true, the fuel cell must consume the hydrogen in the tank for up to its maximum working hours, which is 6 hours. This assessment determines whether it is economically justified to consume the stored hydrogen, considering the profit potential based on ($C_{avg,5h\_7day}$). However, since the consumption rates of the fuel cell are not fixed and depend on load requirements, the fuel cell working time might vary. In any case, it operates within its planned hours and limited duration (6 hours) according to the fuel status. This approach ensures a comprehensive evaluation of the economic viability and operational requirements, contributing to an optimized utilization of the hydrogen production system within the broader energy framework.

With the assistance of the developed physics-based model and the implemented decision-making algorithm, the analysis for various periods of the year can now be initiated. This analytical exploration aims to evaluate the effectiveness and feasibility of the system. The comprehensive discussion and interpretation of these results will be undertaken in the upcoming chapter, results and discussion.

5 Results and discussion

The surging global energy demand, notably in heating, emphasizes the pivotal link between energy use and environmental sustainability. Heating, comprising 50% of global energy consumption, with 46% dedicated to space heating and domestic hot water, is a focal point, especially in regions like Norway with a heating-dominated climate [4]. Focused on this nexus, this research embarks on a pivotal exploration, driven by the central question: "How might the strategic utilization of off-peak electricity for hydrogen production and storage in building power consumption patterns result in cost reduction and increased sustainability?" The research posits a novel approach to enhancing the energy efficiency of buildings by integrating advanced technology, particularly the utilization of hydrogen as an energy storage solution. By delving into the unique energy landscape of Norway, where 98% of electricity production is derived from renewable sources, predominantly hydropower, this study aligns seamlessly with the nation's commitment to sustainable practices.

The University of Stavanger provides a living lab as the case study for a detailed analysis of load, consumption data, and electricity prices. Through this examination, the research explores the feasibility and benefits of introducing hydrogen solutions into building structures, aiming to enhance sustainability in the energy landscape. This chapter unfolds the outcomes of a comprehensive examination. Initially, it outlines the procedural details of applying the model and conducting calculations for a single day. Building upon this daily analysis, the investigation extends to encompass an entire week, presenting the weekly results. Further, the study delves into an analysis of results across two different weeks, each representative of a distinct season throughout the year. This structured approach aims to provide a nuanced understanding of the proposed strategy's efficacy in terms of sustainability and cost-effectiveness across varying temporal contexts. By evaluating the method's performance under diverse seasonal conditions, the chapter contributes valuable insights crucial for shaping the future trajectory of hydrogen-driven energy systems within buildings.

5.1 One day sample

To illustrate the functionality of the algorithm, along with the results obtained from the developed model and the subsequent cost calculations, a specific day (12_{th} October 2023) was selected for a detailed examination. All the analyzed data, encompassing the hourly load of the building from the case study and the daily unit price [50], pertains to the year 2023. This choice is attributed to the availability of the most up-to-date data for a thorough analysis. A crucial determinant in the algorithm decision-making process is the unit price of the day-ahead market, serving as a vital and readily available input. The hourly unit prices for the selected day are graphically depicted in the Figure *5.1*,in which At the time of writing this thesis, the exchange rate from Euro (EUR) to Norwegian Krone (NOK) was 11.63, offering essential context for the subsequent analysis. The entire strategy is formulated on the foundation of the daily price variation, moving from low to high. This approach proves highly effective, particularly during this specific timeframe throughout the year. It holds

particular significance for regions characterized by high volatility in electricity prices, with Norway being a prime example of such a potential option.

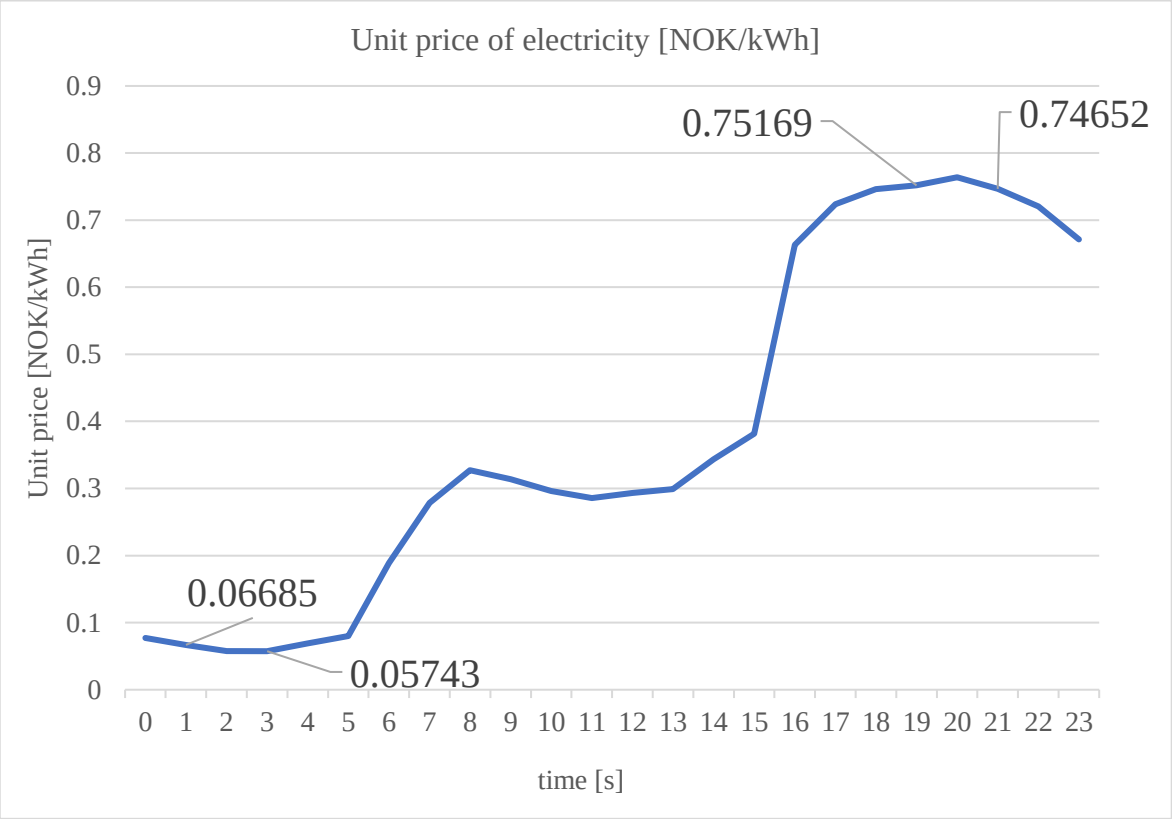

Figure 5.1: Hourly unit price of electricity for 12$_{th}$ October

An additional pivotal factor influencing decision-making is the load prediction for the day, achieved through a weighted average of the current day and the average load from the preceding week, as detailed in the methodology chapter. The graphical representation in the Figure *5.2*, depicts the actual load against the predicted load, allowing for a clear visual assessment of the disparities between the two.

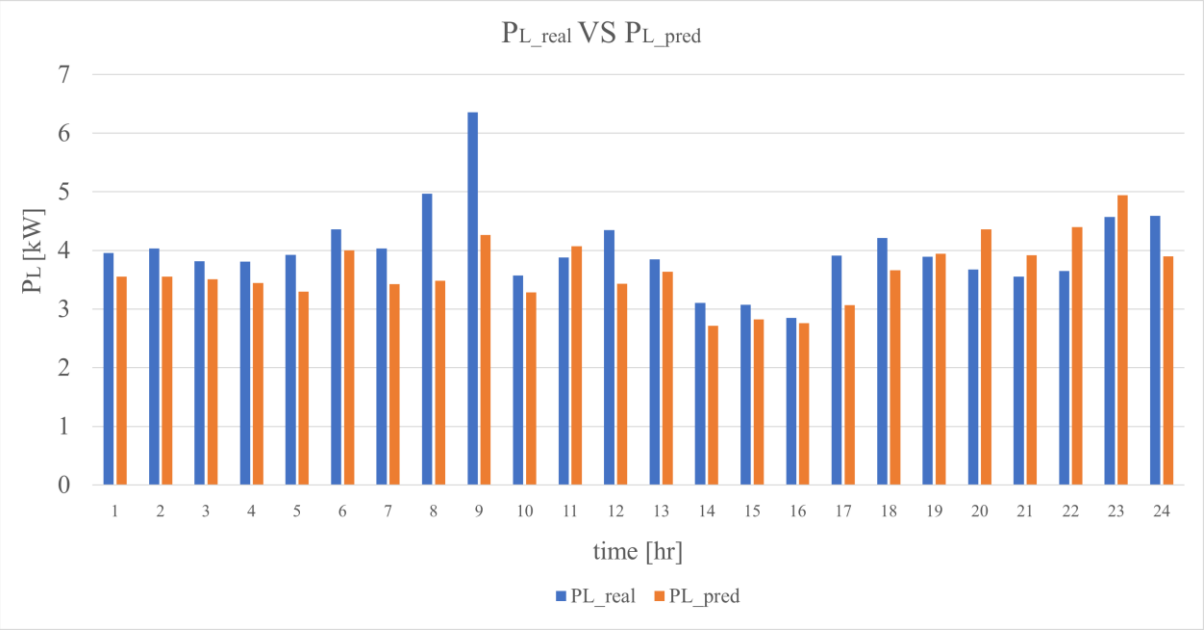

Figure 5.2:Real load of the building versus the predicted load - 12th October

With the crucial parameters of the unit price and the predicted load for the day at our disposal, the subsequent step involves commencing calculations to determine whether to activate the electrolyzer and fuel cell. These calculations are integral to the decision-making process, guiding the decision of whether these systems should be operational on the given day.

The initial step involves the calculation of C_{tot1}, obtained by multiplying the unit price, time and the power of the electrolyzer during 5 off-peak hours. Simultaneously, C_{tot2} is determined by multiplying the unit price, time, and the predicted load for the fuel cell during peak hours. The ratio between C_{tot2} and C_{tot1} is then computed, serving as a key determinant in the decision-making process. Additionally, the algorithm considers a parameter, X, representing the percentage of hydrogen remaining in the tank from the previous day(s). The resulting values are presented in Table *5-1*.

Table 5-1: Economic evaluation for 12th October with electrolyzer-fuel cell on/off status

Day	C_{tot1} [NOK]	C_{tot2} [NOK]	C_{tot2}/C_{tot1} [-]	X [%]	$C_{avg,6h}/C_{avg,6h\_7day}$ [-]	$C_{avg,5h}/C_{avg,5h\_7day}$ [-]	ELZ	FC
12 Oct	3.93	18.71	4.75	33	1.50	0.47	1	1

The observed ratio between C_{tot2} and C_{tot1}, exceeding 1.3, signifies substantial price variations throughout the day. Additionally, with 33% of the fuel tank occupied, it suggests there is sufficient capacity for hydrogen production. Accordingly, the algorithm mandates the simultaneous operation of both the electrolyzer and fuel cell. Consequently, hydrogen production occurs during 5 off-peak hours, while consumption aligns with the 6 costly hours of the same day. It is noteworthy that, in this case, the algorithm omits the assessment of

$C_{avg,6h}$ and $C_{avg,5h}$, as the ratio between C_{tot2} and C_{tot1} sufficiently guides its decision-making process. The order is now sent to the developed model and the results of the model are as following.

5.1.1 Power curves

After the decision-making process, the model is executed during the specified hours for both the electrolyzer and fuel cell. As clarified earlier, the electrolyzer operates at its nominal power, fixed at 12 [kW] and depicted in Figure *5.3*. It is crucial to leverage the cost-effective hours for rapid hydrogen production, hence the electrolyzer functions for five consecutive hours before ceasing operation for the remainder of the modeling period. Consequently, the power line descends to zero. The selection of the electrolyzer scale, tailored to residential size, is aligned with the building specific requirements.

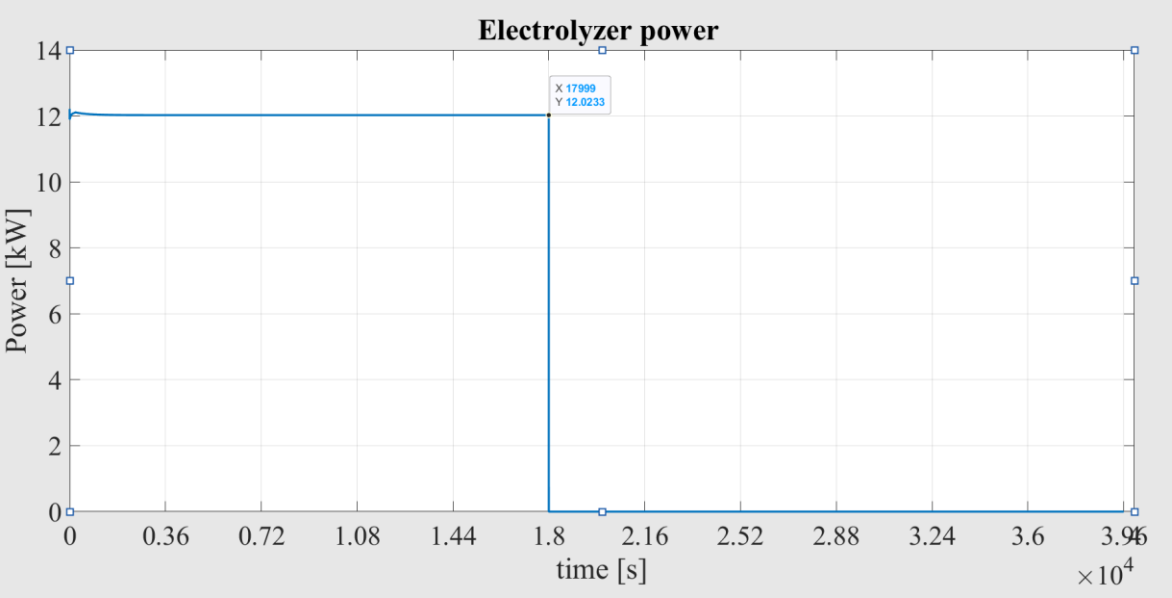

Figure 5.3 Electrolyzer power

Concerning the fuel cell, it remains inactive while the electrolyzer is operational, initiating its operation from the onset of the sixth hour of the modeling, concluding at 39,600 [s]. Despite the nominal power being 8 [kW], historical consumption data reveals that the fuel cell typically operates below its nominal power. Given its power being contingent on load requirements, it fluctuates hourly, as depicted in Figure *5.4*, demonstrating its non-fixed nature. For instance, on the selected day for discussion, the 6-hour load period, where approximately 1177 [g] is consumed, exhibits average loads of 4.2, 3.8, 3.6, 3.5, 3.6, and 4.5 [kW] during the hours from 17:00 to 23:00, respectively.

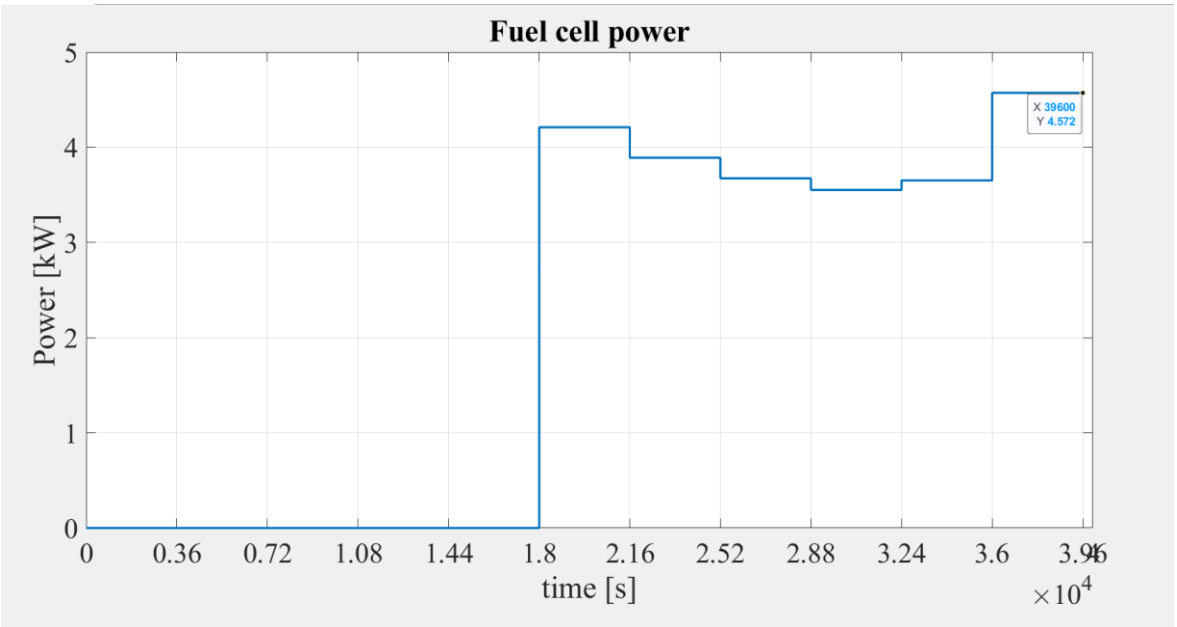

Figure 5.4 Fuel cell power

5.1.2 Hydrogen produced and consumed

As elaborated earlier, the fixed and nominal power of the electrolyzer with efficiency equal to 70% ensures a consistent rate of hydrogen production over 5 hours, resulting in the accumulation of approximately 1260 [g] of hydrogen from 12:00 a.m. to 5:00 a.m. (5 hours). This production profile is visually represented in Figure *5.5*, derived from the model, depicting the electrolyzer activity from the commencement of the modeling until it ceases hydrogen production at 18,000 s. Subsequently, the fuel cell initiates hydrogen consumption for the subsequent 6 hours of modeling. Given a relatively constant power requirement for meeting the building's demand, distinguishing changes in consumption rates during this phase, as illustrated in Figure *5.6*, is challenging. Ultimately, by the conclusion of the sixth hour of fuel cell operation and considering the fuel cell efficiency equal to 60%, approximately 1177 [g] of hydrogen is consumed from 17:00 to 23:00 which are the 6 consecutive most-expensive hours in terms of unit electricity price, satisfying the building's demand, yet leaving some residual hydrogen in the tank for subsequent days.

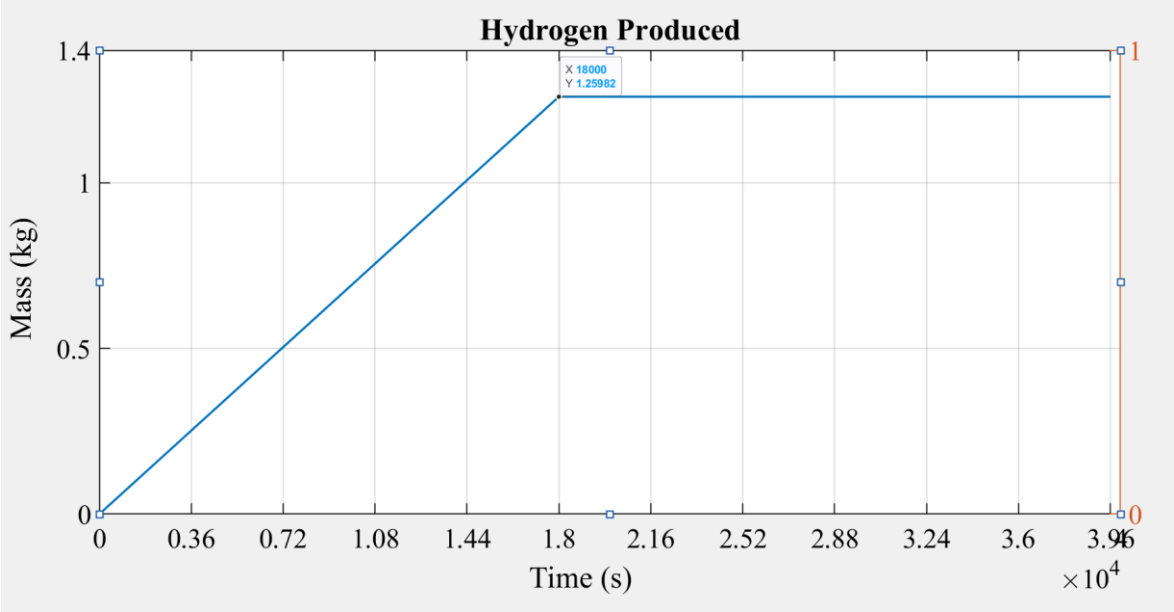

Figure 5.5: Hydrogen produced [kg]-Accumulated

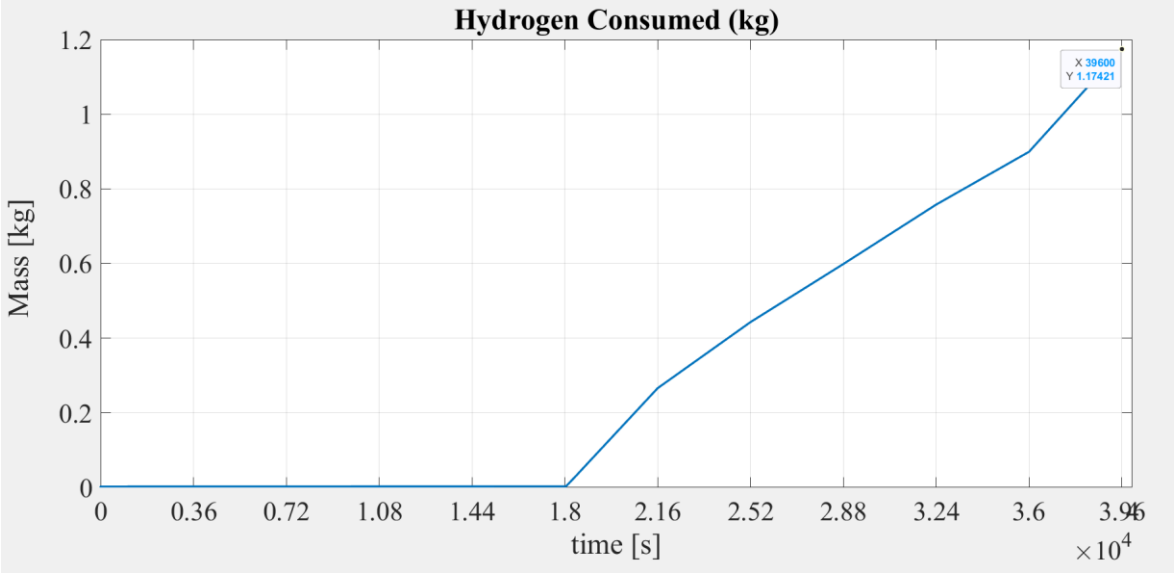

Figure 5.6: Hydrogen consumption [kg]-Accumulated

The amount of hydrogen produced and consumed follows the equations defined below. Corresponding hydrogen mass production and consumption, considering the power, efficiency, and time taken, can be observed in Table *5-2*.

$$\eta_{ELZ} = \frac{m_{H2-prod} * LHV}{\Sigma P_{ELZ}(t) * \Delta t} \quad [\%] \qquad (5.1)$$

$$m_{H2-prod} = \frac{\Sigma P_{ELZ}(t) * \Delta t * \eta_{ELZ}}{LHV} \quad [kg] \qquad (5.2)$$

$$\eta_{FC} = \frac{\Sigma P_{FC}(t) * \Delta t}{m_{H2-cons} * LHV} \quad [\%] \qquad (5.3)$$

$$m_{H2-cons} = \frac{\Sigma P_{FC}(t) * \Delta t}{\eta_{FC} * LHV} \quad [kg] \qquad (5.4)$$

Table 5-2: Hydrogen production/consumption calculation-12$_{th}$ October

Component	Parameter				
	Power [kW]	Δt [hr]	η [%]	LHV [kWh/g]	$m_{H2-prod/cons}$ [g]
ELZ	12	1	70	0.03333	1260.13
FC	4.2,3.8,3.6,3.5,3.6,4.5	1	60	0.03333	1177.67

5.1.3 Temperature curves

The temperature of the entire system and its management is one of the most important parameters that play a crucial role in the performance and efficiency of electrolyzers and fuel cells. Optimal temperature conditions are essential for maximizing their efficiency and prolonging their lifespan. In the electrolyzers, maintaining the correct temperature ensures that the electrochemical reactions proceed smoothly and efficiently. Higher temperatures can enhance reaction kinetics, leading to faster hydrogen production rates. However, excessively high temperatures can also increase energy consumption and accelerate material degradation, reducing the electrolyzer's lifespan. Similarly, in fuel cells, temperature management is crucial for achieving optimal electrochemical activity and preventing degradation. The operating temperature of a fuel cell affects its voltage output, reaction kinetics, and internal resistance. Maintaining the correct temperature enables efficient electrochemical reactions and ensures stable power output.

The Figure *5.7* and Figure *5.8*, demonstrate that the maximum temperature reached is 80°C, an optimal operating temperature for both PEM fuel cells and electrolyzers.

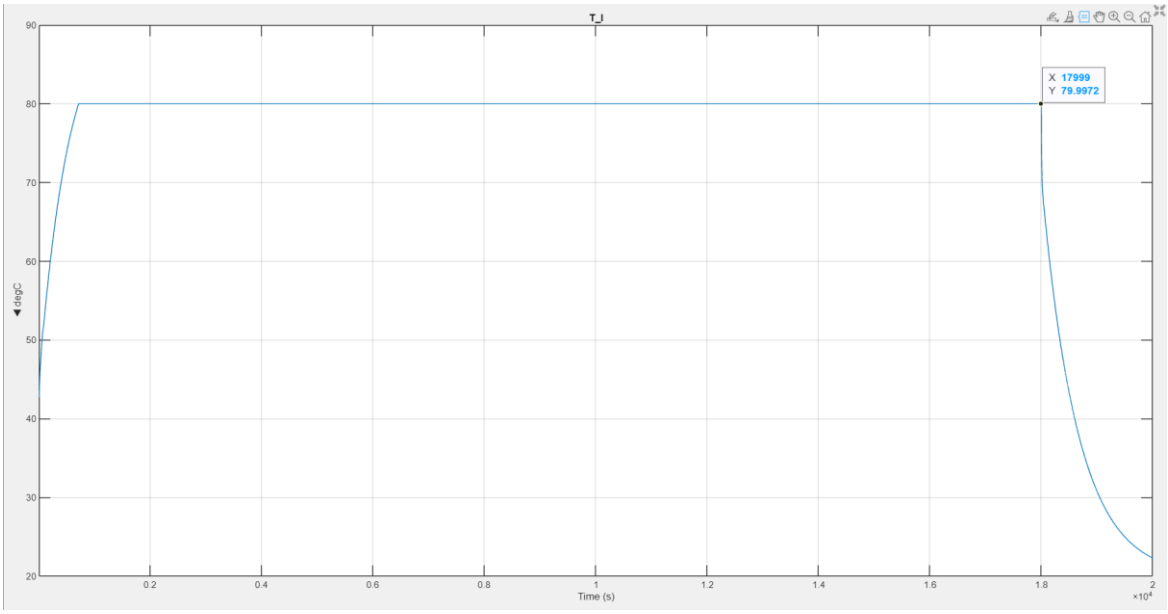

Figure 5.7: Eletrolyzer temperature

This favorable temperature range is maintained through the utilization of a heat exchanger in the electrolyzer and an efficient cooling system in the fuel cell. The emphasis on

temperature control is crucial, as it ensures the stability and optimal performance of these components, contributing to the overall reliability and efficiency of the integrated system.

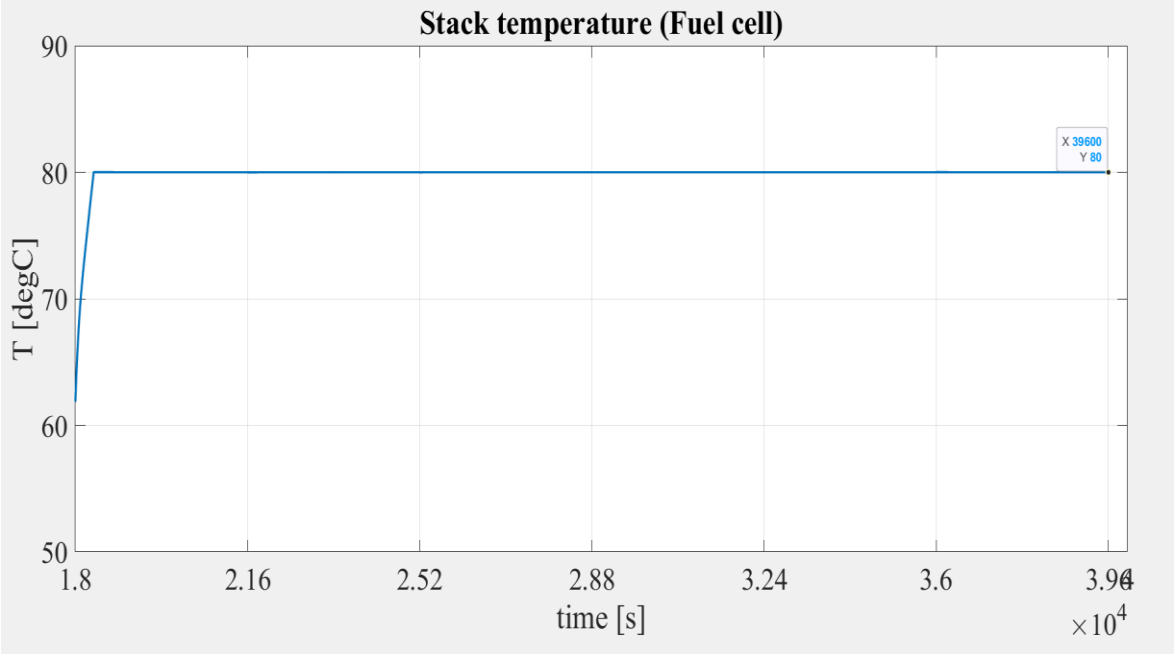

Figure 5.8: Fuel cell temperature

With the outcomes generated by the model, the subsequent step involves conducting final calculations to determine the cost associated with hydrogen production during the 5 low-cost hours and the profits derived from distributing this hydrogen across the 6 expensive hours of the day. This financial analysis aims to provide a comprehensive understanding of the economic dynamics associated with the proposed energy storage and distribution strategy, which are indeed only the operating costs.

5.1.4 Operational performance of the system on sample day-12th of October

Initiating the day-ahead plan, the operational hours for both the electrolyzer and fuel cell are predetermined, as outlined in *Table 5-3*. On this day, both systems operate at their maximum capacities: five hours for the electrolyzer and six hours for the fuel cell, as indicated in the first column of the table. The electrolyzer, is active from 12:00 a.m. to 5:00 a.m., producing 1260 [g] of hydrogen at a fixed production rate. The overall cost of hydrogen production by the electrolyzer is delineated in the "ELZ cost" column, accounting for the varying unit prices during the designated hours. Subsequently, the focus shifts to the working hours defined for the fuel cell. Operating at its maximum working hours for six hours, the fuel cell's consumption rate, contingent on the load, differs from that of the electrolyzer. This consumption results in utilizing 1177 [g] of hydrogen, meeting the entirety of the building's demand during the peak hours from 17:00 to 23:00 – the six most expensive hours of the day.

The "FC contribution" column reflects the financial contribution of the fuel cell, amounting to 17.44 [NOK]. Introducing the concept of Hydrogen utilization benefit (HUB), calculated

by subtracting the cost of production of hydrogen from the contribution of the fuel cell, provides a holistic view of the overall financial impact.

Table 5-3: Detailed calculations for the working hours of the system for 12$_{th}$ October 2023

Time [hr]	$H_{2, prod}$ [g]	$H_{2, cons}$ [g]	ELZ cost [NOK]	FC contribution [NOK]	HUB [NOK]	Normal cost [NOK]	Actual cost [NOK]
0	252.02	0	0.92	0	-0.92	0.30	1.23
1	252.02	0	0.80	0	-0.80	0.26	1.07
2	252.02	0	0.69	0	-0.69	0.21	0.91
3	252.02	0	0.68	0	-0.68	0.21	0.90
4	252.02	0	0.82	0	-0.82	0.27	1.09
5	0	0	0	0	0	0.34	0.34
6	0	0	0	0	0	0.76	0.76
7	0	0	0	0	0	1.38	1.38
8	0	0	0	0	0	2.07	2.07
9	0	0	0	0	0	1.12	1.12
10	0	0	0	0	0	1.14	1.14
11	0	0	0	0	0	1.24	1.24
12	0	0	0	0	0	1.12	1.12
13	0	0	0	0	0	0.92	0.92
14	0	0	0	0	0	1.05	1.05
15	0	0	0	0	0	1.08	1.08
16	0	0	0	0	0	2.59	2.59
17	0	210.57	0	3.04	3.04	3.04	0
18	0	194.51	0	2.90	2.90	2.90	0
19	0	183.71	0	2.76	2.76	2.76	0
20	0	177.61	0	2.71	2.71	2.71	0
21	0	182.61	0	2.72	2.72	2.72	0
22	0	228.62	0	3.29	3.29	3.29	0
23	0	0	0	0	0	3.08	3.08
SUM	1260.13	1177.67	3.93	17.44	13.50	36.69	23.19

The last two columns, "Normal cost" (36.69 [NOK]) and "Actual cost" (23.19 [NOK]) encapsulate the cost scenarios. In the "Actual cost" column, when the system operates, all associated costs and contributions are considered alongside normal costs. In contrast, if the system is inactive, the “Actual cost" aligns with the "Normal cost." This comprehensive analysis offers insights into the financial dynamics of hydrogen production and consumption on this specific day.

Building upon the established parameters, the economic viability and profitability of the system are evaluated through new metrics, as detailed in Table *5-4*.The "HUB/Normal cost [%]" parameter gauges the extent to which the costs typically incurred, known as normal costs, are covered when these systems are operational. The subsequent parameter, "total hydrogen utilization benefit (THUB [NOK])," provides a comprehensive evaluation by considering the costs, system contributions, and the value of the hydrogen left in the tank.

This value is calculated based on the average of the unit prices during the six most expensive hours of the next day.

Table 5-4: Final financial results-12$_{th}$ October 2023

Day	HUB [NOK]	HUB/NOR [%]	THUB [NOK]	THUB/NOR [%]
12 Oct	13.50	36.80	22.18	60.44

Figure *5.9*, contrasts the normal load of the building with the shifted load, illustrating the substantial impact of the system on load distribution during the assessed day.

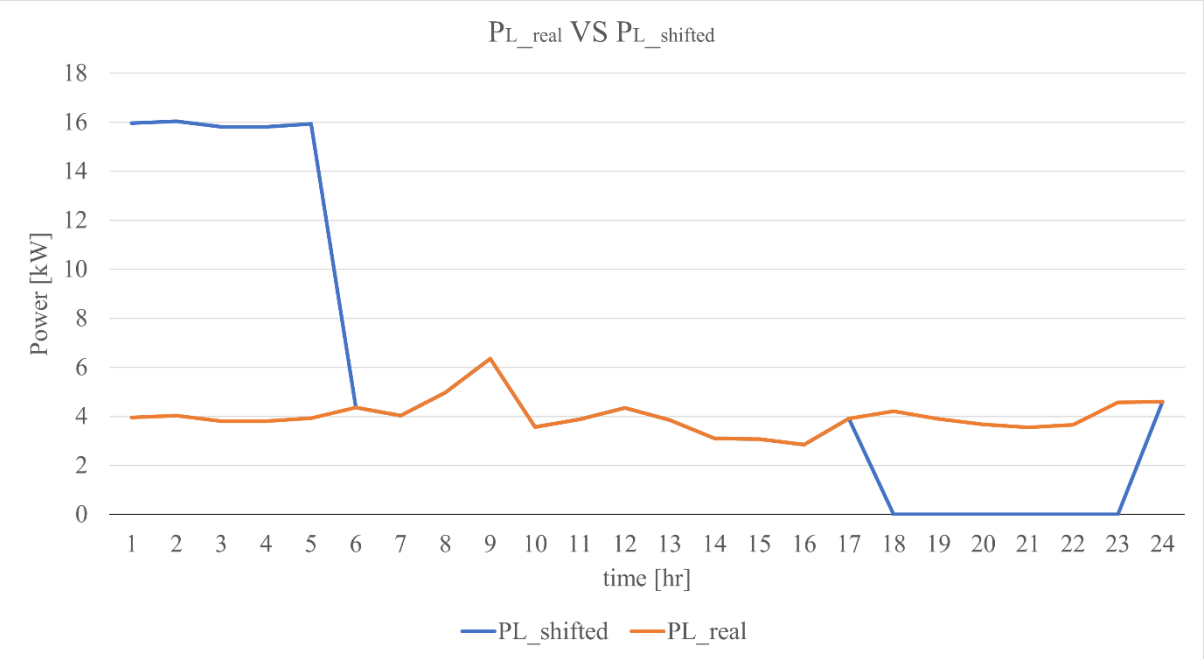

Figure 5.9: Real normal load versus the shifted load-12$_{th}$ October

Load shifting stands out as an essential objective not only within the scope of this survey but also from the broader perspective of grid management. It plays a pivotal role in achieving a more balanced grid. This intricate process involves analysis and processing of data provided from both the day-ahead market price and historical consumption load patterns. By scrutinizing this information, optimal operating windows are determined for both electrolyzer and fuel cell. Moreover, the decision-making process concerning the system's ON/OFF status hinges on factors such as the current fuel tank capacity and prevailing unit prices of electricity throughout the day. This approach ultimately leads to the effective execution of load shifting strategies, thereby enhancing grid stability and efficiency. In the visual representation, the blue line denotes the shifted load, while the orange line depicts the normal, real load. Notably, on this specific day, there is a noticeable absence of a significant peak during the costly electricity hours, which span from 17:00 to 23:00. Intriguingly, the entirety of the building's load within these six hours is fulfilled by the hydrogen produced

during the off-peak hours. Effectively, this results in a load shift from the right side to the left side of the curve, signifying a migration from demanding hours with high electricity prices to off-peak hours characterized by lower electricity costs.

5.2 Weekly calculations

The calculations discussed above were specifically conducted for a representative day, the 12th of October 2023. This comprehensive procedure is systematically replicated for the remaining days within the considered week in October. The compiled results are meticulously presented in Table *5-5*, offering a comprehensive overview of the system performance and decision-making across multiple days.

Table 5-5: Detailed financial and performance evaluation-Daily overview from 10_{th} to 16_{th} October

Day	X_i [%]	m_i [g]	C_{tot2}/C_{tot1} [-]	$C_{avg,6h}/C_{avg,6h\_7day}$ [-]	$C_{avg,5h}/C_{avg,5h\_7day}$ [-]	ELZ	FC	$P_{L,\ real\_6h}$ [kW]	$P_{L,pred\_6h}$ [kW]	$H_{2,prod}$ [g]	$H_{2,cons}$ [g]	m_f [g]	X_f [%]
10 Oct	0	0	2.65	1.79	0.79	1	0	21.82	20.78	1260.13	0	1260	63
11 Oct	63	1260	10.48	0.31	0.03	1	1	25.95	20.88	689.11	1297.88	660	33.01
12 Oct	33.01	660	4.75	1.5	0.47	1	1	23.55	25.23	1260.13	1177.67	742	37.14
13 Oct	37.14	742	1.69	1.11	0.71	1	1	22.12	22.47	1260.13	742	1261	63.07
14 Oct	63.07	1261	2.34	0.22	0.13	1	1	23.81	24.62	698.11	1190.77	768	38.44
15 Oct	38.44	768	11.77	0.77	0.09	1	1	30.9	25.21	1191.07	1545.3	414	20.73
16 Oct	20.73	414	0.58	1.33	3.94	0	1	26.79	23.76	0	414	0	0

According to Table *5-5*, the decision of system operation is made based on the initial fuel tank status (X_i) and other parameters (C_{tot2}/C_{tot1}, $C_{avg,6h}/C_{avg,6h\_7day}$, $C_{avg,5h}/C_{avg,5h\_7day}$), based on which different scenarios might happen, like, both electrolyzer and fuel cell must work, neither of them must work, or, one of the must be ON so the other must remain OFF. Subsequently, through the other columns, the real load for the fuel cell working hours (6 hours) and the predicted ones ($P_{L,pred\_6h}$) are shown, the reason of showing the real and predicted load for just 6 hours is that the electrolyzer must work with its defined and predicted load since it is independent of the real load power; however, for the fuel cell, the real load is essential, since regardless of the prediction, it must work based on the real demand of the building. This consideration leads to specific hydrogen production and consumption for each day. Finally, according to the accumulated hydrogen in the tank, there might be some hydrogen left, which is the final amount of the hydrogen left in the tank (X_f) that is delivered to the next day. Then based on
Table *5-6* the assessment is done according to the economic indices for each day, by which, the profitability of the system for each day can be analysed and seen.

Table 5-6: Final weekly results from 10_{th} to 16_{th} of October

Day	HUB [NOK]	HUB/NOR [%]	THUB [NOK]	THUB/NOR [%]
10 Oct	-5.98	-15.47	-2.20	-5.75
11 Oct	3.97	53.15	13.77	184
12 Oct	13.50	36.80	22.18	60.44
13 Oct	2.35	7.25	5.58	17.21
14 Oct	3.74	82.18	10.21	224
15 Oct	12.43	55.9	18.17	81.71
16 Oct	6.13	9.72	6.15	9.76

5.3 Monthly comparison of the results

Having completed the detailed calculations and assessments for the week spanning from the 10th to the 16th of October, the same meticulous process has been applied to another week in January, precisely from the 10th to the 16th. The results of these extensive analyses for a sample week in October, January, April, and August are systematically presented in *Table 5-7*. This comparative display provides a comprehensive insight into the system's performance and decision-making dynamics across these distinct months.

Table 5-7: Comparison of the results for the sample week in January, April, August and October

Period	HUB [NOK]	HUB/NOR [%]	THUB [NOK]	THUB/NOR [%]
10 -16 Jan	70.75	12.85	71.33	12.95
10 -16 Apr	43.79	6.6	44.94	6.86
10-16 Aug	43.09	27.24	66.83	42.26
10-16 Oct	36.15	17.62	36.15	17.62

After examining the data, it is evident that August stands out as the most successful month among the four with the final cost coverage of 27.24% and a total hydrogen utilization benefit that covers 42.26% of the normal cost. August exhibits a notable financial advantage compared to the situation if there was not any hydrogen-based system used. In contrast, April exhibits the weakest financial performance. This can be attributed to the system's operational duration of only two days within the week. The remaining days lack financial justification for system operation, resulting in a mere 6.6% coverage of the normal cost and a total utilization factor of 6.86%.

6 conclusion

In addressing the pressing global demand for energy, particularly in heating, this research has explored a pioneering strategy for hydrogen production and storage in building power consumption patterns. Focused on the specific case study of Norway, where heating constitutes a significant portion of energy consumption, the study aimed to assess the feasibility and sustainability of utilizing off-peak electricity for hydrogen production. The central question driving this investigation was, "How might the strategic utilization of off-peak electricity for hydrogen production and storage in building power consumption patterns result in cost reduction and increased sustainability?"

The research has demonstrated a novel approach to enhance the energy efficiency of buildings through the integration of advanced technology, specifically the use of hydrogen as an energy storage solution. The University of Stavanger provided a detailed case study for the analysis of load, consumption data, and electricity prices. The findings of this study are presented through a detailed examination of a sample day, followed by a systematic extension to an entire week, showcasing weekly results across different seasons.

The implemented algorithm, considering factors like unit prices, load predictions, and hydrogen storage status, guided the decisions for running the electrolyzer and fuel cell. It sent instructions to the physics-based model to create curves for power, temperature, hydrogen production, and consumption. Finally, the calculations for analyzing operational costs are conducted. The results, illustrated through graphical representations and tables, revealed a significant impact on load distribution. The hydrogen produced during off-peak hours effectively met the demand during peak hours, resulting in load shifting and cost optimization. In this study the energy production from the renewables is totally neglected and the aim was to evaluate the possibility of the strategy only with on-grid scenario.

The operational economic assessment, encompassing a monthly comparison, has revealed each month as a seasonal indicator of the system performance. August showcased the strongest performance for the summer season, with a final cost coverage of 27.24% and a total hydrogen utilization benefit of 42.26% over the normal cost, underscoring the financial efficacy of the hydrogen-based system. In stark contrast, April, representing the spring season, saw the lowest results with only 6.6% coverage of the normal cost and a total utilization factor of 6.86%, reflecting the system limited operation during this time. January and October, symbolizing winter and autumn, also recorded commendable performances with cost coverages of 12.85% and 17.62% respectively.

In conclusion, the findings of this research showcase the potential of the proposed strategy for hydrogen storage in buildings, particularly in regions with high electricity price daily variations. The successful implementation of this method, as evidenced by the case study in Norway, highlights its viability in contributing to cost reduction and increased sustainability in the energy landscape. The insights gained from this study contribute valuable knowledge to the field, paving the way for further advancements in smart energy solutions with the hydrogen energy systems.

Acronyms

IPCC	Intergovernmental Panel on Climate Change
EU	European Union
DHW	Domestic Hot Water
IEA	International Energy Agency
HVAC	Heating, Ventilation, and Air Conditioning
BMS	Building Management Systems
ICT	Information and Communications Technology
NZEB	Net-Zero Energy Building
ESS	Energy Storage System
HSS	Hydrogen Storage System
TESS	Thermal Energy Storage Systems
PCM	Phase Change Materials
PV	Photovoltaics
PEM	Proton Exchange Membrane
SEH	Smart Energy Hub
DSM	Demand Side Management
CAES	Compressed Air Energy Storage
HES	Hydrogen Energy Storage
OCV	Open Circuit Voltage
EDL	Electrical Double Layer
GDL	Gas Diffusion Layer
EMS	Energy Management System
ELZ	Electrolyzer
FC	Fuel Cell
MEA	Membrane Electrode Assembly
$P_{L\text{-}his}$	Historical data of consumption of the load
NOR	Normal cost of electricity in absence of hydrogen system
HUB	Hydrogen Utilization Benefit
THUB	Total Hydrogen Utilization Benefit
HSB	Hydrogen Saving Benefit
C_{tot1}	Total cost of hydrogen production by the electrolyzer
C_{tot2}	Total contribution of the fuel cell
$C_{avg,6h}$	Average of the 6-highest unit price
$C_{avg,6h\text{-}7day}$	Average of 6-highest unit price of the past 7days
$C_{avg,5h}$	Average of the 5-cheapest unit price
$C_{avg,5h\text{-}7day}$	Average of 5-lowest unit price of the past 7days
ΔC_{save}	Overall cost savings

Nomenclature

T	Time	s
m	Mass	kg
$\dot{m}$	Mass flow rate	kg/s
V	Volume	m^3
l	Length	m
T	Temperature	K or °C
P	Pressure	Pa
ρ	Density	kg/ m^3
A	Surface area	m^2
R	Resistance	ohm
I	Current	A
i_0	Exchange current density	A/m^2
V_{OC}	Open circuit voltage	V
E_0	Standard electrode potential	V
E_{Nernst}	Nernst potential	V
α	Charge transfer coefficient	[-]
P	Power	W
E	Energy	J or Wh
HHV	Higher heating value	J/kg
LHV	Lower heating value	J/kg
R	Universal gas constant	J/mol.K
n	Number of moles	mole
F	Faraday's constant	C/mol
$\Delta\hat{G}^0$	Gibbs free energy	J
$\dot{H}$	Enthalpy flow rate	kJ/s
$\dot{Q}_{loss}$	Heat loss rate	kJ/s
U	Heat transfer coefficient	W/m^2K
C_{tot}	Overall thermal capacity of the system	kJ/K
$\dot{N}_{species}$	Molar flow rate	mol/s
$\dot{n}_{fuel}$	Fuel mass flow rate	kg/s
X	Hydrogen volume in tank	[%]
η	Efficiency of the system	[-]
C	Total cost	Norwegian krone (NOK)
ε	Error	%
α, β	Coefficient	[-]
NOR	Normal cost	NOK
HUB	Hydrogen utilization benefit	NOK
THUB	Total hydrogen utilization benefit	NOK
HSB	Hydrogen saving benefit	NOK

References

[1] K. Härkönen, *SMART BUILDINGS IN THE GREEN ENERGY TRANSITION*.

[2] "https://www.iea.org/policies/14454-climate-action-plan-20212030."

[3] C. Breyer *et al.*, "On the History and Future of 100% Renewable Energy Systems Research," *IEEE Access*, vol. 10, pp. 78176–78218, 2022, doi: 10.1109/ACCESS.2022.3193402.

[4] "O. Economics A. Viak Kartlegging og vurdering av potensial for effektivisering av oppvarming og kjøling i Norge in English: Mapping and assessment of potential for streamlining heating and cooling in Norway 2020 Oslo."

[5] H. Sadeghi, A. Ijaz, and R. M. Singh, "Current status of heat pumps in Norway and analysis of their performance and payback time," *Sustainable Energy Technologies and Assessments*, vol. 54. Elsevier Ltd, Dec. 01, 2022. doi: 10.1016/j.seta.2022.102829.

[6] M. Child, *TRANSITION TOWARDS LONG-TERM SUSTAINABILITY OF THE FINNISH ENERGY SYSTEM*.

[7] E. Janhunen, N. Leskinen, and S. Junnila, "The economic viability of a progressive smart building system with power storage," *Sustainability (Switzerland)*, vol. 12, no. 15, Aug. 2020, doi: 10.3390/su12155998.

[8] "https://sftool.gov/learn/about/649/building-energy-storage#:~:text=The%20capability%20to%20store%20energy,return%20it%20to%20the%20grid."

[9] Y. Elaouzy and A. El Fadar, "Potential of thermal, electricity and hydrogen storage systems for achieving sustainable buildings," *Energy Convers Manag*, vol. 294, Oct. 2023, doi: 10.1016/j.enconman.2023.117601.

[10] M. Kilic and A. F. Altun, "Dynamic modelling and multi-objective optimization of off-grid hybrid energy systems by using battery or hydrogen storage for different climates," *Int J Hydrogen Energy*, vol. 48, no. 60, pp. 22834–22854, Jul. 2023, doi: 10.1016/j.ijhydene.2022.12.103.

[11] L. Aiche-Hamane, M. Belhamel, B. Benyoucef, and M. Hamane, "Feasibility study of hydrogen production from wind power in the region of Ghardaia," *Int J Hydrogen Energy*, vol. 34, no. 11, pp. 4947–4952, Jun. 2009, doi: 10.1016/j.ijhydene.2008.12.037.

[12] P. Fragiacomo and M. Genovese, "Technical-economic analysis of a hydrogen production facility for power-to-gas and hydrogen mobility under different renewable sources in Southern Italy," *Energy Convers Manag*, vol. 223, Nov. 2020, doi: 10.1016/j.enconman.2020.113332.

[13] T. Nguyen, Z. Abdin, T. Holm, and W. Mérida, "Grid-connected hydrogen production via large-scale water electrolysis," *Energy Convers Manag*, vol. 200, Nov. 2019, doi: 10.1016/j.enconman.2019.112108.

[14] I. B. Mansir, E. H. Bani Hani, N. Farouk, A. AlArjani, H. Ayed, and D. D. Nguyen, "Comparative transient simulation of a renewable energy system with hydrogen and battery energy storage for residential applications," *Int J Hydrogen Energy*, vol. 47, no. 62, pp. 26198–26208, Jul. 2022, doi: 10.1016/j.ijhydene.2022.02.092.

[15] X. Li and M. Siavashi, "Compressed air and hydrogen energy storage hybridized with solar energy to supply electricity and hot water for a residential settlement," *Energy for Sustainable Development*, vol. 76, Oct. 2023, doi: 10.1016/j.esd.2023.101263.

[16] S. S. Mosayebi Javid, G. Derakhshan, and S. mehdi Hakimi, “Energy scheduling in a smart energy hub system with hydrogen storage systems and electrical demand management,” *Journal of Building Engineering*, vol. 80, Dec. 2023, doi: 10.1016/j.jobe.2023.108129.
[17] “https://www.statista.com/statistics/1025497/distribution-of-electricity-production-in-norway-by-source/.”
[18] D. , & M. P. Bessarabov, “Brief Historical Background of Water Electrolysis. In PEM Water Electrolysis,” *Elsevier*, pp. 17–42, 2018.
[19] Z. Abdin, C. J. Webb, and E. M. Gray, “Modelling and simulation of a proton exchange membrane (PEM) electrolyser cell,” *Int J Hydrogen Energy*, vol. 40, no. 39, pp. 13243–13257, Oct. 2015, doi: 10.1016/j.ijhydene.2015.07.129.
[20] H. Görgün, “Dynamic modelling of a proton exchange membrane (PEM) electrolyzer,” pp. 29–38, 2006.
[21] C. Y. Biaku, N. V. Dale, M. D. Mann, H. Salehfar, A. J. Peters, and T. Han, “A semiempirical study of the temperature dependence of the anode charge transfer coefficient of a 6 kW PEM electrolyzer,” *Int J Hydrogen Energy*, vol. 33, no. 16, pp. 4247–4254, Aug. 2008, doi: 10.1016/j.ijhydene.2008.06.006.
[22] R. Sorace, “Development and Analysis of Proton Exchange Membrane Water Electrolyzer (PEMWE) Model with Chemical Degradation Phenomenon,” 2021.
[23] R. García-Valverde, N. Espinosa, and A. Urbina, “Simple PEM water electrolyser model and experimental validation,” in *International Journal of Hydrogen Energy*, Jan. 2012, pp. 1927–1938. doi: 10.1016/j.ijhydene.2011.09.027.
[24] P. Colbertaldo, S. L. Gómez Aláez, and S. Campanari, “Zero-dimensional dynamic modeling of PEM electrolyzers,” in *Energy Procedia*, Elsevier Ltd, 2017, pp. 1468–1473. doi: 10.1016/j.egypro.2017.12.594.
[25] F. Marangio, M. Santarelli, and M. Calì, “Theoretical model and experimental analysis of a high pressure PEM water electrolyser for hydrogen production,” *Int J Hydrogen Energy*, vol. 34, no. 3, pp. 1143–1158, Feb. 2009, doi: 10.1016/j.ijhydene.2008.11.083.
[26] H. Zhang, G. Lin, and J. Chen, “Evaluation and calculation on the efficiency of a water electrolysis system for hydrogen production,” *Int J Hydrogen Energy*, vol. 35, no. 20, pp. 10851–10858, Oct. 2010, doi: 10.1016/j.ijhydene.2010.07.088.
[27] R. O’Hayre, S. Cha, W. G. Colella, and F. Prinz, *Fuel Cell Fundamentals. 3rd ed*. 2016.
[28] F. B. Hultin, “High-Capacity PEM Fuel Cells and Electrolysers in Hybrid Energy System for Offshore Power Generation,” 2020.
[29] R. Abid, *Dynamic Performance of a PEM Fuel Cell System*. APA, 2013. [Online]. Available: www.mek.dtu.dk
[30] “https://www.dibk.no/Regulations on technical requirements for construction works.”
[31] “https://www.uis.no/nb/om-uis/bor-gratis-pa-campus-mot-a-leve-baerekraftig.”
[32] M. 12, “Prosjektbeskrivelse for Ulla-Førrefondet.”
[33] “T. M. MATLAB 2020b, ‘Basic Principles of Modeling Physical Networks - MATLAB & Simulink.’ https://www.mathworks.com/help/physmod/simscape/ug/b asic-principles-of-modeling-physical-networks.html (accessed Dec. 16, 2021).”
[34] “‘Declare Through and Across Variables for a Domain - MATLAB & Simulink.’ https://www.mathworks.com/help/physmod/simscape/lang /declare-through-and-across-variables-for-a-domain.html (accessed Dec. 16, 2021).”
[35] R. Banihabib, T. Lingstädt, M. Wersland, P. Kutne, and M. Assadi, “Development and testing of a 100 kW fuel-flexible micro gas turbine running on 100% hydrogen,” *Int J Hydrogen Energy*, vol. 49, pp. 92–111, Jan. 2024, doi: 10.1016/j.ijhydene.2023.06.317.

[36] “https://se.mathworks.com/help/simscape/ug/connecting-simscape-diagrams-to-simulink-sources-and-scopes.html.”
[37] “https://se.mathworks.com/help/simscape/ref/flowratesourcetl.html?s_tid=doc_ta.”
[38] “https://se.mathworks.com/help/simscape/ref/pipetl.html?s_tid=doc_ta.”
[39] “https://se.mathworks.com/help/simscape/ug/pem-electrolysis-system.html.”
[40] “https://se.mathworks.com/help/simscape/ref/moisturesourcema.html?s_tid=doc_ta.”
[41] “https://se.mathworks.com/help/simscape/ref/constantvolumechamberma.html?s_tid=doc_ta.”
[42] “https://se.mathworks.com/help/simscape/ref/thermalmass.html.”
[43] T. E. Springer, T. A. Zawodzinski, and S. Gottesfeld, “Technical In-formation Bulletins 465-223,465-225, 465-246. 6. P. Wagner,” 1991. [Online]. Available: http://www.ecsdl.org/terms_use.jsp
[44] W. W. Yuan, K. Ou, S. Jung, and Y. B. Kim, “Analyzing and modeling of water transport phenomena in open-cathode polymer electrolyte membrane fuel cell,” *Applied Sciences (Switzerland)*, vol. 11, no. 13, Jul. 2021, doi: 10.3390/app11135964.
[45] “https://se.mathworks.com/help/simscape/ug/pem-fuel-cell-system.html.”
[46] “https://se.mathworks.com/help/simscape/ref/convectiveheattransfer.html?s_tid=doc_ta.”
[47] V. Liso, G. Savoia, S. S. Araya, G. Cinti, and S. K. Kær, “Modelling and experimental analysis of a polymer electrolyte membrane water electrolysis cell at different operating temperatures,” *Energies (Basel)*, vol. 11, no. 12, Dec. 2018, doi: 10.3390/en11123273.
[48] C. Spiegel, “PEM Fuel Cell Modeling and Simulation Using MATLAB ®.”
[49] “https://www.iso.org/standard/72085.html.”
[50] “https://www.nordpoolgroup.com/.”